

DUDLEY KNOX LIBRARY
NAVAL POSTGRADUATE SCHOOL
MONTEREY CA 93943-5101

Approved for public release; distribution is unlimited.

Hydrodynamic Flowfield Visualization Studies of a Mach 6 Waverider

by

Lowell Morgan Johnson
Lieutenant , United States Navy
B.S., University of Wisconsin -Madison, 1985

Submitted in partial fulfillment of the requirements for
the degree of

MASTER OF SCIENCE IN AERONAUTICAL ENGINEERING

from the

NAVAL POSTGRADUATE SCHOOL
March, 1994

REPORT DOCUMENTATION PAGE

Form Approved
OMB No. 0704-0188

1a. REPORT SECURITY CLASSIFICATION Unclassified			1b. RESTRICTIVE MARKINGS		
2a. SECURITY CLASSIFICATION AUTHORITY			3. DISTRIBUTION/AVAILABILITY OF REPORT Approved for public release; distribution is unlimited		
2b. DECLASSIFICATION/DOWNGRADING SCHEDULE					
4. PERFORMING ORGANIZATION REPORT NUMBER(S)			5. MONITORING ORGANIZATION REPORT NUMBER(S)		
6a. NAME OF PERFORMING ORGANIZATION Naval Postgraduate School		6b. OFFICE SYMBOL (If applicable)	7a. NAME OF MONITORING ORGANIZATION Naval Postgraduate School		
6c. ADDRESS (City, State, and ZIP Code) Monterey, CA 93943-5000		7b. ADDRESS (City, State, and ZIP Code) Monterey, CA 93943-5000			
8a. NAME OF FUNDING/SPONSORING ORGANIZATION		8b. OFFICE SYMBOL (If applicable)	9. PROCUREMENT INSTRUMENT IDENTIFICATION NUMBER		
8c. ADDRESS (City, State, and ZIP Code)			10. SOURCE OF FUNDING NUMBERS		
			PROGRAM ELEMENT NO.	PROJECT NO.	TASK NO.
			WORK UNIT ACCESSION NO.		
11. TITLE (Include Security Classification) HYDRODYNAMIC FLOWFIELD VISUALIZATION STUDIES OF A MACH 6 WAVERIDER					
12. PERSONAL AUTHOR(S) Lowell Morgan Johnson					
13a. TYPE OF REPORT Master's Thesis		13b. TIME COVERED FROM _____ TO _____		14. DATE OF REPORT (Year,Month,Day) March 1994	
15. PAGE COUNT 173					
16. SUPPLEMENTARY NOTATION The views expressed in this thesis are those of the author and do not reflect the official policy or position of the Department of Defense or the U.S. Government.					
17. COSATI CODES			18. SUBJECT TERMS (Continue on reverse if necessary and identify by block number)		
FIELD	GROUP	SUB-GROUP			
			Waverider, Flow visualization by dye injection, Water tunnel studies, Vortex development and bursting, Effect of static angle of attack and sideslip		
19. ABSTRACT (Continue on reverse if necessary and identify by block number) Flowfield visualization studies of a conical flow derived waverider were conducted in the Naval Postgraduate School water tunnel facility, as part of an ongoing study by the Naval Postgraduate School and the NASA Ames Research Center. The model, with an 8 inch root chord, 7.5 inch span and an aspect ratio of 1.41, was designed and constructed with an integrated forebody engine inlet ramp system and cowling for a hydrocarbon scramjet type propulsion system. Still photographs and video frames were taken for pitch angles between 0° and 20° and yaw angles between 0° and 10°. The waverider flowfield was similar to that associated with sharp leading edge delta wings with the primary vortex separating at the leading edge and rolling up over the upper surface. However, a comparison of waverider with delta wing data suggests that vortex core breakdown occurred at much lower angles of attack on the blunt nosed (planform) waverider.					
20. DISTRIBUTION/AVAILABILITY OF ABSTRACT <input checked="" type="checkbox"/> UNCLASSIFIED/UNLIMITED <input type="checkbox"/> SAME AS RPT. <input type="checkbox"/> DTIC USERS			21. ABSTRACT SECURITY CLASSIFICATION Unclassified		
22a. NAME OF RESPONSIBLE INDIVIDUAL C.F. Newberry			22b. TELEPHONE (Include Area Code) (408) 656 - 2892		22c. OFFICE SYMBOL AA/Ne

ABSTRACT

Flowfield visualization studies of a conical flow derived waverider were conducted in the Naval Postgraduate School water tunnel facility, as part of an ongoing effort by the Naval Postgraduate School and the NASA Ames Research Center. The model, with an 8 inch root chord, 7.5 inch span and an aspect ratio of 1.41, was designed and constructed with an integrated forebody engine inlet ramp system and cowling for a hydrocarbon scramjet type propulsion system. Still photographs and video frames were taken for pitch angles between 0° and 20° and yaw angles between 0° and 10° . The waverider vortical flowfield was similar to that associated with sharp leading edge delta wings with the primary vortex separating at the leading edge and rolling up over the upper surface. However, a comparison of waverider with delta wing data suggests that vortex core breakdown occurred at much lower angles of attack on the blunt nosed (planform) waverider.

T 70313
J 6236
C.1

TABLE OF CONTENTS

I.	INTRODUCTION	1
A.	BACKGROUND	1
B.	SUMMARY OF PREVIOUS WORK	6
C.	LOW-SPEED TESTING	9
D.	TEST PHILOSOPHY	9
E.	DELTA WING LOW-SPEED FLOW CHARACTERISTICS	9
II.	TESTING APPARATUS	13
A.	WATER TUNNEL.....	13
B.	THE MODEL	14
C.	METHOD OF PHOTOGRAPHY	15
III.	RESULTS/DISCUSSION.....	25
A.	BASELINE CONFIGURATION	26
1.	Angle of Attack Effects on Vortex Stability	26
2.	Sideslip Effects on Vortex Core Stability	29
3.	Angle of Attack effects on Vortex core Trajectory	31
4.	Sideslip Effects on Vortex Core Trajectory	32
B.	APEX DELTA.....	32
C.	MODIFICATION ONE.....	33
1.	Angle of Attack Effects.....	34
2.	Sideslip Effects	36
D.	MODIFICATION TWO	36
1.	Angle of Attack Effects.....	37
2.	Sideslip Effects	38
E.	MODIFICATION THREE.....	39
1.	Angle of Attack Effects.....	40
2.	Sideslip Effects	40
IV.	CONCLUSIONS AND RECOMMENDATIONS.....	125
A.	BASELINE MODEL	125

1. Angle of Attack Effects.....	125
2. Sideslip Effects	125
B. APEX DELTA MODIFICATIONS.....	126
1. Area Ratio Effects.....	126
3. Leading Edge Sweep Effects	126
C. RECOMMENDATIONS	127
APPENDIX A-MODEL SETUP AND INSTRUMENTATION.....	129
A. DYE PORT ATTACHMENT AND LOCATION.....	129
B. MODEL ALIGNMENT.....	130
APPENDIX B-APEX DELTA DESIGN.....	132
APPENDIX C-DATA TABLES	145
A. BASELINE.....	145
B. MODIFICATION ONE.....	148
C. MODIFICATION TWO	151
D. MODIFICATION THREE.....	154
LIST OF REFERENCES	157
INITIAL DISTRIBUTION LIST	159

LIST OF TABLES

TABLE 1.1	PERFORMANCE CONSTRAINTS	7
TABLE 3.1	TEST MATRIX	26
TABLE 3.2	APEX DELTA MODIFICATIONS TESTED.....	33
TABLE B.1	APEX DELTA DIMENSIONS	133
TABLE C.1	BASELINE LATERAL CORE TRAJECTORY (LEEWARD).....	145
TABLE C.2	BASELINE LATERAL CORE TRAJECTORY (WINDWARD).....	146
TABLE C.3	BASELINE BURST LOCATION	147
TABLE C.4	MOD 1 LATERAL CORE TRAJECTORY (LEEWARD).....	148
TABLE C.5	MOD 1 LATERAL CORE TRAJECTORY (WINDWARD).....	159
TABLE C.6	MOD 1 BURST LOCATION.....	150
TABLE C.7	MOD 2 LATERAL CORE TRAJECTORY (LEEWARD).....	151
TABLE C.8	MOD 2 LATERAL CORE TRAJECTORY (WINDWARD)	152
TABLE C.9	MOD 2 BURST LOCATION	153
TABLE C.10	MOD 3 LATERAL CORE TRAJECTORY (LEEWARD).....	154
TABLE C.11	MOD 3 LATERAL CORE TRAJECTORY (WINDWARD)	155
TABLE C.12	MOD 3 BURST LOCATION	156

LIST OF FIGURES

Figure 1.1	Nonweiler's Caret Wing.....	3
Figure 1.2	Conical Flow Waverider.....	4
Figure 1.3	Bowcut-Anderson Mach 6 Waverider	5
Figure 1.4	Mach 6 Waverider Tested by Vanhoy	5
Figure 1.5	Mission Profile	7
Figure 1.6	Price Mach 6 Waverider.....	8
Figure 1.7	Flow Field Over Sharp Edged Delta Wing	10
Figure 1.8	Leading Edge Vortices Made Visible by Dye Streaks in Water Flow	11
Figure 1.9	Spanwise Pressure Distribution Over Sharp Edged Delta Wing.....	11
Figure 1.10	Vortex Burst Pattern	12
Figure 2.1	NPS Flow Visualization Facility	16
Figure 2.2	Dye Supply System.....	17
Figure 2.3	Model Support System.....	18
Figure 2.4	Model Support System in the Up Position	19
Figure 2.5	Control Panel	20
Figure 2.6	Top View of Waverider Model.....	21
Figure 2.7	Bottom View of Waverider Model.....	22
Figure 2.8	Side View of Waverider Model	23
Figure 2.9	Front View of Waverider Model	24
Figure 3.1	Angle of Attack Effects, Baseline Model, $\alpha=3^\circ$, $\beta=0^\circ$	42
Figure 3.2	Angle of Attack Effects, Baseline Model, $\alpha=6^\circ$, $\beta=0^\circ$	43
Figure 3.3	Angle of Attack Effects, Baseline Model, $\alpha=9^\circ$, $\beta=0^\circ$	44
Figure 3.4	Angle of Attack Effects, Baseline Model, $\alpha=12^\circ$, $\beta=0^\circ$	45
Figure 3.5	Angle of Attack Effects, Baseline Model, $\alpha=15^\circ$, $\beta=0^\circ$	46
Figure 3.6	Angle of Attack Effects, Baseline Model, $\alpha=17.5^\circ$, $\beta=0^\circ$	47
Figure 3.7	Angle of Attack Effects, Baseline Model, $\alpha=20^\circ$, $\beta=0^\circ$	48

Figure 3.8	Vortex Burst Location as a Function of Angle of Attack, Baseline Model Compared to Delta Wing, $\beta=0^\circ$	49
Figure 3.9	Baseline Model, Entrainment, $\alpha=4^\circ$, $\beta=0^\circ$	50
Figure 3.10	Baseline Model, Entrainment, $\alpha=8^\circ$, $\beta=0^\circ$	51
Figure 3.11	Baseline Model, Entrainment, $\alpha=10^\circ$, $\beta=0^\circ$	52
Figure 3.12	Sideslip Effects, Baseline Model, $\alpha=7^\circ$, $\beta=0^\circ$	53
Figure 3.13	Sideslip Effects, Baseline Model, $\alpha=7^\circ$, $\beta=5^\circ$	54
Figure 3.14	Sideslip Effects, Baseline Model, $\alpha=7^\circ$, $\beta=10^\circ$	55
Figure 3.15	Sideslip Effects, Baseline Model, $\alpha=2^\circ$, $\beta=10^\circ$	56
Figure 3.16	Sideslip Effects, Baseline Model, $\alpha=4^\circ$, $\beta=10^\circ$	57
Figure 3.17	Sideslip Effects, Baseline Model, $\alpha=5^\circ$, $\beta=10^\circ$	58
Figure 3.18	Sideslip Effects, Baseline Model, $\alpha=7^\circ$, $\beta=10^\circ$	59
Figure 3.19	Sideslip Effects, Baseline Model, $\alpha=9^\circ$, $\beta=10^\circ$	60
Figure 3.20a	Baseline Model, Vortex Burst Asymmetry.....	61
Figure 3.20b	Baseline Model Compared to 70° Delta Wing, Vortex Burst Asymmetry	62
Figure 3.21	Baseline Model, Angle of Attack Effects on Vortex Core Lateral Position, $\beta=0^\circ$	63
Figure 3.22	Baseline Model Compared to Delta Wing, Vortex Core Lateral Position, $\beta=0^\circ$	64
Figure 3.23	Baseline Model, Sideslip Effects on Vortex Core Lateral Position (leeward Side)	65
Figure 3.24	Baseline Model, Sideslip Effects on Vortex Core Lateral Position (Windward Side)	66
Figure 3.25	Entrainment, Modification One, $\alpha=4^\circ$, $\beta=0^\circ$	67
Figure 3.26	Entrainment, Modification One, $\alpha=6^\circ$, $\beta=0^\circ$	68
Figure 3.27	Entrainment, Modification One, $\alpha=10^\circ$, $\beta=0^\circ$	69
Figure 3.28	Entrainment, Modification One, $\alpha=8^\circ$, $\beta=10^\circ$	70
Figure 3.29	Entrainment, Modification One, $\alpha=12^\circ$, $\beta=10^\circ$	71
Figure 3.30	Angle of Attack Effects, Modification One, $\alpha=2^\circ$, $\beta=0^\circ$	72
Figure 3.31	Angle of Attack Effects, Modification One, $\alpha=6^\circ$, $\beta=0^\circ$	73
Figure 3.32	Angle of Attack Effects, Modification One, $\alpha=12^\circ$, $\beta=0^\circ$	74
Figure 3.33	Angle of Attack Effects, Modification One, $\alpha=16^\circ$, $\beta=0^\circ$	75

Figure 3.34	Angle of Attack Effects, Modification One, $\alpha=20^\circ$, $\beta=0^\circ$	76
Figure 3.35	Vortex Burst Location as a Function of Angle of Attack, Baseline Model Compared to Modification One and Delta Wing, $\beta=0^\circ$	77
Figure 3.36	Baseline Model Compared to Modification One and Delta Wing, Vortex Core Lateral Position, $\beta=0^\circ$	78
Figure 3.37	Sideslip Effects, Modification One, $\alpha=8^\circ$, $\beta=0^\circ$	79
Figure 3.38	Sideslip Effects, Modification One, $\alpha=8^\circ$, $\beta=5^\circ$	80
Figure 3.39	Sideslip Effects, Modification One, $\alpha=8^\circ$, $\beta=10^\circ$	81
Figure 3.40	Modification One, Vortex Burst Asymmetry	82
Figure 3.41	Modification One, Sideslip Effects on Vortex Core Lateral Position (leeward Side)	83
Figure 3.42	Modification One, Sideslip Effects on Vortex Core Lateral Position (Windward Side)	84
Figure 3.43	Modification Two, Angle of Attack Effects, $\alpha=4^\circ$, $\beta=0^\circ$	85
Figure 3.44	Modification Two, Angle of Attack Effects, $\alpha=12^\circ$, $\beta=0^\circ$	86
Figure 3.45	Modification Two, Angle of Attack Effects, $\alpha=16^\circ$, $\beta=0^\circ$	87
Figure 3.46	Modification Two, Angle of Attack Effects, $\alpha=24^\circ$, $\beta=0^\circ$	88
Figure 3.47	Modification Two, Sideslip Effects, $\alpha=12^\circ$, $\beta=5^\circ$	89
Figure 3.48	Modification Two, Sideslip Effects, $\alpha=12^\circ$, $\beta=10^\circ$	90
Figure 3.49	Angle of Attack Effects, Modification Two, $\alpha=4^\circ$, $\beta=0^\circ$	91
Figure 3.50	Angle of Attack Effects, Modification Two, $\alpha=12^\circ$, $\beta=0^\circ$	92
Figure 3.51	Angle of Attack Effects, Modification Two, $\alpha=16^\circ$, $\beta=0^\circ$	93
Figure 3.52	Angle of Attack Effects, Modification Two, $\alpha=20^\circ$, $\beta=0^\circ$	94
Figure 3.53	Vortex Burst Location as a Function of Angle of Attack Baseline Model Compared to Modification Two and Delta Wing, $\beta=0^\circ$	95
Figure 3.54	Baseline Model Compared to Modification Two and Delta Wing, Vortex Core Lateral Position, $\beta=0^\circ$	96
Figure 3.55	Sideslip Effects, Modification Two, $\alpha=8^\circ$, $\beta=0^\circ$	97
Figure 3.56	Sideslip Effects, Modification Two, $\alpha=8^\circ$, $\beta=5^\circ$	98
Figure 3.57	Sideslip Effects, Modification Two, $\alpha=8^\circ$, $\beta=10^\circ$	99
Figure 3.58	Modification Two, Vortex Burst Asymmetry	100

Figure 3.59	Modification Two, Sideslip Effects on Vortex Core Lateral Position (leeward Side).....	101
Figure 3.60	Modification Two, Sideslip Effects on Vortex Core Lateral Position (Windward Side)	102
Figure 3.61	Modification Three, Angle of Attack Effects, $\alpha=8^\circ$, $\beta=0^\circ$	103
Figure 3.62	Modification Three, Angle of Attack Effects, $\alpha=16^\circ$, $\beta=0^\circ$	104
Figure 3.63	Modification Three, Angle of Attack Effects, $\alpha=20^\circ$, $\beta=0^\circ$	105
Figure 3.64	Modification Three, Sideslip Effects, $\alpha=12^\circ$, $\beta=0^\circ$	106
Figure 3.65	Modification Three, Sideslip Effects, $\alpha=12^\circ$, $\beta=5^\circ$	107
Figure 3.66	Modification Three, Sideslip Effects, $\alpha=12^\circ$, $\beta=10^\circ$	108
Figure 3.67	Modification Three, Sideslip Effects, $\alpha=8^\circ$, $\beta=+5^\circ$	109
Figure 3.68	Modification Three, Sideslip Effects, $\alpha=8^\circ$, $\beta=0^\circ$	110
Figure 3.69	Modification Three, Sideslip Effects, $\alpha=8^\circ$, $\beta=-5^\circ$	111
Figure 3.70	Angle of Attack Effects, Modification Three, $\alpha=4^\circ$, $\beta=0^\circ$	112
Figure 3.71	Angle of Attack Effects, Modification Three, $\alpha=8^\circ$, $\beta=0^\circ$	113
Figure 3.72	Angle of Attack Effects, Modification Three, $\alpha=12^\circ$, $\beta=0^\circ$	114
Figure 3.73	Angle of Attack Effects, Modification Three, $\alpha=16^\circ$, $\beta=0^\circ$	115
Figure 3.74	Vortex Burst Location as a Function of Angle of Attack, Baseline Model, Modification Three and Delta Wing, $\beta=0^\circ$	116
Figure 3.75	Modification Three, Sideslip Effects on Vortex Core Lateral Position (Leeward Side).....	117
Figure 3.76	Modification Three, Sideslip Effects on Vortex Core Lateral Position (Windward Side).....	118
Figure 3.77	Baseline Model Compared to Modification Three and Delta Wing, Vortex Core Lateral Position, $\beta=0^\circ$	119
Figure 3.78	Sideslip Effects, Modification Three, $\alpha=8^\circ$, $\beta=5^\circ$	120
Figure 3.79	Sideslip Effects, Modification Three, $\alpha=8^\circ$, $\beta=10^\circ$	121
Figure 3.80	Sideslip Effects, Modification Three, $\alpha=16^\circ$, $\beta=5^\circ$	122
Figure 3.81	Sideslip Effects, Modification Three, $\alpha=16^\circ$, $\beta=10^\circ$	123
Figure 3.82	Modification Three, Vortex Burst Asymmetry	124
Figure 4.1	Comparison of 0° Sideslip Burst Behavior.....	128
Figure A.1	Baseline model Dye Port Location	129
Figure A.2	Roll Level Adjustment (Rear View).....	130

Figure A.3	Roll Level Adjustment (Top View)	131
Figure B.1	Apex Delta.....	133
Figure B.2	Modification 1 (Top View).....	134
Figure B.3	Modification 1 (Bottom View).....	135
Figure B.4	Modification 1 (Side View)	136
Figure B.5	Modification 1 (Isometric View).....	137
Figure B.6	Modification 1 (Side View Close-up)	138
Figure B.7	Modification 1 (Bottom View Close-up).....	139
Figure B.8	Modification 2 (Top View).....	140
Figure B.9	Modification 2 (Top View Close-up).....	141
Figure B.10	Modification 3 (Top View).....	142
Figure B.11	Modification 3 (Top View Close-up).....	143
Figure B.12	Modification 3 (Bottom View) With Dye Ports	144

I. INTRODUCTION

A. BACKGROUND

The waverider concept has been around since 1959 when Nonweiler introduced the concept of a three-dimensional body derived from the flow field behind a planar shock [Ref. 1]. Nonweiler's waverider had a delta planform and a caret shaped cross section as seen in Figure 1.1 [Ref. 2].

A waverider operating at its design Mach number rides on its own shock wave, hence the term waverider. The shock is attached all along its leading edge, not allowing the high pressure air behind the shock to leak around to the upper surface. The upper panels of the caret wing are streamwise planes and, hence, introduce no pressure drag. At its design Mach number the lower surface panels are subjected to constant pressure and the corresponding drag component, which is associated with the planar shock attached to the leading edges. As a result, waverider wave drag is much smaller than the wave drag of conventional supersonic or hypersonic configurations which, correspondingly, results in higher ratios of lift over drag (L/D) [Ref. 2].

Interestingly, discovery of the waverider concept had been made and tested before Nonweiler's paper of 1959 was published. In 1955, NASA Ames research engineer, Dr. Alfred Eggers conceived of a flat topped supersonic aircraft with a wing tapered to follow its own shockwave. Preliminary testing revealed values of L/D of 6.5 at Mach 5, much improved over then current technology values of 4. After extensive wind tunnel testing, NASA, in 1956, made the results available to all authorized aircraft firms. North American Aviation was the only firm to take advantage of NASA's discovery and, as a result was able to win a design

competition for an advanced long-range bomber. The bomber design that grew out of it was the B-70 Valkyrie. North American engineers labeled the technology the "pressure field" concept. The application of Dr. Eggers discovery to the design of the B-70 contributed toward its ability to cruise at supersonic speeds and achieve almost the same range as was previously attainable only by a subsonic cruise airplane [Ref. 3].

Beginning in the late 1960's, the waverider concept was expanded to include vehicles designed from the axisymmetric flow over a right circular cone. Figure 1.2 [Ref. 2] shows a conical flow waverider. Rassmussen extended work in this area by employing analytic expressions gained from hypersonic small disturbance theory to generate optimum waveriders from flows over inclined circular cones and elliptic cylinders [Ref. 4].

The next step in waverider development was taken by Bowcutt and Anderson, who generated a series of viscous optimized (L/D) conical flow waveriders. Figure 1.3 [Ref. 5] shows the Bowcutt-Anderson optimum result for a Mach 6 waverider design. In 1988 Vanhoy expanded the work of Bowcutt into the low-speed regime with wind tunnel tests of a Mach 6 viscous optimized waverider and a sharp-edged delta wing with the same length, span and base thickness as the waverider. Vanhoy compared the subsonic performance of his waverider and delta wing and found the low-speed characteristics of the waverider very similar to those of the sharp-edged delta wing in that the primary vortex, which results from separation at the leading edge, dominates the flow. Vanhoy concluded that both his waverider and delta wing had the same drag characteristics and the same L/D . Vanhoy also compared his waverider and delta wing data to Polhamus' vortex lift theory and found the results for both wing

types were nearly identical to the theory. Figure 1.4 [Ref. 6] shows the waverider Vanhoy used in his tests.

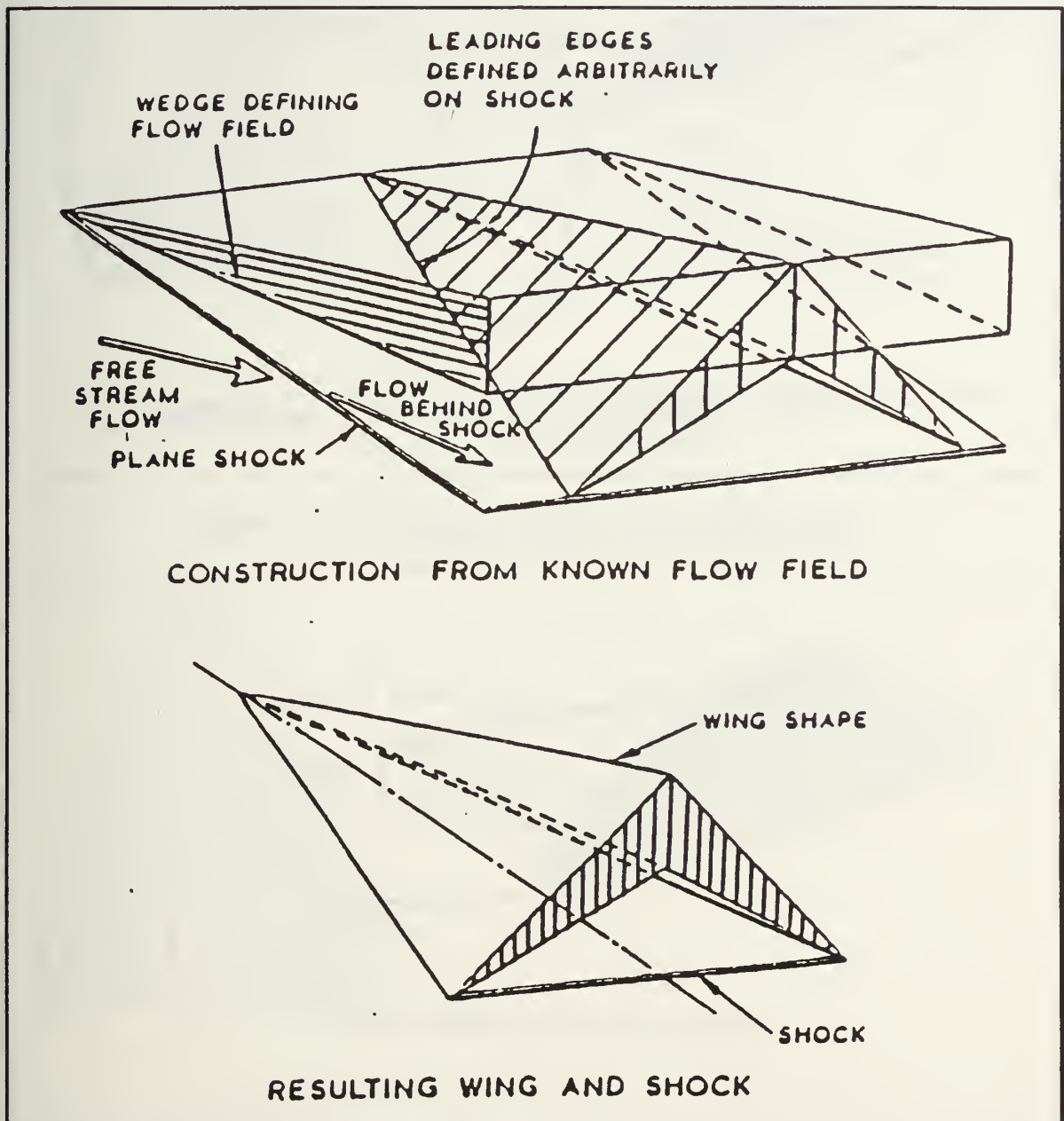


Figure 1.1 Nonweiler's Caret Wing

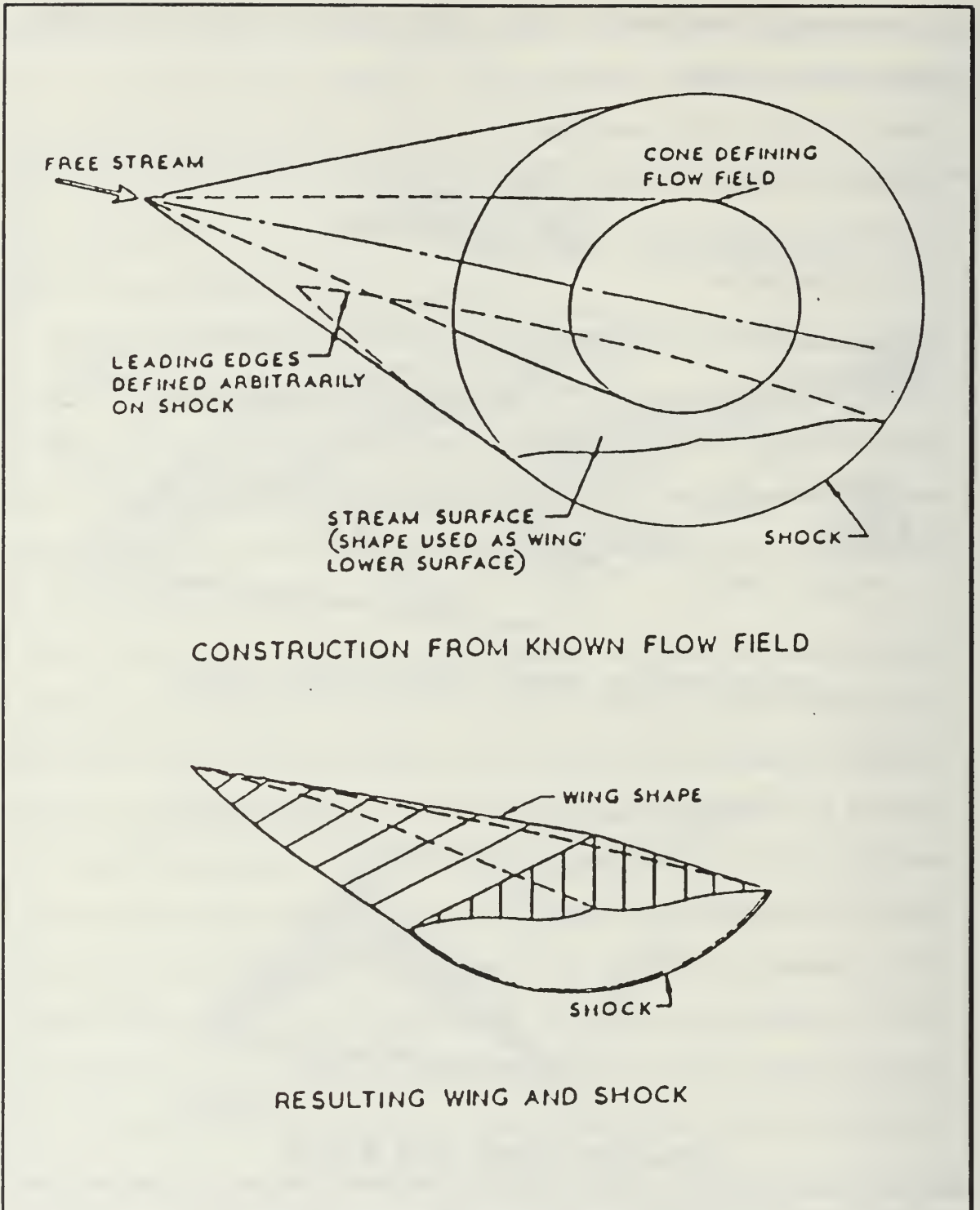


Figure 1.2 Conical Flow Waverider

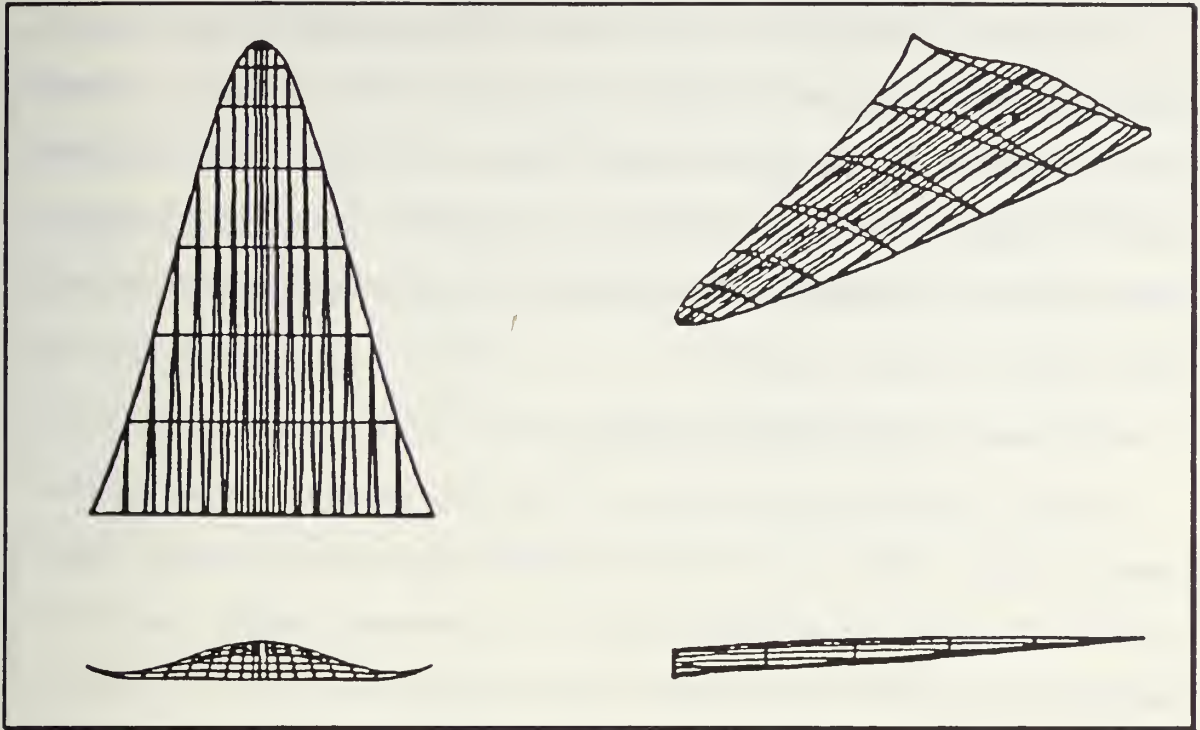


Figure 1.3 Bowcutt-Anderson Mach 6 Waverider

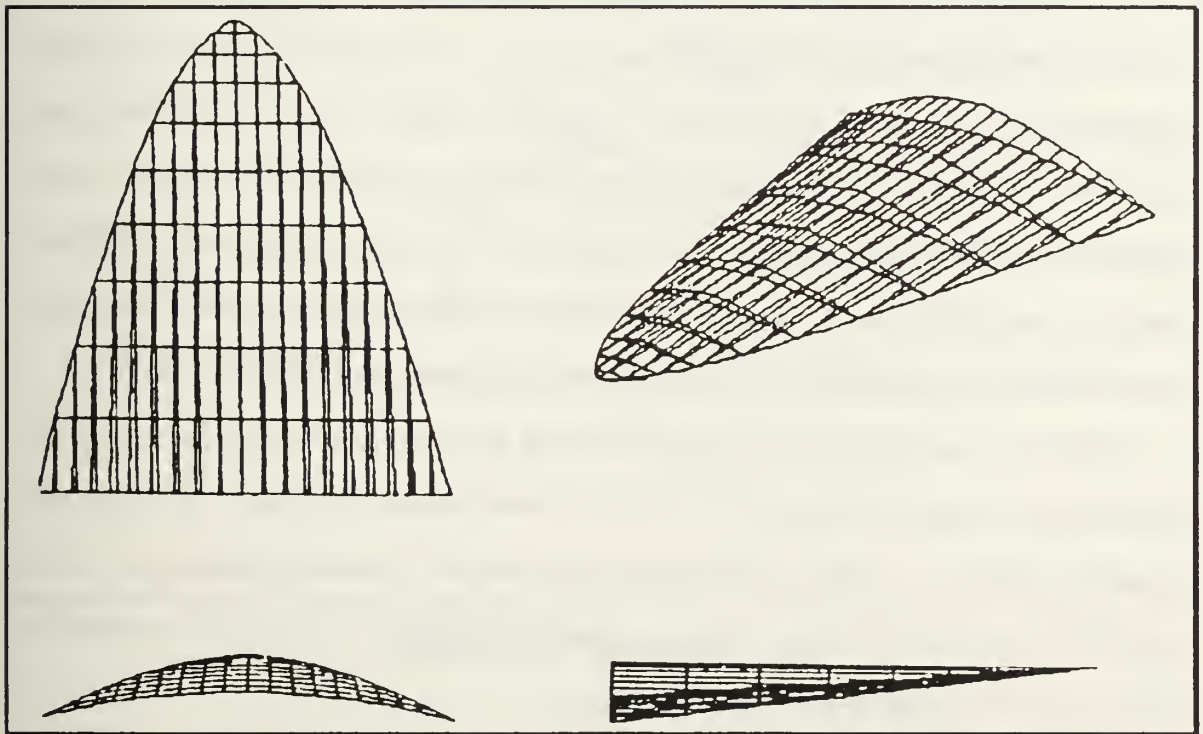


Figure 1.4 Mach 6 Waverider Tested by Vanhoy

In 1993 Price, in conjunction with the NASA Ames Research Center, Systems Analysis Branch, designed a conical based hydrocarbon-scramjet-powered viscous optimized $[(L/D)(I_{sp})]$ waverider subject to mission and performance constraints (I_{sp} refers to specific impulse). As a follow on to Price's work, the present study is an experimental investigation of the low-speed characteristics of Price's Mach 6 optimized waverider.

B. SUMMARY OF PREVIOUS WORK

The Price waverider tested herein was designed to perform a carrier launched intercept mission. Table 1.1 contains the specific mission parameters and Figure 1.5 [Ref. 7] depicts the intercept mission. As previously stated a numerical optimization to maximize the product of L/D and I_{sp} was completed. Using this product for the optimization criteria resulted in tradeoffs during the optimization process between aerodynamic and engine performance. The unique feature of the Price waverider is that the engine and body were designed together, from the beginning, to work as a single unit. Figure 1.6 [Ref. 7] depicts the resulting optimum configuration and dimensions with the integrated forebody ramp system. While Price's optimum design called for a leading edge radius of zero, practical considerations dictated a more realistic value of 0.4995 inches. Planform area remained unchanged however, from Price's optimized value of 2266.33 ft².

The Price waverider was generated using the waverider code developed by the Systems Analysis Branch of the NASA Ames Research Center. The code and its subroutines are a subset of the Hypersonic Aircraft Vehicle Optimization Code (HAVOC), also created by the Systems Analysis Branch. For more information on this code and its application see Reference 8.

TABLE 1.1 PERFORMANCE CONSTRAINTS

Range	1000 nautical mile combat radius
Cruise	Mach 6 at Best Cruise Altitude
Combat	Twenty minutes on-station, air intercept, no dog fighting
Loiter	Twenty minutes at sea level at Best Loiter Speed
Approach Speed	< 140 KTS
Takeoff and Landing	Catapult launch and arrested recovery

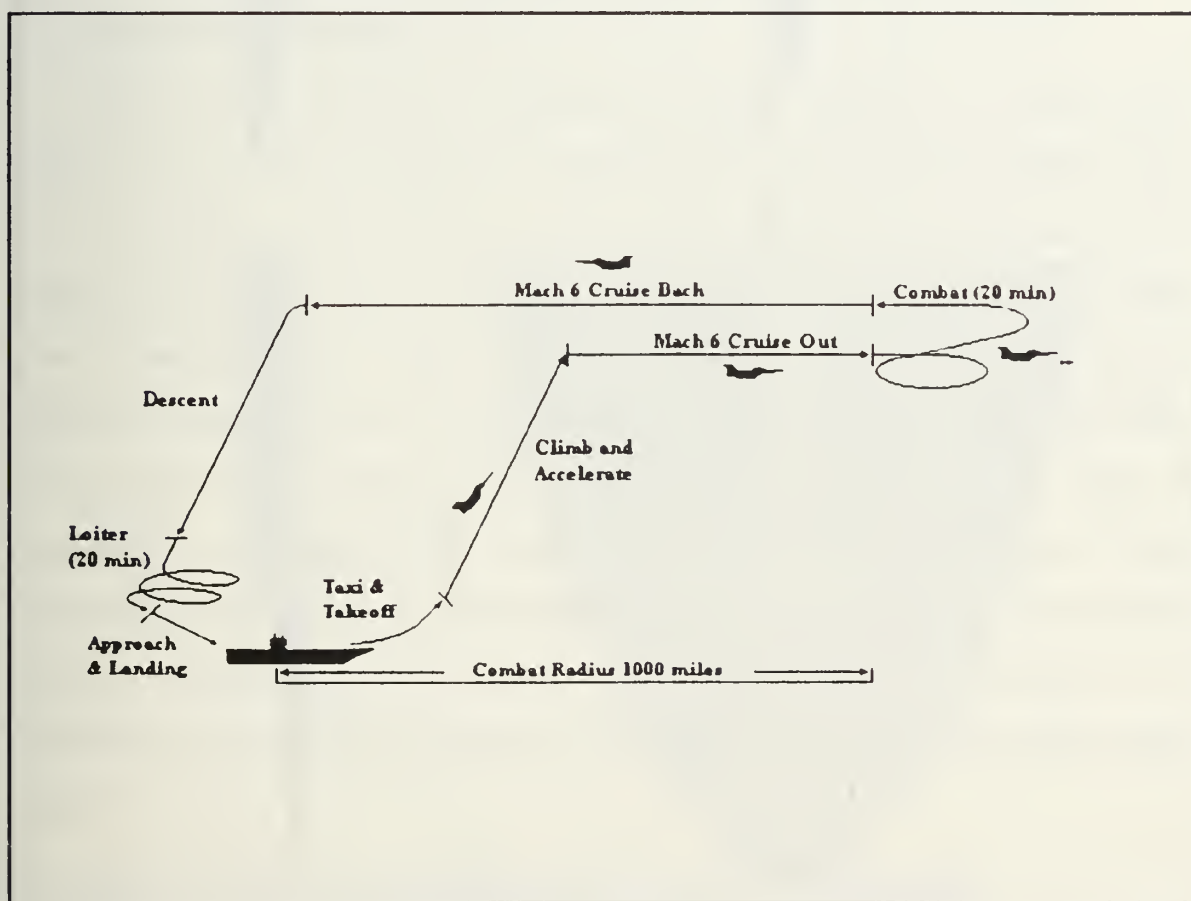


Figure 1.5 Mission Profile

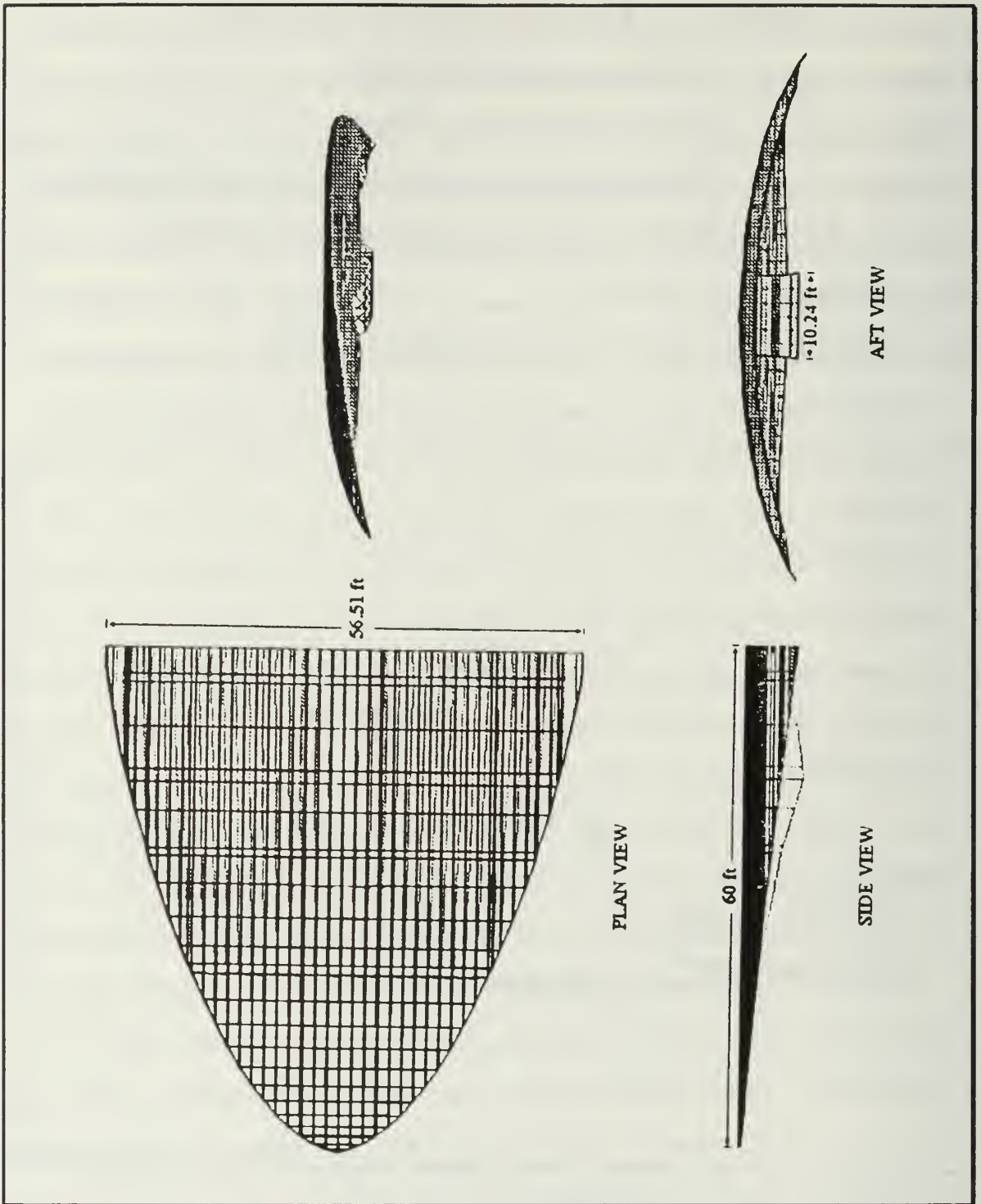


Figure 1.6 Price Mach 6 Waverider

C. LOW-SPEED TESTING

Even a Mach 6 optimized waverider must take-off and land; for this reason its low-speed flying qualities are of interest. Prior knowledge of vortex core trajectories and vortex burst positions will facilitate the development and implementation of theoretical methods to predict surface loading characteristics and will help to explain the results of planned follow-on wind tunnel testing. Recognizing that little theoretical work has been done on waveriders in the low-speed flight regime, low-speed testing was considered useful.

D. TEST PHILOSOPHY

With no water tunnel flow visualization studies available on waverider type aircraft, but a wealth of this type of data available for low aspect ratio delta wings, it was considered informative to do as Vanhoy had done in his study and compare the waverider flow visualization results to low aspect ratio delta wing flow visualization data. Thus, the NPS/NASA ARC test philosophy developed along the following lines: 1) conduct flow visualization studies of the waverider model flowfield, recording vortex core trajectory and burst location data; 2) compare the waverider data to similar aspect ratio delta wing data; and 3) test various high lift devices on the waverider model and compare to previous test results. Before comparing waverider test results to delta wing data it is informative to review the primary flow characteristics of thin sharp-edged delta wings.

E. DELTA WING LOW-SPEED FLOW CHARACTERISTICS

The subsonic flow pattern over the top of a flat plate delta wing at angle-of-attack is shown in Figure 1.7 [Ref. 9]. Generally, two symmetric leading edge vortices form at the apex as the wing pitches up. A hydrodynamic flow

visualization of such leading edge vortices is shown in Figure 1.8 [Ref. 10]. These vortices cause the flow over the upper surface to accelerate producing extra lift called vortex lift. Figure 1.9 [Ref. 10] shows a sketch of the spanwise variation of pressure over the top surface of a delta wing. At high angles of attack the core flow of the vortex suddenly stagnates and expands in size, called bursting as shown in Figure 1.9 [Ref. 11]. Once the vortex has burst there is a loss of suction and, hence, a loss of the extra lift associated with that vortex from the point of bursting downstream over the top of the wing.

Burst location is known to be affected by wing sweep, angle-of-attack, and the shape of the leading edge. Vortex breakdown begins aft of the trailing edge and progresses forward as the angle-of-attack increases. The lift coefficient reaches a maximum value approximately as the vortex bursting reaches the trailing edge. As the vortex breakdown progresses over the upper surface, the wing displays first a pitch-up tendency due to the loss of lift near the trailing edge and then a pitch-down tendency due to the loss of lift at the front of the wing.

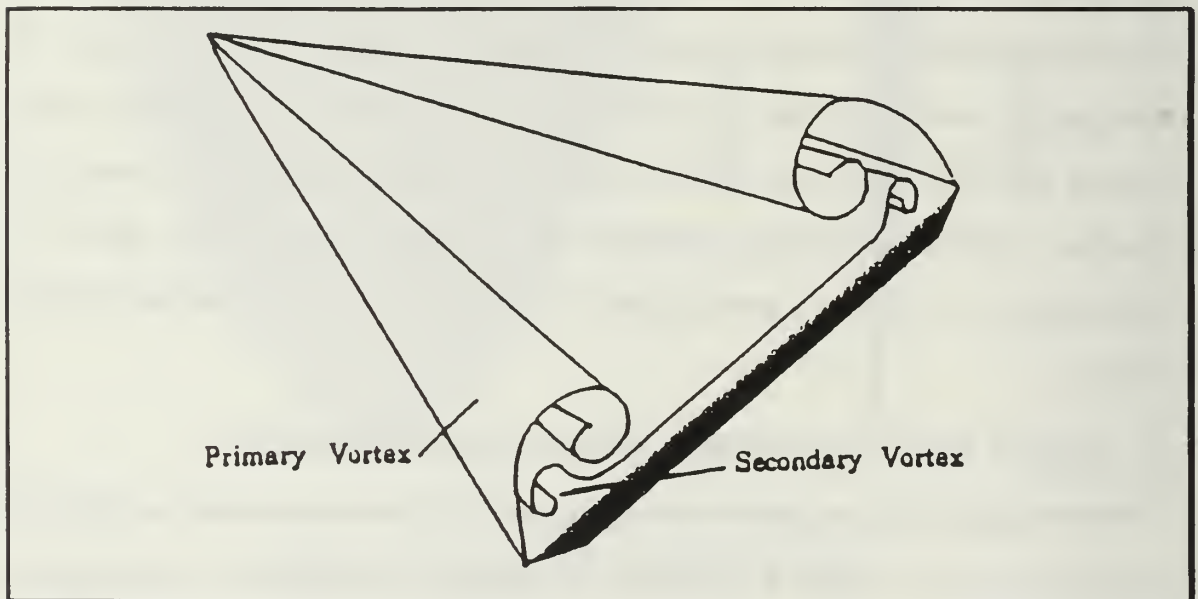


Figure 1.7 Flow Field Over Sharp Edged Delta Wing



Figure 1.8 Leading Edge Vortices Made Visible by Dye Streaks in Water Flow

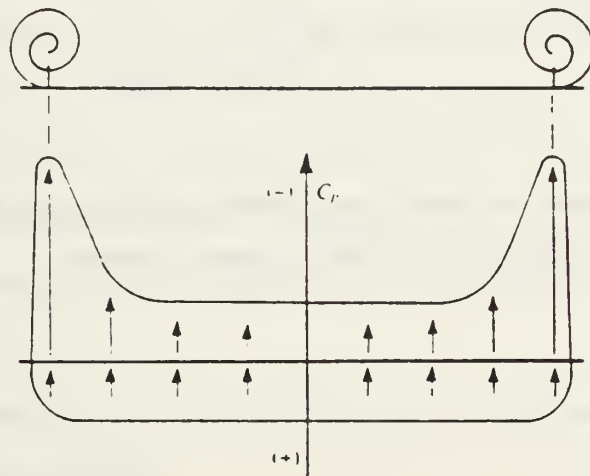


Figure 1.9 Spanwise Pressure Distribution Over Sharp Edged Delta Wing

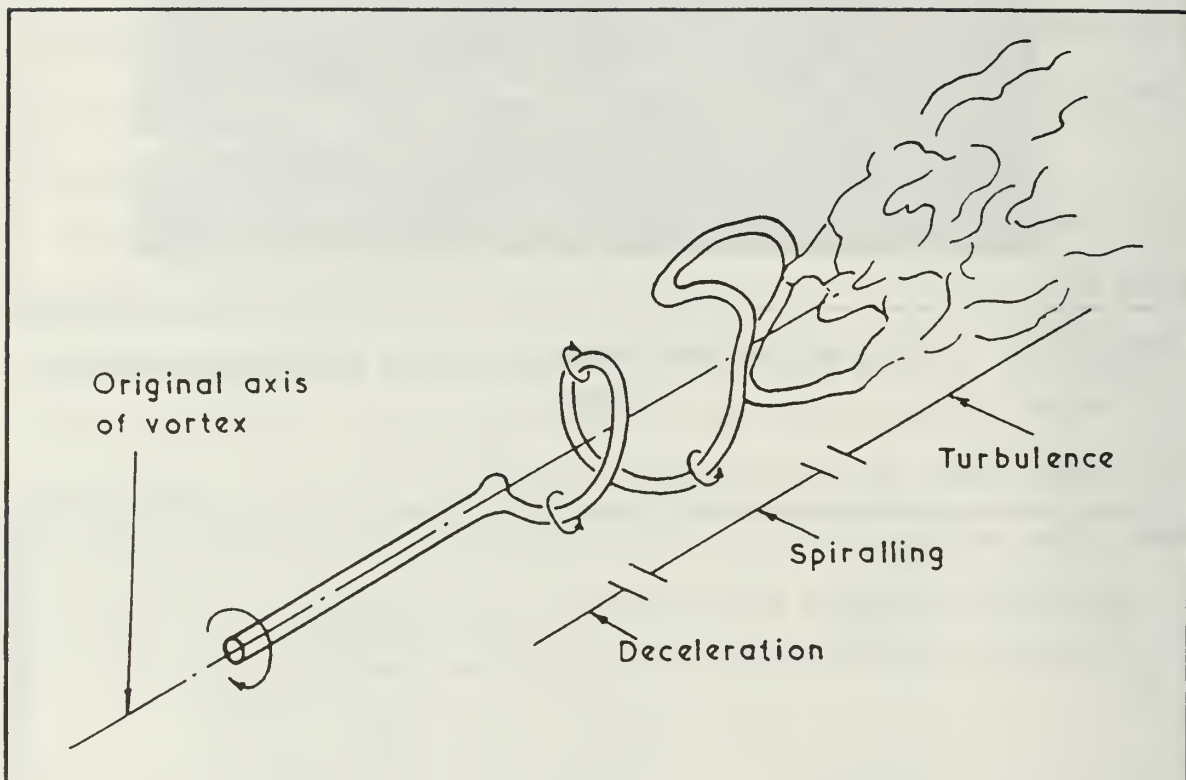


Figure 1.10 Vortex Burst Pattern

II. TESTING APPARATUS

A. WATER TUNNEL

The tests for this study were conducted in the Naval Postgraduate School (NPS) Flow Visualization Water Tunnel facility which was designed by Eidetics International, Inc., Torrance, California and installed at NPS in late 1988. Figure 2.1 [Ref. 12] shows a sketch of the NPS facility. The NPS water tunnel is a closed-circuit facility for studying a wide range of fluid phenomena. Two of its key design features are horizontal orientation and continuous operation. The horizontal orientation facilitates access and enables models to be readily changed without draining the water from the tunnel. The rate of circulation of water is up to 900 gallons/minute which corresponds to a flow rate of up to 1 ft/sec in the test section.

The test section is 15 inches wide, 20 inches high, and 60 inches long. The side walls of the test section have a slight divergence to compensate for boundary layer growth and to maintain uniform flow velocity throughout. The test section walls were constructed of tempered glass to provide thermal stability and simultaneous viewing of the model from the top, bottom, both sides and from the rear.

The level of flow quality (measured outside the boundary layer) over the test section velocities is as follows:

Mean flow angularity:	$< \pm 1.0^\circ$
Turbulence intensity level:	$< \pm 1.0 \% \text{ RMS}$
Velocity uniformity:	$< \pm 2.0$

Six pressurized dye canisters using water soluble food coloring were used to supply dye for flow visualization. Each canister was pressurized with air to 15 psig by a small compressor and connected to the model port through an individually routed line. Details of dye port location and method of attachment can be found in Appendix A. The quantity of dye was manually regulated by individual valves on each canister. The advantage of a pressurized system is finer control of dye emission and the ability to blow out the dye lines going to the model to prevent clogs. Figure 2.2 shows a photo of the dye supply system.

To minimize flow interference effects the model is mounted upside down in the test section as shown in Figure 2.3. The model support system utilizes a C-strut to vary the model pitch from -10° to $+70^{\circ}$ and a turntable to provide yaw variations of $\pm 20^{\circ}$. Easy and rapid access to the model is provided by mounting the support system on top of the test section. As seen in Figure 2.4, the entire assembly can be tilted out of the water circuit for model changes. The model attitude control system consists of two servo motors which provide independent control of model pitch and yaw. Figure 2.5 shows the model attitude and flow velocity control panel.

B. THE MODEL

Model scale was determined by Price by utilizing a general rule of thumb that is to limit flow blockage to five percent of the test section area. Price estimated 20° as the maximum angle of attack of interest from which he determined a model plan area of 40.60 in², root chord length of eight inches, span of 7.53 inches, and leading edge radius of .006 inches ($\pm .002$ inches) [Ref. 7].

The model was then constructed of non-heat treated 7075 aluminum alloy by the NASA Ames machine shop on a Cincinnati M3, computerized three axis

milling machine. Aluminum was chosen for its relatively low cost, its rigidity and its ability to hold the extremely sharp leading edge, which was required by the design, through-out the fabrication process. Heat generated by the milling bit during construction caused some leading edge warping to occur. To restore the leading edge an eighth of an inch of material had to be hand trimmed from that area resulting in a model chord length of 7.875 inches. However the leading edge radius was maintained at .006 inches. Figures 2.6-2.8 show the completed model.

C. METHOD OF PHOTOGRAPHY

The photographic equipment for the experimental test sessions consisted of two 35 mm automatic cameras, 3 Smith-Victor 600 watt photographic lights, and a fixed flood light installed below the test section. Lighting was adjusted to reduce shadowing and reflections as much as possible.

A Minolta 5000i camera with depth card and automatic focus, shutter speed control, aperture control and ASA setting was used for the side view photos. The depth card maximizes camera depth of field and is inserted into the camera body when the camera is operated in the program mode. A Nikon 2050 camera with features similar to the Minolta (without automatic ASA and focus) was used for the top view photographs. The film used for the side view photographs was 35 mm black and white ASA 400. Side view exposure settings were set to automatic. Focus was set to manual to better isolate the dye streaks from the model. The film for the top view photos was 35 mm black white ASA 3200. At the advice of the NPS photo lab technicians, top view camera settings were ASA 1600 with an aperture of 11 and shutter speed set to automatic. This set-up gave the highest contrast between the different colored dyes on the black and white

film which was essential when looking at multiple dye locations (and colors) simultaneously. Video frames were taken with a Panasonic VHS video camera utilizing AMPEX 189 T120 Broadcast Videocassettes.

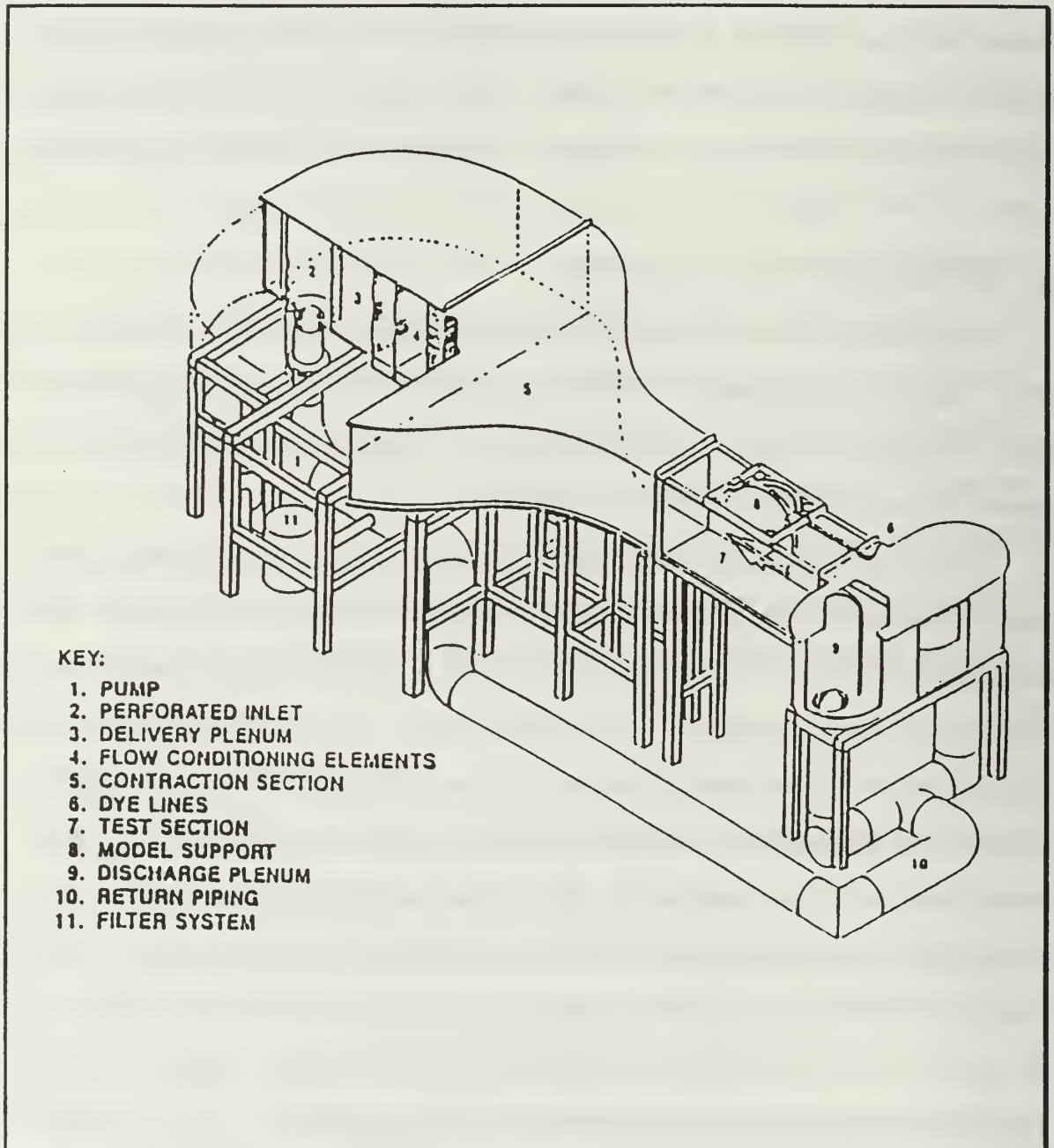


Figure 2.1 NPS Flow Visualization Facility

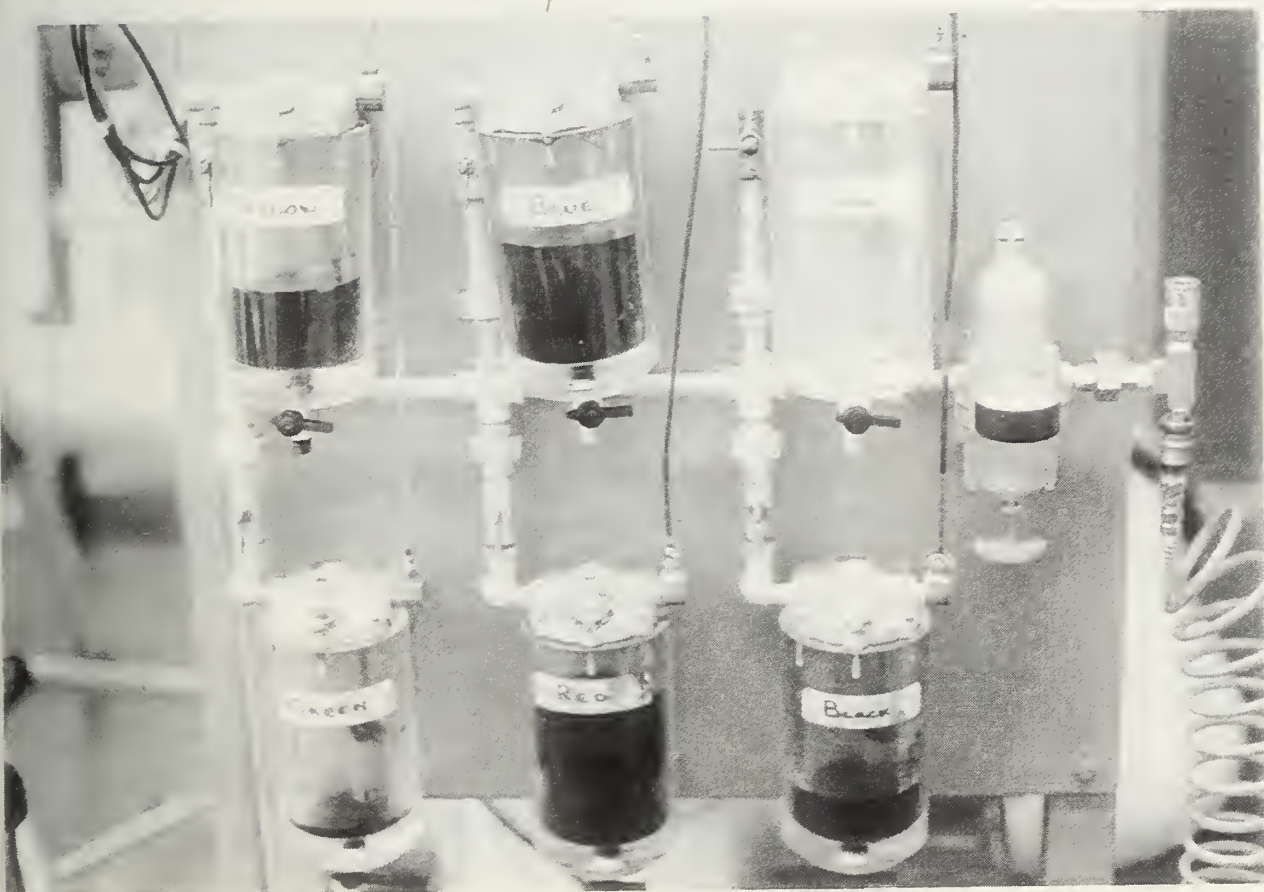


Figure 2.2 Dye Supply System

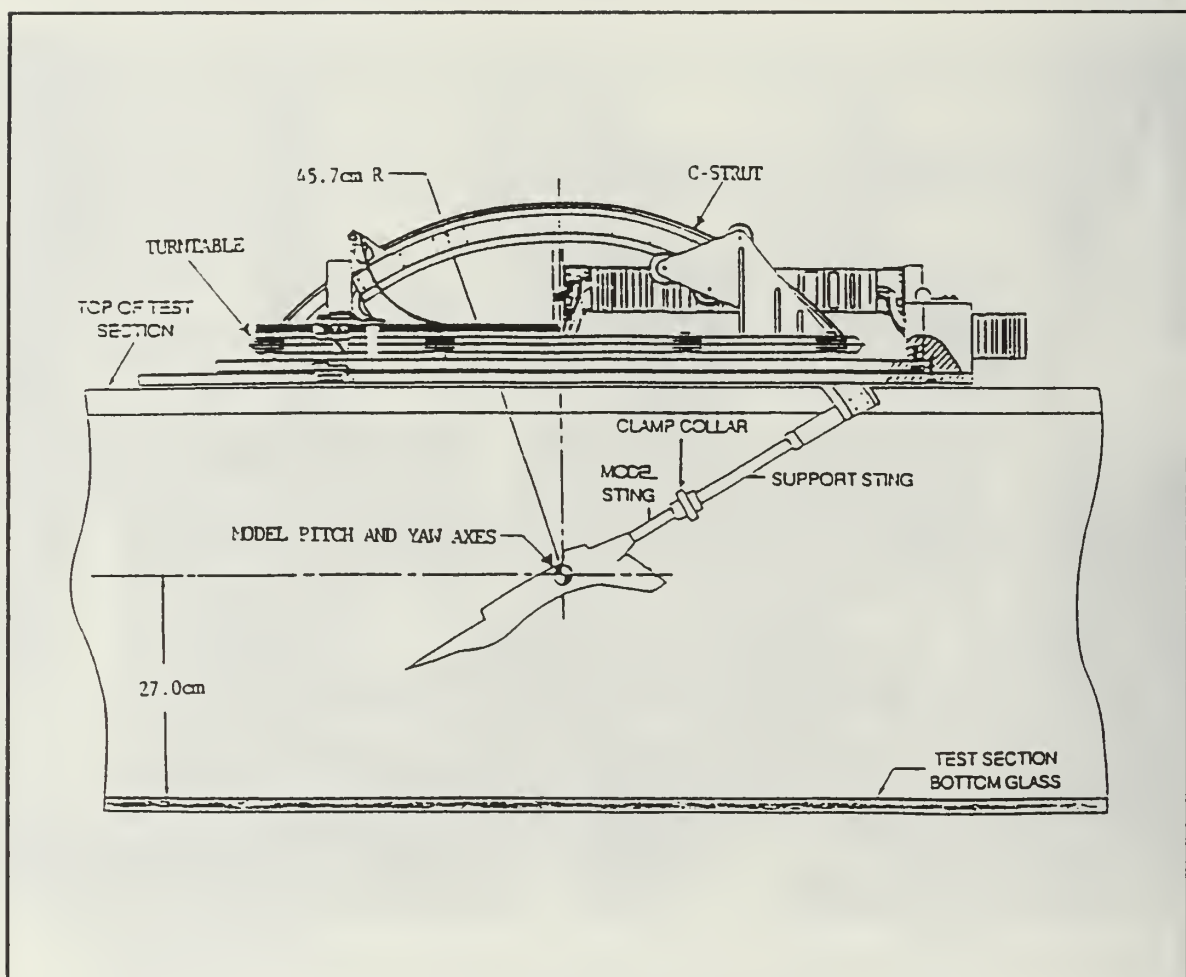


Figure 2.3 Model Support System

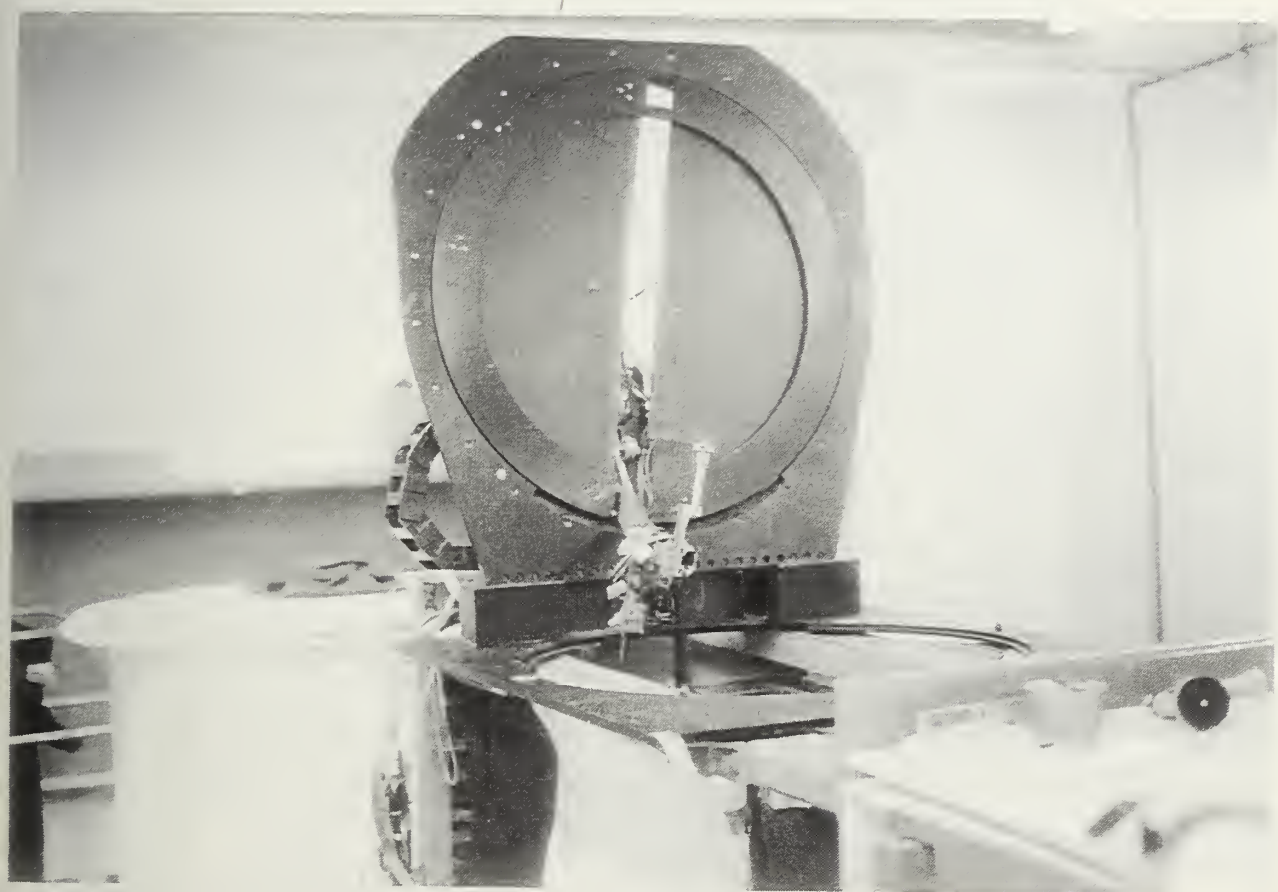


Figure 2.4 Model Support System in the Up Position

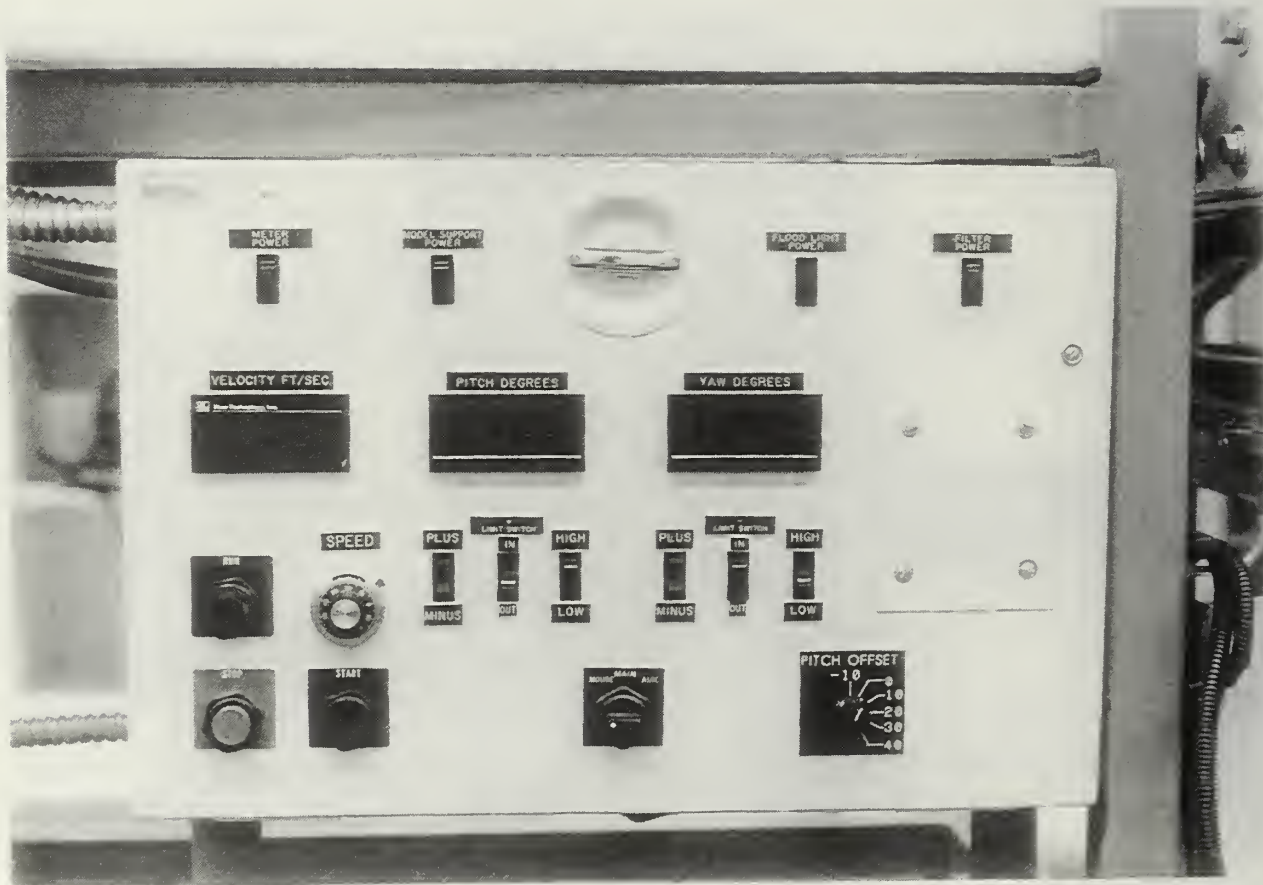


Figure 2.5 Control Panel

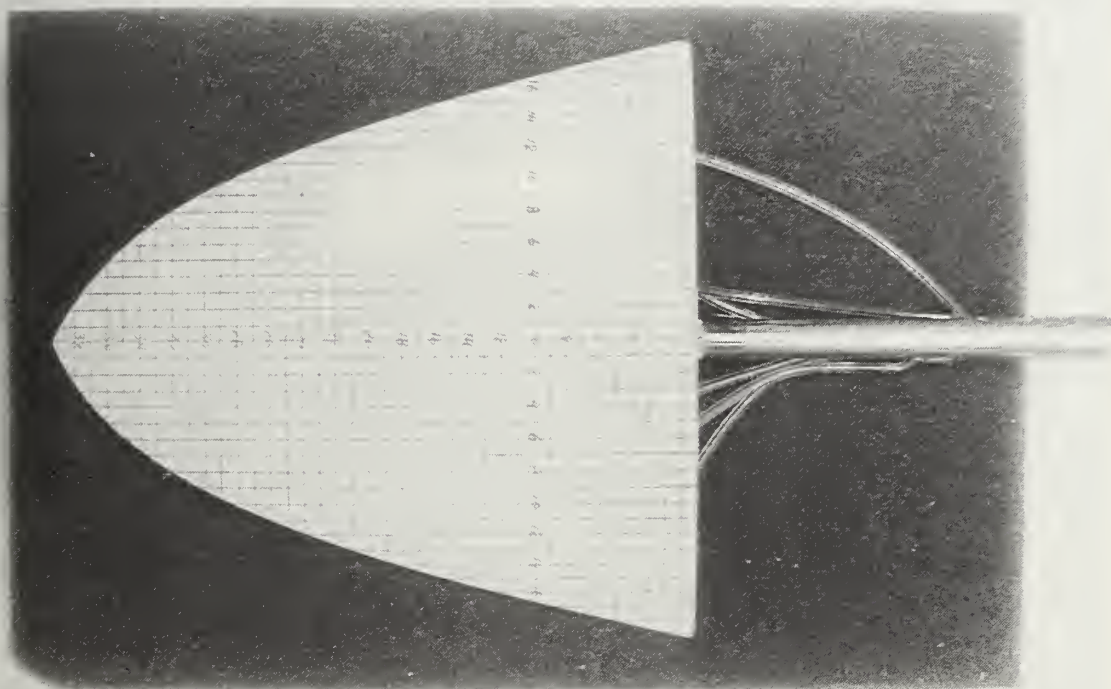


Figure 2.6 Top View of Waverider Model



Figure 2.7 Bottom View of Waverider Model

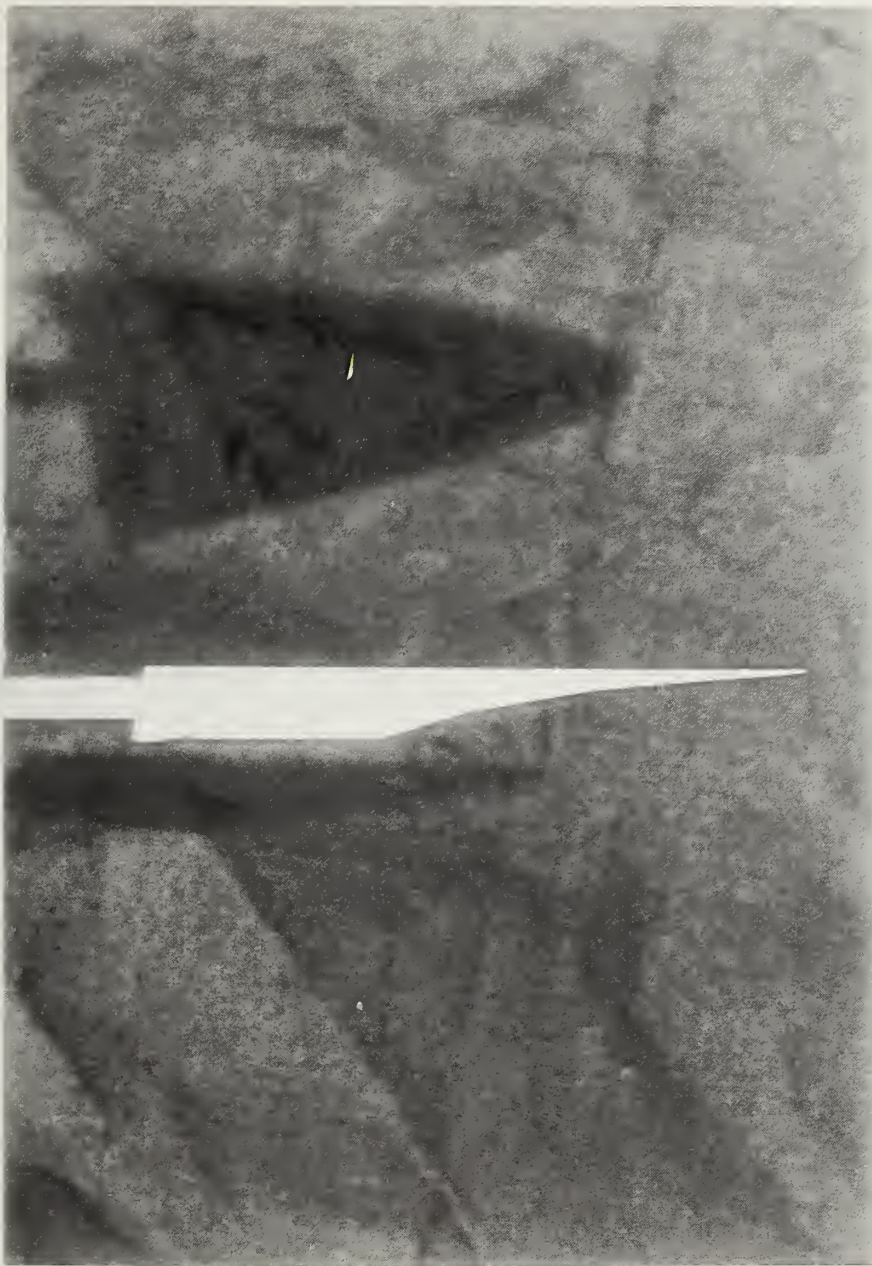


Figure 2.8 Side View of Waverider Model



Figure 2.9 Front View of Waverider Model

III. RESULTS/DISCUSSION

Vortex core trajectory and burst location data were recorded for a pitch range of 2° to 12° and yaw range of 0° to 10° for the unmodified model. For the modified models the pitch range was from 4° to 24° and the yaw range was from 0° to 10° . The yaw range was set arbitrarily but the lower pitch limit represents the pitch angle at which the vortex begins to form over the top surface of the model and the upper pitch angle limit represents the pitch angle at which the vortex core burst point has reached the leading edge. The flow velocity in the tunnel was kept at 0.26 ft/sec that corresponded to a Reynolds number of 24600/foot (16140 based on the centerline chord). The top surface of the waverider was used as the angle-of-attack reference with 0° occurring when this flat surface was parallel to the oncoming flow. The model pitch axis was located at mid-chord ($x/c=0.5$) where "c" represents the centerline chord which is equal to the body length of 7.875 inches.

Vortex core trajectories and burst locations were visually determined from video frames and still photos taken during testing. Due to the unsteady nature of vortices, the burst location at any angle-of-attack fluctuated an average of eight percent of the centerline chord (0.6 inches), therefore for the purposes of data reduction, average values of burst point location were determined. Some degree of imprecision may be present in the reduced data due to the difficulty associated with actually locating the burst points of weak or washed out vortices as was usually the case for the windward side of the model during yaw testing. All data was nondimensionalized using the centerline chord length. Note that the angle-of-attack indication in the side view photographs is not necessarily the true

angle-of-attack as the side view camera was not always focused exactly at the fuselage centerline of the model. The true angle-of-attack was read from the digital indicator on the control panel.

The test procedure consisted of setting a yaw angle and increasing angle-of-attack until the burst point had traversed to the leading edge. Table 3.1 shows the test matrix.

TABLE 3.1 TEST MATRIX

Configuration	Sideslip Angle	Pitch Angle
unmodified	0°, 5°, 10°	2°-12°*
modified	0°, 5°, 10°	4°-24°#

*1° increments, #4° increments

A. BASELINE CONFIGURATION

The unmodified configuration refers to the basic waverider model. To aid in data reduction, a square grid was applied to the top and bottom surfaces of the model. The grid squares are 0.2 inches on each side and are referenced to the model's trailing edge and the model centerline. All burst point locations and vortex core lateral positions in the following discussion are referenced to the model trailing edge and centerline respectively.

1. Angle of Attack Effects on Vortex Stability

Figures 3.1 through 3.3 show the zero yaw vortex burst progression over the top of the wing as angle-of-attack is increased. As can be seen from the photos, vortex bursting is symmetric and the burst behavior is analogous to delta wing behavior described in Reference 9. At 3° angle-of-attack (Figure 3.1) two symmetric vortices are formed. The cores are not tightly wound and are somewhat broken indicating a relatively weak structure. The burst position is not

well defined but is located approximately at 30% of the root chord. At 6° angle-of-attack (Figure 3.2) the vortex core is more tightly wound indicating greater strength. The burst position is well defined and has moved forward symmetrically from its 6° angle-of-attack position to 74% of the root chord. At 9° angle-of-attack (Figure 3.3) the burst position is symmetric and has moved to 86% of the root chord and at 12° angle-of-attack (Figure 3.4) the vortex is completely turbulent over the top of the model with the burst position positioned at 94% of the root chord. As the angle-of-attack is increased to 15° , 17.5° and 20° (Figures 3.5, 3.6, and 3.7 respectively) it can be seen that the flow over the top surface of the model is completely separated.

Figure 3.8 illustrates quantitatively the vortex breakdown characteristics of the waverider compared to delta wings of various sweep angles. Here and in all the burst location plots that follow, x/c values of 0 and 1.0 correspond to vortex breakdown at the wing trailing edge and wing apex, respectively. The results show that vortex breakdown occurs much sooner for the waverider than for any of the delta wings. This could be due in part to the low sweep angle of the waverider planform near the apex, which is approximately 35° . The delta wing data suggests that increasing leading edge sweep angle delays vortex bursting. The waverider data of figure 3.8 indicates that this waverider configuration generates much less vortex lift than a similar aspect ratio delta wing which brings up the question; will it generate enough lift to allow it to take-off and land? That question can only be answered after low speed wind tunnel testing is completed. These results may not be as bad as they first appear. It has been determined in previous wind tunnel tests of similar waverider configurations that the very diffuse core of a broken or burst vortex still has

strong circulation and a large static suction and that the low-speed characteristics of waverider wings should not present any more difficulties than those of current slender delta wings [Ref. 14]. It is interesting to note that the rate of vortex burst progression over the aft end of the waverider where the sweep is constant at 75° is comparable to that of the 75° delta wing.

To get a more complete picture of the flow characteristics over the top of the model at angle-of-attack, dye was introduced into the flow at arbitrary points along the leading edge. Figure 3.9 shows the model at 0° yaw and 4° angle-of-attack. Dye is being injected at 74% of the root chord from the trailing edge (position 1), 86% of the root chord from the trailing edge (position 2), and at the apex. Note that the apex vortex and the right side, position 2, vortex core appear to split. This is due to an excess amount of dye being injected at these points while the vortex is too weak at this low angle of attack to entrain all of the dye. This effect is not seen on the left because a smaller amount of dye is being injected there due to a slight difference in dye injection rate between the left and right sides. This difference can be attributed to slight variations in dye port diameter and other equipment variations and is only evidenced at these low angles of attack. Also notice that the position 1 and 2 dye streams become entrained in the apex vortex. At 8° angle-of-attack (Figure 3.10) entrainment of the dye is more clearly seen. At 10° angle-of-attack (Figure 3.11) the vortex core burst position has moved ahead of the positions 1 and 2 injection points but it is evident that the dye being injected at these points is being entrained in the turbulent vortex. As can be deduced from these photos, there are two primary vortex cores present, one on each side of the model, and they originate at the apex and are symmetric over the angles of attack of this study .

2. Sideslip Effects on Vortex Core Stability

Figures 3.12-3.14 reveal the vortex burst asymmetry that is present due to sideslip. Vortex burst asymmetry refers to the difference in the burst location of the leeward core compared to windward core. Leeward refers to side of the model that is away from the flow and windward refers to the opposite side of the model which is angled into the flow. All side photographs are of the leeward side of the model. These figures show the model at 7° angle-of-attack with sideslip angles of 0° , 5° , and 10° respectively. At 0° yaw (Figure 3.12) a pair of well developed, strong and symmetrical vortices are visible with both vortex cores bursting at about 76% of the root chord. As the sideslip angle is increased to 5° (Figure 3.13) a pair of asymmetrical vortices develops with the leeward vortex burst point moving aft of its 0° yaw position to 63% of the root chord while the windward vortex appears washed out with the burst point having moved forward of its 0° yaw position to approximately 85% of the root chord. At 10° of sideslip (Figure 3.14) the leeward vortex appears more stable and well defined and the burst point has moved to 46% of the root chord. The windward vortex appears less washed with no apparent movement in burst location from its 5° sideslip location of 85% of the root chord.

Figures 3.15-3.19 illustrate the flow field over the top of the waverider at a constant 10° of sideslip as the angle-of-attack is increased from 2° to 9° . At 2° angle-of-attack (Figure 3.15) the leeward vortex core is weak but well defined showing no sign of bursting. The windward vortex appears washed out with no defined core. Through slow motion video analyses a weak core was determined to be present with a burst point located at 51% of the root chord. At 4° angle-of-attack (Figure 3.16) the leeward core structure appears more well defined and

stable than at 2° angle-of-attack with still no sign of bursting. The windward core appears washed out but the burst point was estimated to be at 76% of the root chord.

At 5° angle-of-attack (Figure 3.17) the leeward core still appears to be strong with bursting evident but not well defined at approximately 10% of the root chord. The windward core is still not well defined but the burst point was determined to be at 81% of the root chord.

At 7° angle-of-attack (Figure 3.18) the leeward burst point has moved to approximately 51% of the root chord. The windward vortex core is more well defined indicating increased strength with the burst point located at approximately 86% of the root chord length.

At 9° angle-of-attack (Figure 3.19) the leeward burst point has moved forward of its 7° angle-of-attack position to 86% of the root chord and the windward burst point has also moved forward of its 7° angle of attack position to 91% of the root chord. It appears that the vortex burst asymmetry present at lower angles of attack is greatly reduced as the angle-of-attack increases. This result indicates that this waverider may have less roll due to yaw, caused by the asymmetric vortex lift, when compared to a similar aspect ratio delta wing and may therefore be a more forgiving aircraft during cross wind takeoff and landing maneuvers.

As depicted in Figures 3.20a and 3.20b vortex burst asymmetry for the $M=6$ waverider design is reduced as angle-of-attack is increased. This reduction is indicated by the pinching together of the five waverider burst position vs. angle-of-attack curves at the higher angles of attack. This result may be misleading due to the relatively narrow initial separation of the curves and the

relatively large margin for error in measuring the actual burst location. Note that the 70° delta wing data used for comparison (Figure 3.20b) shows a much wider and constant spread among the burst position vs. angle-of-attack curves indicating greater vortex burst asymmetry at all angles of attack compared to the waverider.

3. Angle of Attack effects on Vortex core Trajectory

Figure 3.21 illustrates the angle-of-attack effect on vortex core lateral position. Here y/c refers to the nondimensionalized lateral position of the vortex core as measured from the model centerline prior to bursting or streamwise deflection at the trailing edge. Lateral position was measured at seven arbitrarily spaced longitudinal positions. The absence of a data point at a given angle-of-attack implies that the vortex core has burst and does not extend to that longitudinal position.

As can be seen in Figure 3.21, the lateral position of the vortex core at 0° of sideslip is essentially constant with angle-of-attack. The largest variation, which is located at $x/c=0.914$, represents about 2.5% of movement based on the centerline chord and therefore, could be classified as due to the previously discussed experimental error. This result is in agreement with previous water tunnel delta wing flow studies which show that vortex core lateral position for a given wing sweep is insensitive to angle-of-attack changes [Ref. 11, 13]. Figure 3.22 compares the waverider lateral vortex core to previous delta wing results [Ref.13]. As can be seen the lateral location of the waverider vortex core is outboard of all the delta wing vortex core locations and that the vortex core is curved to follow the waverider leading edge. This behavior is different from delta wing vortex core trajectory behavior in that delta wing vortex core sweep

angles are always slightly greater than the sweep angles of their respective leading edges [Ref. 13]. The close proximity of the waverider vortex core to its leading edge may contribute to higher rolling moments during conditions of asymmetric vortex lift (i.e. sideslip maneuvers).

4. Sideslip Effects on Vortex Core Trajectory

The effect of sideslip on windward and leeward vortex core lateral position is presented in Figures 3.23 and 3.24. The leeward data (Figure 3.23) indicate that as sideslip increases the vortex core moves away from the model centerline which agrees with previous delta wing results [Ref. 13, 14]. The windward data (Figure 3.24) shows no clear pattern as to the lateral movement of the vortex core with sideslip. This could be due to the generally poor structure of the windward core which makes it difficult to obtain accurate data points as to the actual core location. Typical behavior is for the windward core to move inboard of its 0° yaw position as sideslip is increased.

B. APEX DELTA

To increase vortex core stability and delay vortex bursting, various high lift concepts were recommended by personnel at the NASA Ames Research Center. Time limitations associated with the completion of this thesis permitted the testing of only one of these concepts, known as the apex delta. This device consists of a small flat plate delta planform that is attached at the apex of the waverider; the idea being to take advantage of the increased vortex generating capability of the delta planform compared to this waverider.

Leading edge sweep effects as well as planform area ratio effects were investigated. Planform area ratio refers to the ratio of the exposed planform area of the small delta to that of the waverider. Table 3.2 gives the three modifications

tested. Appendix B gives the details of the design, construction and assembly of these apex delta modifications.

For practical reasons the model grid size was increased to one half inch. This reduced the time required to grid the model without reducing data resolution. To facilitate direct comparison of the unmodified model results with the modified model results, all burst point locations in the following discussion are nondimensionalized utilizing the unmodified model root chord length of 7.875 inches and referenced with respect to the models trailing edge. Lateral vortex core locations are referenced, as before, from the model centerline and nondimensionalized utilizing the unmodified model root chord length.

TABLE 3.2 APEX DELTA MODIFICATIONS TESTED

Modification	Sweep Angle	Area Ratio
1	65°	0.5%
2	65°	2%
3	55°	2%

C. MODIFICATION ONE

As mentioned above, modification one has a 65° sweep angle and an area ratio of 0.5% as seen in Figures B.1-B.7. Figures 3.25-3.27 show the zero sideslip flow field as the angle-of-attack is increased from 4° to 10° . To investigate the possibility of the formation of two primary vortex cores, dye is being injected into the flowfield at the apex of the apex delta and at the kink formed by the juncture of the apex delta and the waverider leading edge. It was thought that due to the abrupt change in curvature of the leading edge that possibly two primary vortex cores would be generated; one at the apex of the apex delta and the other at the kink. At 4° angle-of-attack (Figure 3.25) two vortex cores are present on each

side of the model; one originating at the apex of the apex delta and a weaker looking vortex core originating at the junction of the apex delta and the waverider leading edge (the kink vortex). The apex and kink vortex cores rotate in the same direction on each side of the model. The vortices on the left side of the model rotate clockwise and the vortices on the right side of the model rotate counter clockwise in the rear view. At 6° angle-of-attack (Figure 3.26) the apex vortex appears stronger and becomes entrained with kink vortex. Figure 3.27 shows that the vortices are still entrained at 10° angle-of-attack and Figures 3.28 and 3.29 show that the vortices are entrained for a constant 10° of sideslip and 8° and 12° angle-of-attack respectively.

It can be deduced from the above discussion that at 4° angle-of-attack the vortices do not interact but as the angle-of-attack is increased, the two vortices become entwined together to form one primary vortex core on each side of the model.

1. Angle of Attack Effects

Figures 3.30-3.34 show the model at 0° sideslip while angle-of-attack is increased from 2° to 20° . At 2° angle-of-attack (Figure 3.30) two symmetric vortex cores are present. The vortex structure is so weak that the core becomes deflected in the streamwise direction at approximately 76% of the root chord. A well defined vortex burst point is not evident. At 6° angle-of-attack (Figure 3.31) vortex core structure is well defined and appears stronger, with the vortex core moving outward from the centerline. The lateral trajectory appears linear and does not follow the curvature of the leading edge as was the case for the baseline model. The vortex burst position is located at approximately 70% of the root chord. At 12° angle-of-attack (Figure 3.32) vortex core lateral position is

unchanged and the burst point has moved forward of its 6° angle-of-attack position. Core width appears smaller now compared to the size seen in the two previous photos, possibly indicating increased vortex strength. At 16° angle-of-attack (Figure 3.33) the burst point has moved to approximately 83% of the root chord. At 20° angle-of-attack (Figure 3.34) the burst point is located at the leading edge.

An interesting phenomena of this modification is that the vortex core never extends all the way to the trailing edge as illustrated in Figures 3.30 and 3.25. Figure 3.30 shows a partially developed vortex core at 2° angle-of-attack that loses definition prior to the trailing edge and Figure 3.25 shows two fully developed vortex cores at 4° angle-of-attack with a well defined burst point located well ahead of the trailing edge. From this it would be difficult to predict the angle-of-attack at which maximum lift would occur since maximum lift, as discussed previously for delta wings [Ref. 11], occurs when the burst point is located at the trailing edge.

Figure 3.35 shows that modification one delays vortex core bursting to higher angles of attack compared to the unmodified model. This improvement is due to the slow rate of progression of the burst point once the vortex core has formed (at approximately 4° angle-of-attack). Figure 3.36 shows that the vortex core has moved inboard compared to the unmodified model possibly due to the increased sweep of the apex delta. The above results indicate that this modification increases vortex stability and strength and therefore, would yield higher values of lift for a given angle-of-attack compared to the unmodified model.

2. Sideslip Effects

Figures 3.37-3.39 show the sideslip effects for a constant 8° angle-of-attack. At 0° of sideslip (Figure 3.7) two symmetric vortex cores are present with both burst points located at 70% of the root chord. At 5° of sideslip (Figure 3.38) the windward burst point has moved to 83% of the root chord and the leeward burst point has moved to approximately 44% of the root chord. At 10° sideslip (Figure 3.39) the windward burst point has moved to 89% of the root chord. The leeward core appears darker than the windward core with no defined burst point. The vortex core diameter increases near the trailing edge possibly indicating decreased vortex strength.

Figure 3.40 illustrates the vortex burst asymmetry that is present due to sideslip. Notice that vortex burst asymmetry does not decrease with angle-of-attack as was the case for the baseline model. Figure 3.41 and 3.42 shows the relationship of vortex core lateral position to changes in sideslip and angle-of-attack. The leeward core (Figure 3.41) shifts outboard while the windward core (Figure 3.42) moves inboard with respect to their 0° sideslip positions. Note that the vortex core lateral position is nearly constant with angle-of-attack as seen previously in the baseline results which are in agreement with delta wing results [Ref. 13].

D. MODIFICATION TWO

Modification two has the same 65° sweep as modification one but the area ratio has been increased to 2% as seen in Figure B.8 and B.9 in Appendix B. Once again, to investigate the possibility of the formation of two primary vortex cores on each side of the model, dye is being injected at the apex of the apex

delta and at the kink formed at the juncture of the apex delta and the waverider leading edge.

Figures 3.43-3.46 illustrate the entrainment of the dye over the top surface of the model at angle-of-attack with sideslip held constant at 0° . At 4° angle-of-attack (Figure 3.43) it can be seen that the dye is entrained around the primary vortex core which originates at the apex of the apex delta. At 12° , 16° , and 24° angle-of-attack (Figures 3.4-3.46 respectively) the dye remains entrained around the primary vortex core. Figures 3.47 and 3.48 show the entrainment of the dye at a constant 12° angle-of-attack while sideslip is increased from 5° to 10° . Note again that the dye remains entrained in the primary vortex core even at non-zero sideslip angles. Therefore it can be concluded that one primary vortex is generated on each side of the model and that it originates at the apex of the apex delta.

1. Angle of Attack Effects

Figures 3.49-3.52 illustrate the angle-of-attack effects at zero degrees of sideslip. At 4° angle-of-attack (Figure 3.49) two symmetric vortex cores are present. The burst point is located at approximately 63% of the root chord while at 8° angle-of-attack (Figure 3.50) the burst point has moved to 44% of the root chord. Notice, at 12° angle-of-attack (Figure 3.51) the progression of the burst point has changed directions and moved back to 63% of the root chord. At 20° angle-of-attack (Figure 3.52) the burst point has continued its forward progression to approximately 89% of the root chord.

Figure 3.53 illustrates this result quantitatively. As can be seen, modification two represents an improvement over the baseline in terms of delaying vortex bursting to higher angles of attack and therefore maintaining

increased lift at these higher angles-of-attack compared to the unmodified model, but the progression of the burst point between 4° and 12° angle-of-attack is not typical of documented vortex burst behavior (i.e. vortex burst position traverses from the trailing edge to the leading edge as angle-of-attack is increased) [Ref. 11]. The implications of this atypical behavior on the low-speed flying characteristics of the waverider aircraft can only be explored in the wind tunnel where force and pitching moment data can be measured.

Figure 3.54 shows the lateral vortex core trajectory in relation to the baseline and delta wings. Notice that, the vortex core is moved inboard of the lateral position of the vortex core of the unmodified model. This may be due to the higher sweep angle of the apex delta compared to the waverider. At about 76% of the baseline root chord the apex delta effects are decreased and the core begins to move outboard to the baseline position before bursting. Without the benefits of wind tunnel test results, the effects of this lateral movement of the vortex core are unknown but are probably minimal since the movement is symmetric on both sides of the model.

2. Sideslip Effects

Figures 3.55-3.57 illustrate the sideslip effects on vortex core stability for a constant 8° angle-of-attack. At 0° of sideslip (Figure 3.55) two symmetric vortex cores are present with the burst point located at approximately 57% of the root chord. At 5° of sideslip (Figure 3.56) the leeward burst point has moved to approximately 44% of the root chord while the windward burst point has moved to approximately 63% of the root chord. At 10° of sideslip (Figure 3.57) the leeward vortex core extends past the trailing edge while the windward core burst point has moved to approximately 70% of the root chord.

Figure 3.58 illustrates these results quantitatively. As seen previously in modification one results (Figure 3.40) vortex burst asymmetry does not decrease with angle-of attack. This behavior is analogous to the 70° delta wing results [Ref. 13] also included in Figure 3.58. Figures 3.59 and 3.60 show that the lateral movement of the vortex core with sideslip is in agreement with baseline and modification one results. Note that Vortex core lateral position is constant with angle-of-attack as seen in the baseline and modification one results. These results are analogous to published delta wing results [Ref. 13] and suggest that the low-speed flying characteristics of this modification should not significantly differ from that of a similar aspect ratio delta wing.

E. MODIFICATION THREE

Modification three has the same 2% area ratio as modification two but the leading edge sweep angle has been decreased to 55° as seen in Figures B.10 and B.11 in Appendix B. Figures 3.61-3.63 show the entrainment of the dye over the top of the model at a constant 0° of sideslip as angle-of-attack is increased from 8° to 20° . The dye which is being injected into the flow at two locations; 1) the apex of the apex delta and 2) the juncture of the apex delta and the waverider leading edge; stays entrained around the primary vortex core which emanates from the apex of the apex delta. Figures 3.64-3.66 show that the dye remains entrained when sideslip is increased from 0° to 10° for a constant 12° angle-of-attack. Therefore, as with modification one and two, the addition of the apex delta does not complicate the vortical flowfield with the addition of another primary vortex core.

1. Angle of Attack Effects

Figures 3.70-3.73 illustrate the angle-of-attack effects on vortex core stability. At 4° angle-of-attack (Figure 3.70) the burst point is located at approximately 63% of root chord. At 8° angle-of-attack (Figure 3.71) the burst point has moved to 50% of the root chord and at 12° angle-of-attack (Figure 3.72) the burst point has moved to approximately 57% of the root chord. At 16° angle-of-attack (Figure 3.73) the burst point has moved to approximately 89% of the root chord. These results are illustrated quantitatively in Figure 3.74. As can be seen, this modification delays vortex core bursting compared to the baseline model but also exhibits the same atypical vortex core burst progression seen in modification two.

Figures 3.75 and 3.76 illustrate the angle-of-attack and sideslip effects on vortex core lateral position. As seen in the previous results, the lateral position of the vortex core is insensitive to changes in angle-of-attack.

Figure 3.77 shows the lateral trajectory of the vortex core in relation to the baseline and delta wings. Note that the vortex core is more linear than the two previous modifications (see Figures 3.36 and 3.54). One explanation for this behavior may be that the sweep angle of the waverider leading edge where the apex delta joins the waverider is nearly identical to the sweep angle of the apex delta ($\Lambda=55^\circ$) therefore causing no abrupt change in the overall leading edge sweep at that point.

2. Sideslip Effects

Figures 3.71, 3.78 and 3.79 illustrate the sideslip effects on vortex core stability for a constant 8° angle-of-attack. As sideslip is increased from 0° (Figure 3.71) to 5° and 10° (Figure 3.78 and 3.79 respectively) the familiar pattern of the

leeward burst point extending towards the trailing edge and the windward burst point moving toward the leading edge can be seen. Figures 3.72, 3.80 and 3.81 show the same pattern for a constant 16° angle-of-attack. Figure 3.82 illustrates this result quantitatively. Note the lack of a data point at 20° angle-of-attack on the 10° leeward side. Here the vortex core became very unstable, oscillating at a high frequency. This onset of this instability was very abrupt as is seen in the increasingly steep slope of the of the 10° leeward side curve. For this reason this modification was considered to be the least desirable of the three modifications tested.

Figures 3.75 and 3.76 show the lateral movement of the vortex core with sideslip. As seen in the previous baseline and modification one and two results, the leeward core moves inboard of its 0° sideslip position and the windward core moves outboard of its 0° sideslip position.

The side view photos of Figures 3.64-3.66, which are of the leeward vortex core, show that the height of the leeward vortex core above the top surface of the model increases with increasing sideslip. This effect is further illustrated in Figures 3.67-3.69. At a constant 8° angle-of-attack, sideslip is changed from $+5^\circ$ (Figure 3.67) to 0° (Figure 3.68) and finally to -5° (Figure 3.69). Note that the vertical distance of the vortex core above the model top surface decreases with decreasing sideslip. This result is in agreement with delta wing flow visualization results [Ref. 13] and suggests the lateral-directional characteristics of this modification may be analogous to similar aspect ratio delta wings.

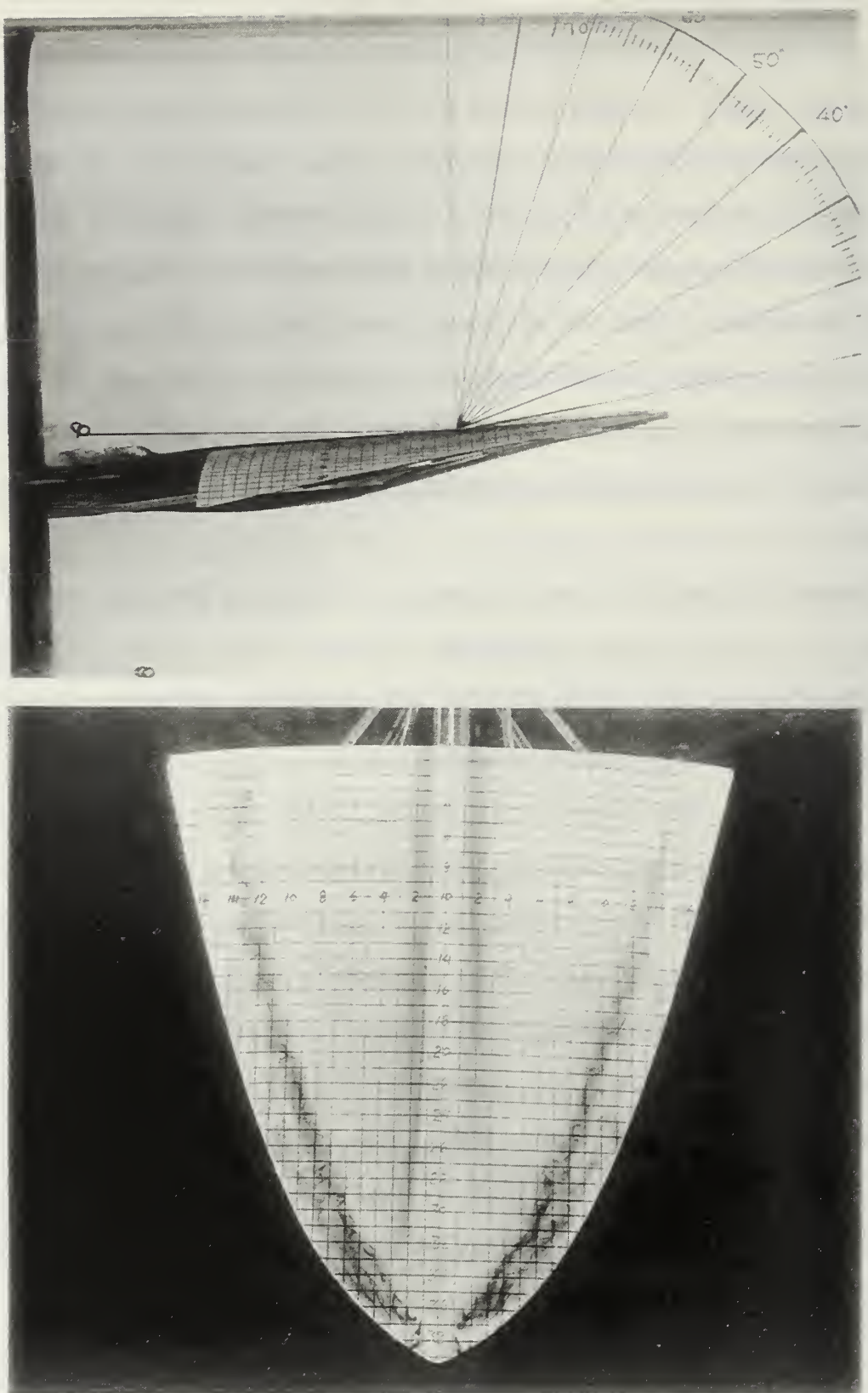


Figure 3.1 Angle of Attack Effects, Baseline Model, $\alpha=3^\circ$, $\beta=0^\circ$

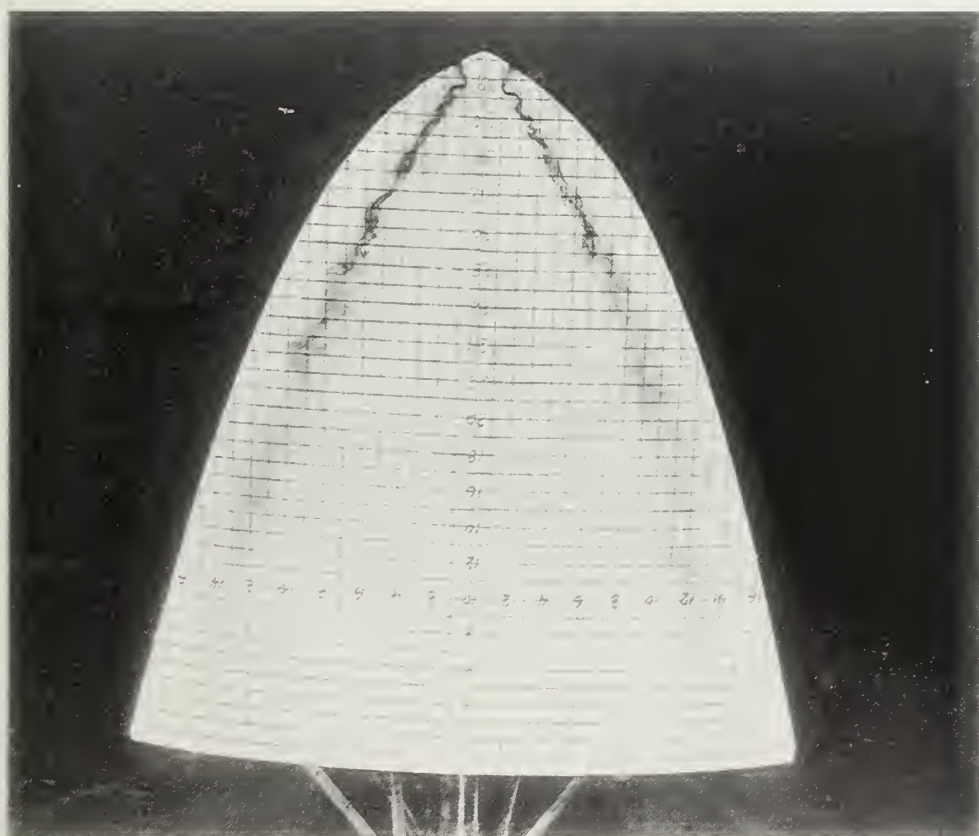


Figure 3.2 Angle of Attack Effects, Baseline Model, $\alpha=6^\circ$, $\beta=0^\circ$

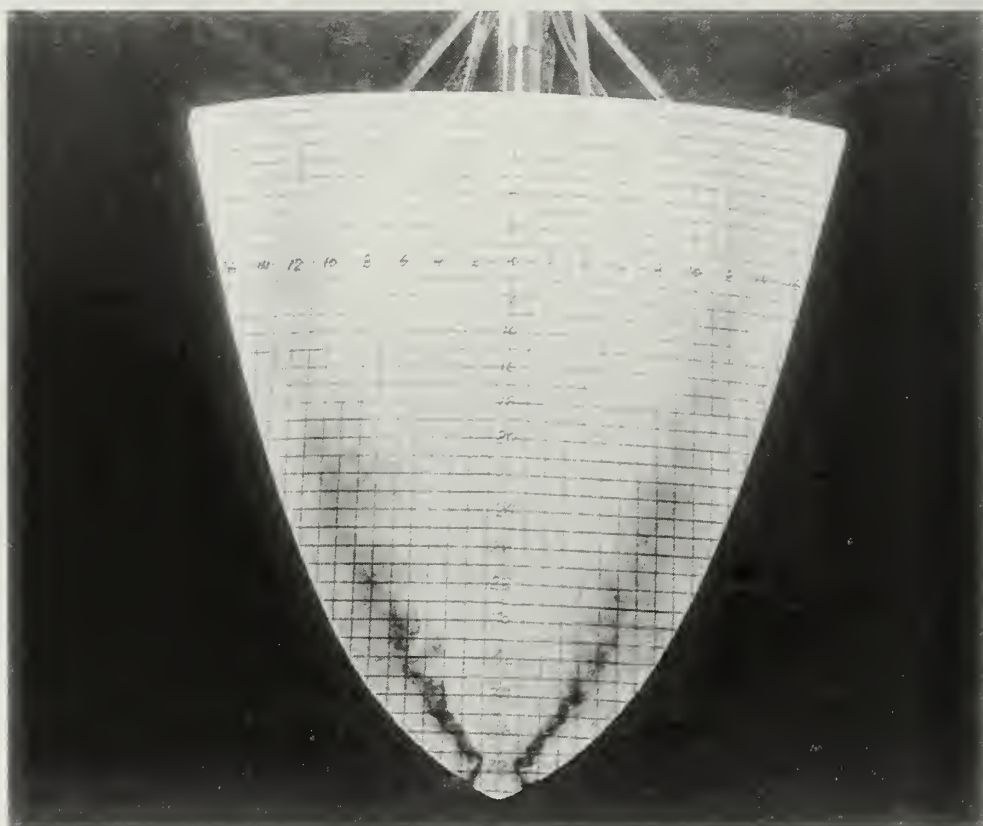


Figure 3.3 Angle of Attack Effects, Baseline Model, $\alpha=9^\circ$, $\beta=0^\circ$

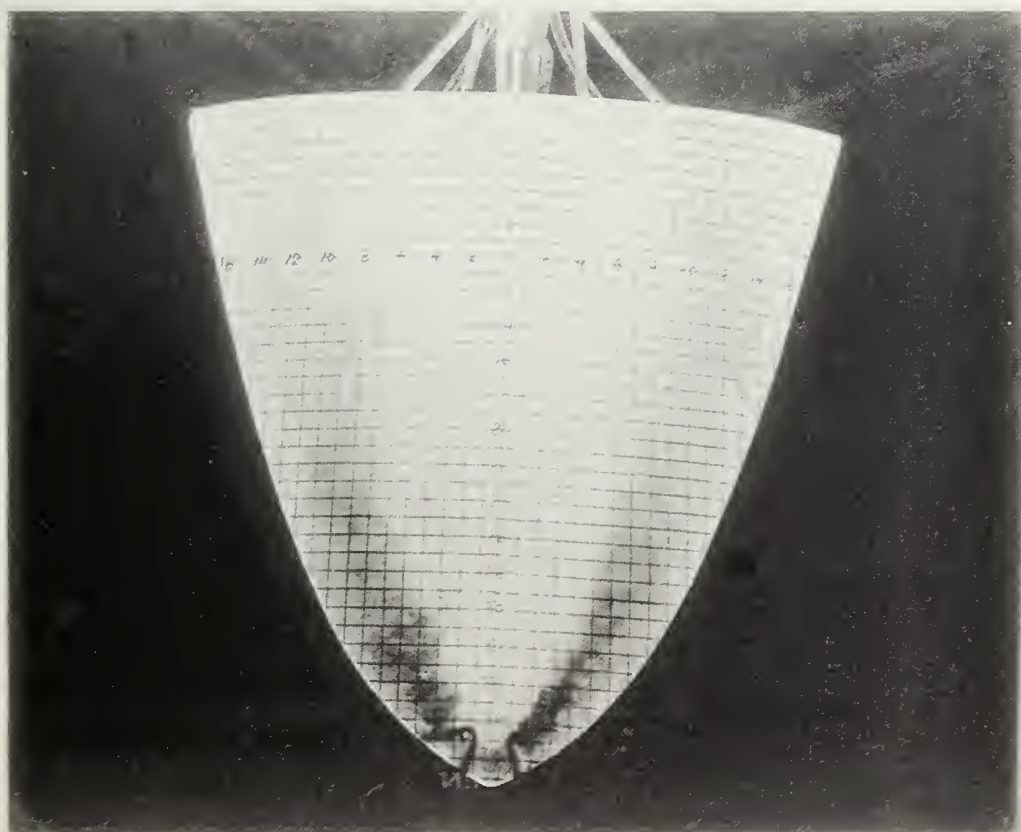


Figure 3.4 Angle of Attack Effects, Baseline Model, $\alpha=12^\circ$, $\beta=0^\circ$

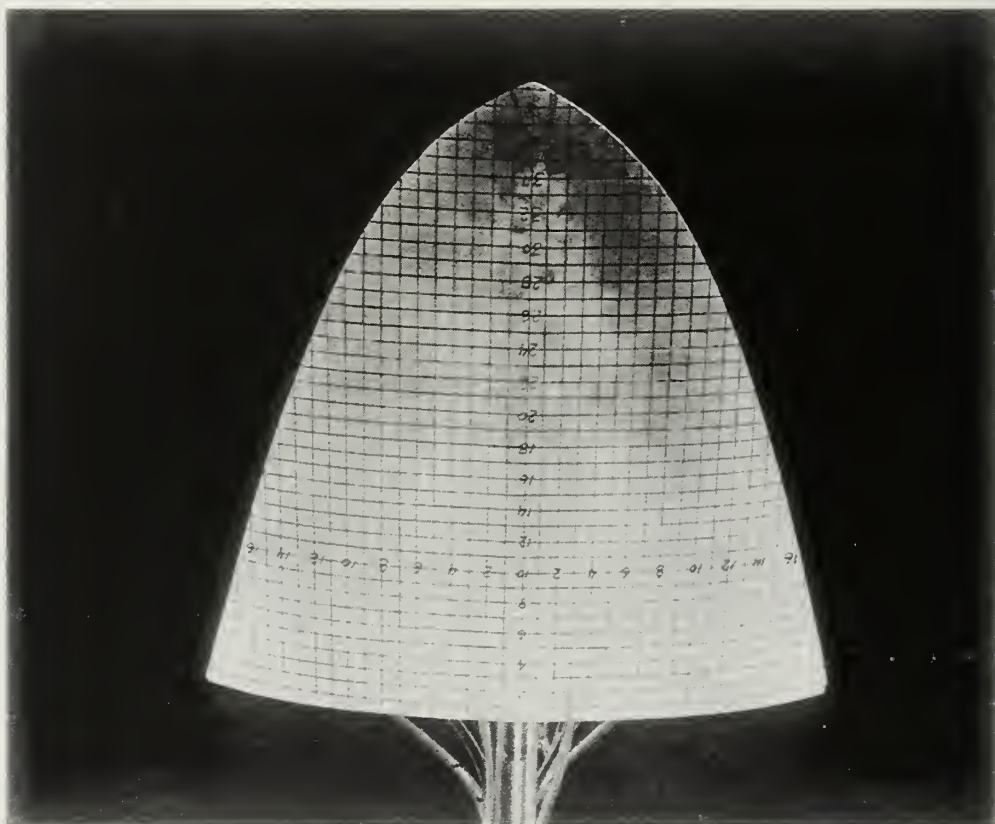


Figure 3.5 Angle of Attack Effects, Baseline Model, $\alpha=15^\circ$, $\beta=0^\circ$

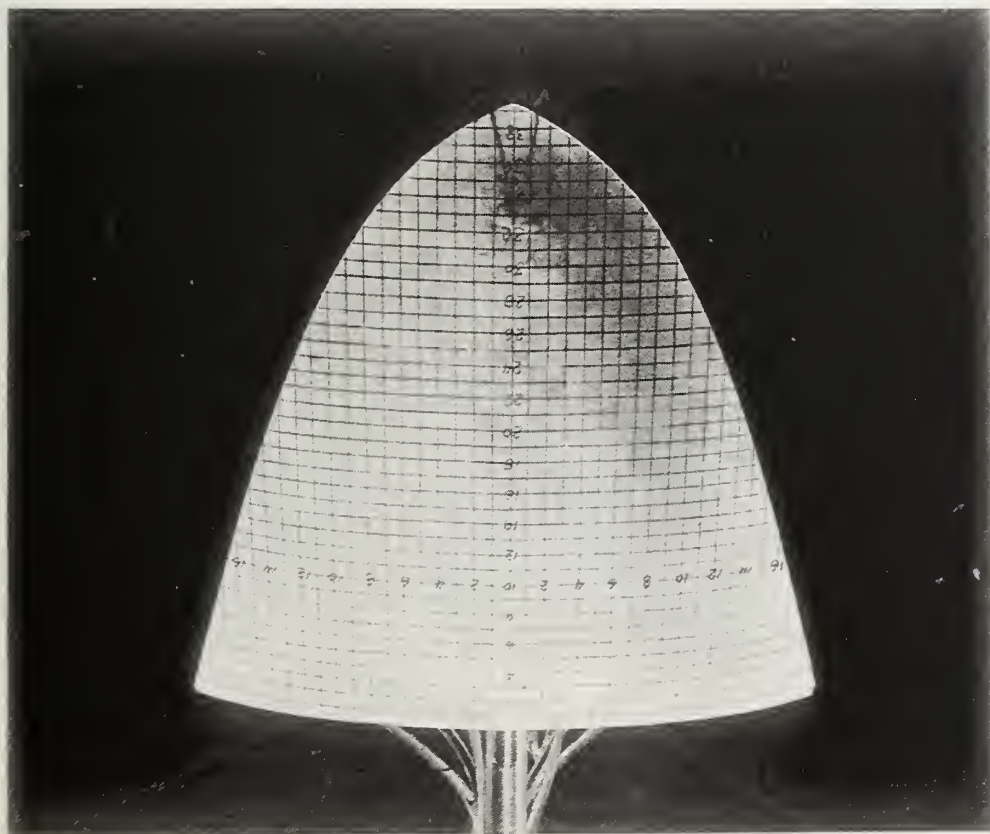
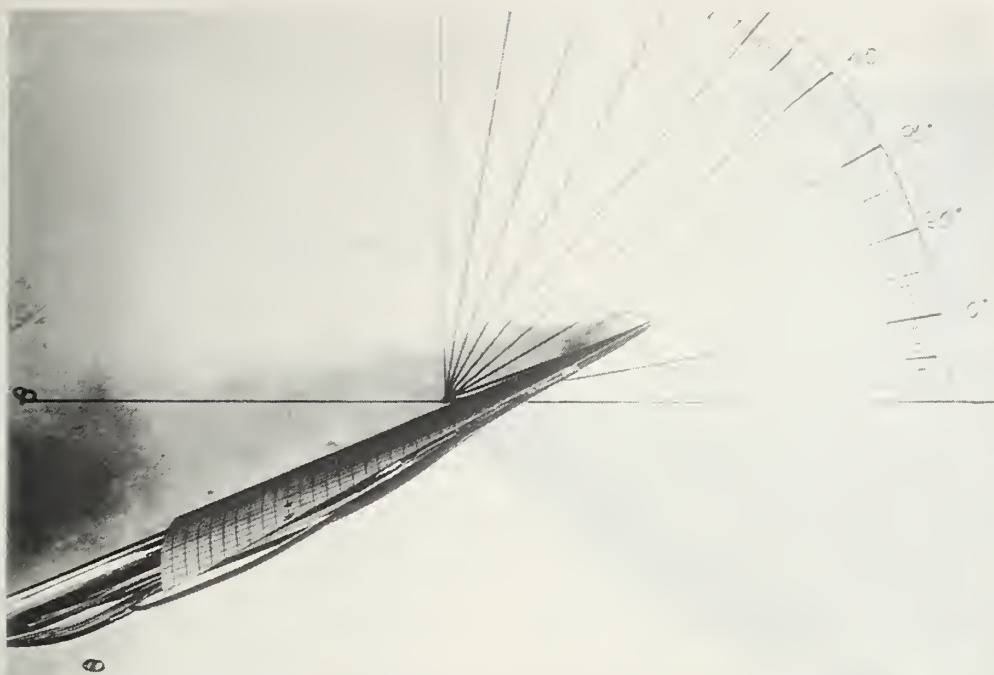


Figure 3.6 Angle of Attack Effects, Baseline Model, $\alpha=17.5^\circ$, $\beta=0^\circ$

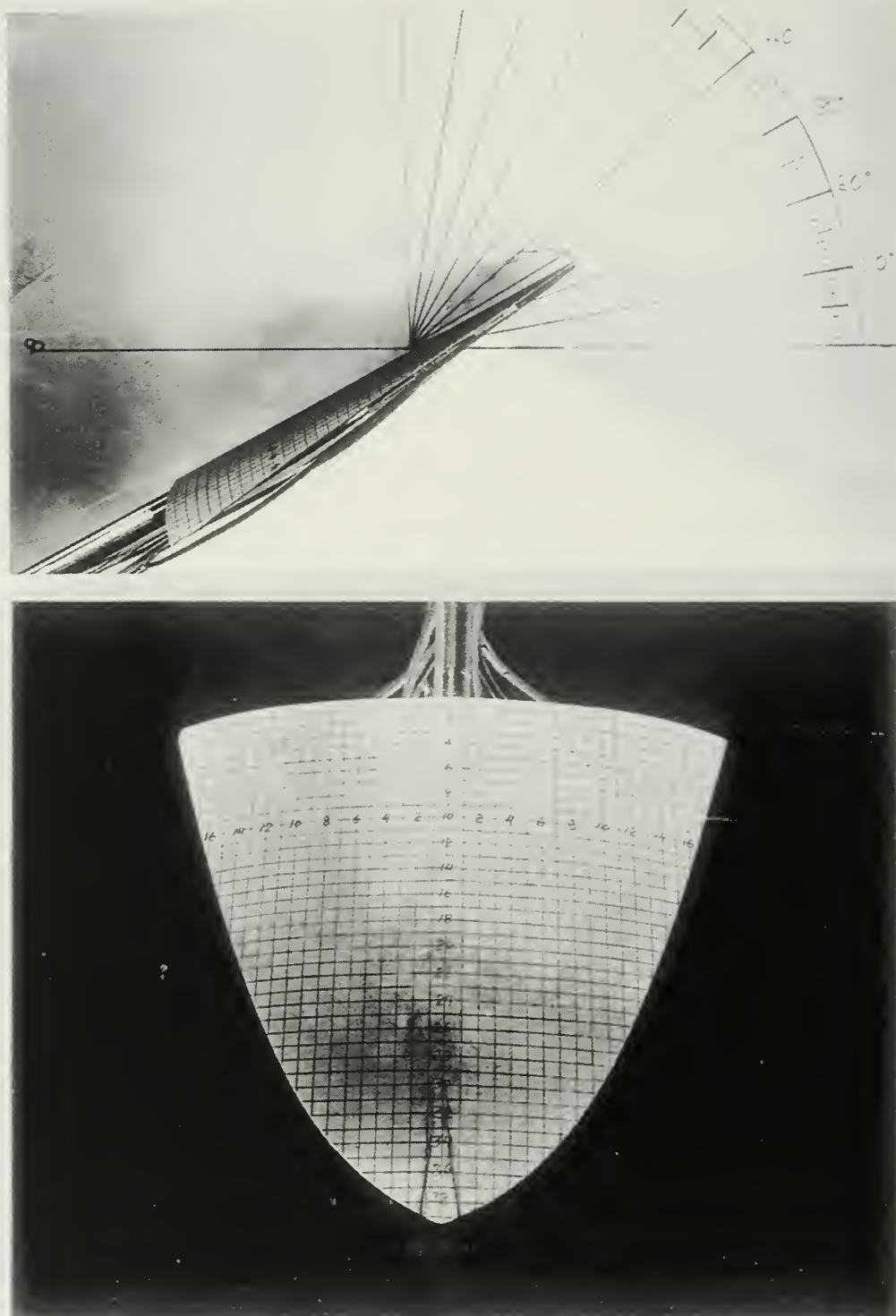


Figure 3.7 Angle of Attack Effects, Baseline Model, $\alpha=20^\circ$, $\beta=0^\circ$

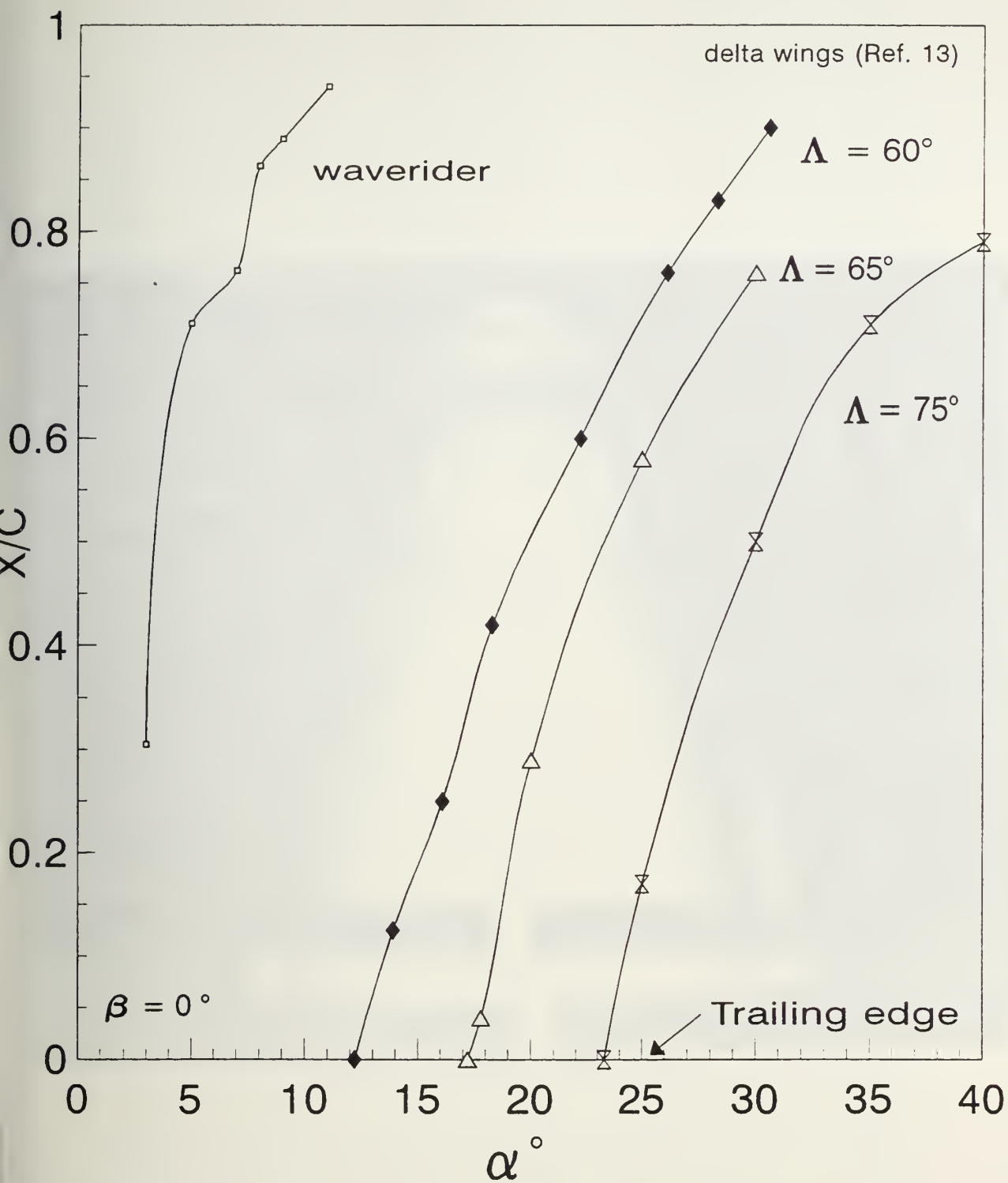


Figure 3.8 Vortex Burst Location as a Function of Angle of Attack, Baseline Model Compared to Delta Wing, $\beta=0^\circ$

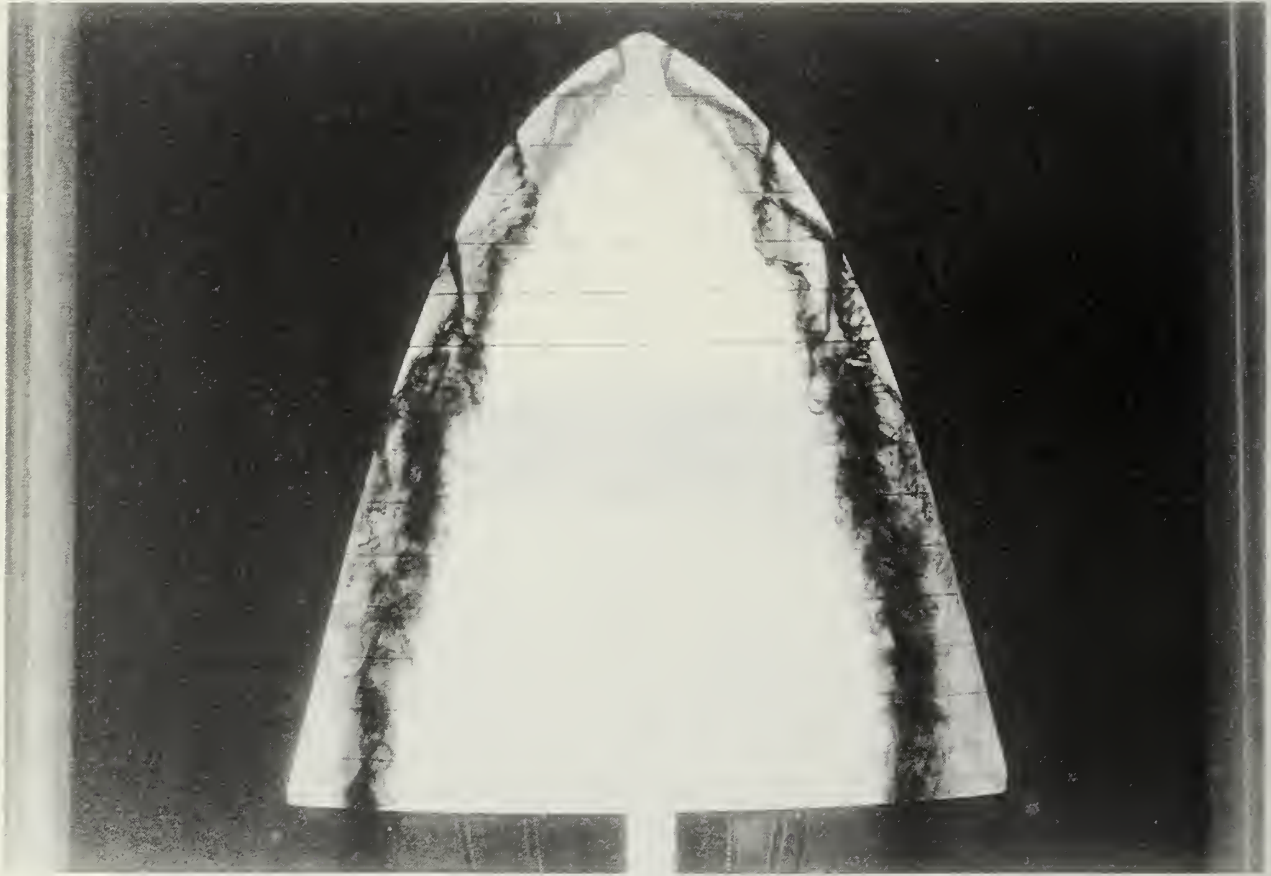


Figure 3.9 Baseline Model, Entrainment. $\alpha=4^\circ$, $\beta=0^\circ$

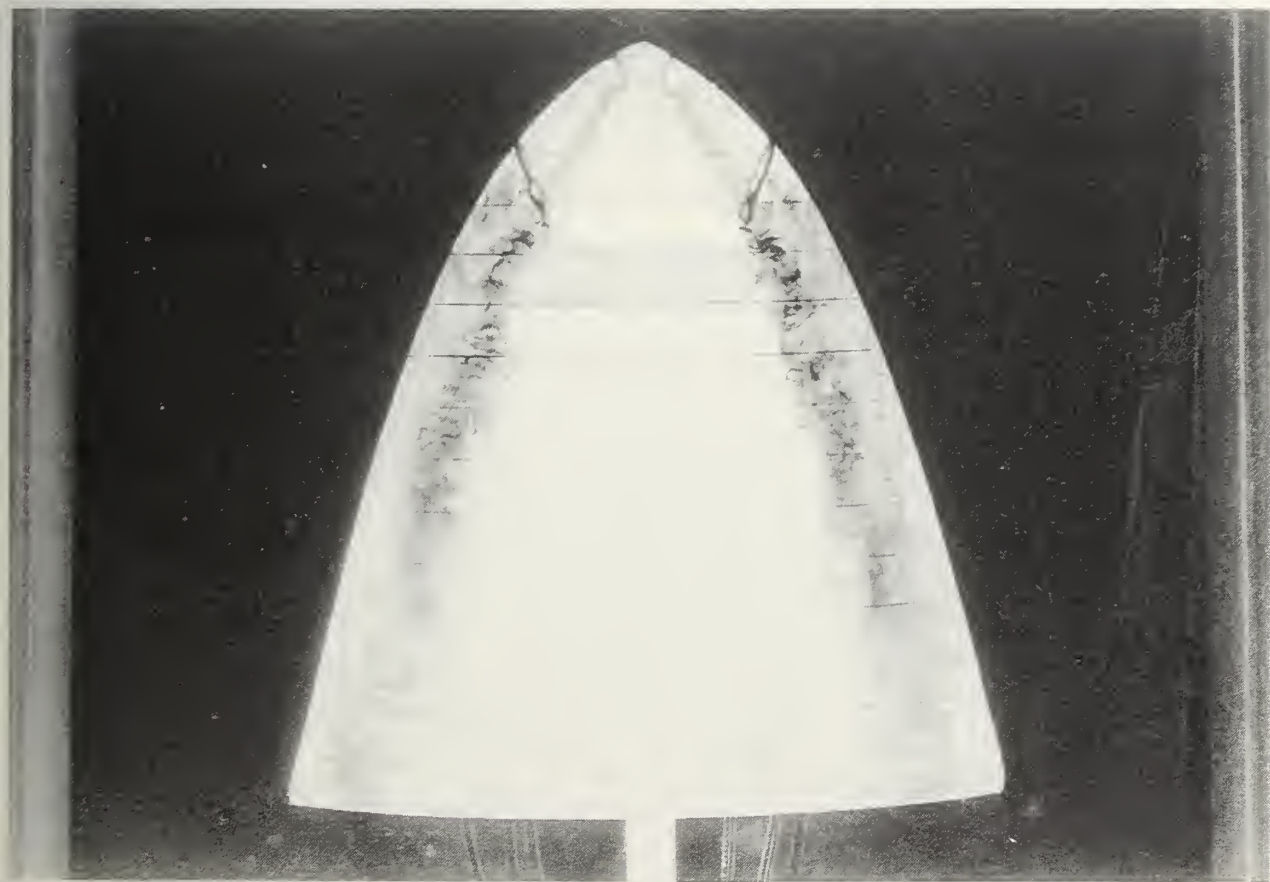


Figure 3.10 Baseline Model, Entrainment, $\alpha=8^\circ$, $\beta=0^\circ$

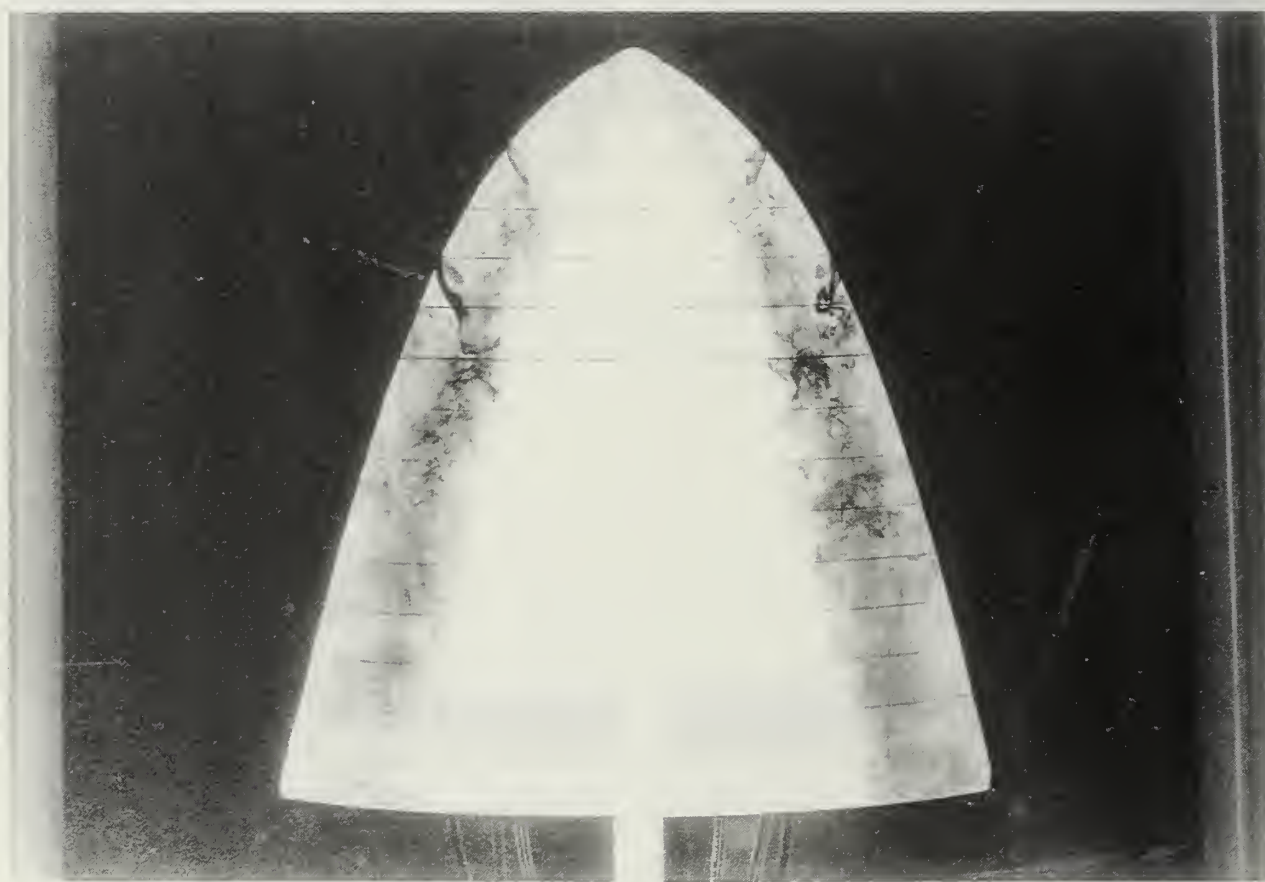


Figure 3.11 Baseline Model, Entrainment, $\alpha=10^\circ$, $\beta=0^\circ$

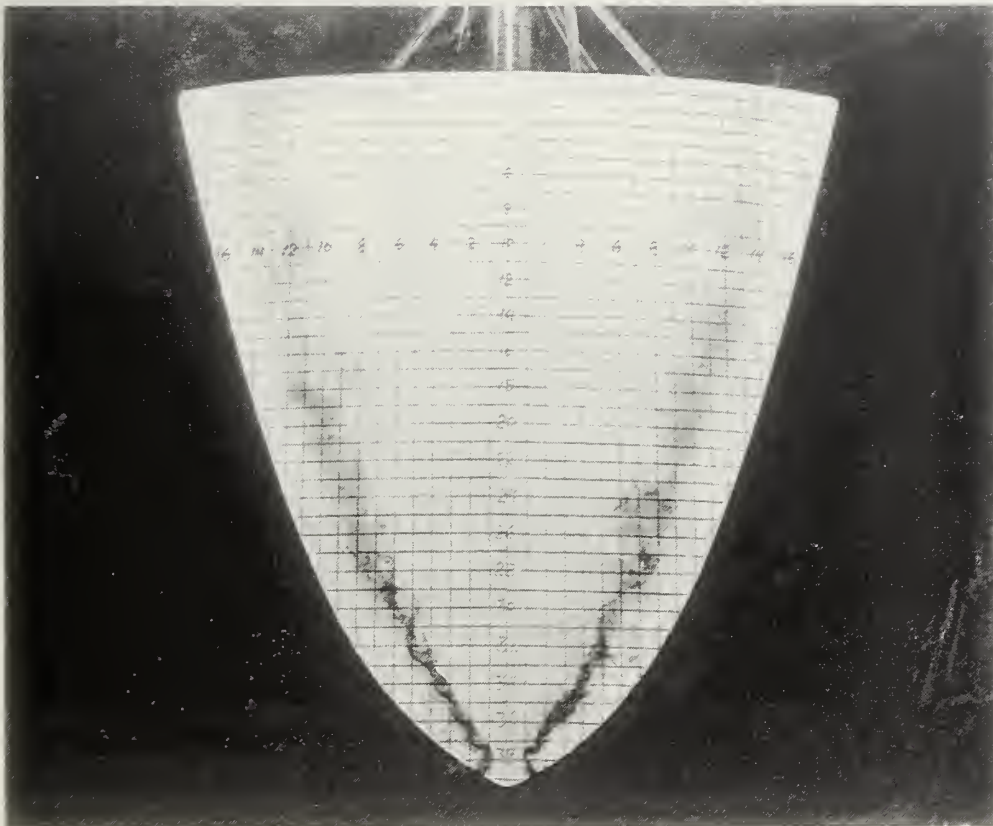


Figure 3.12 Sideslip Effects, Baseline Model, $\alpha=7^\circ$, $\beta=0^\circ$

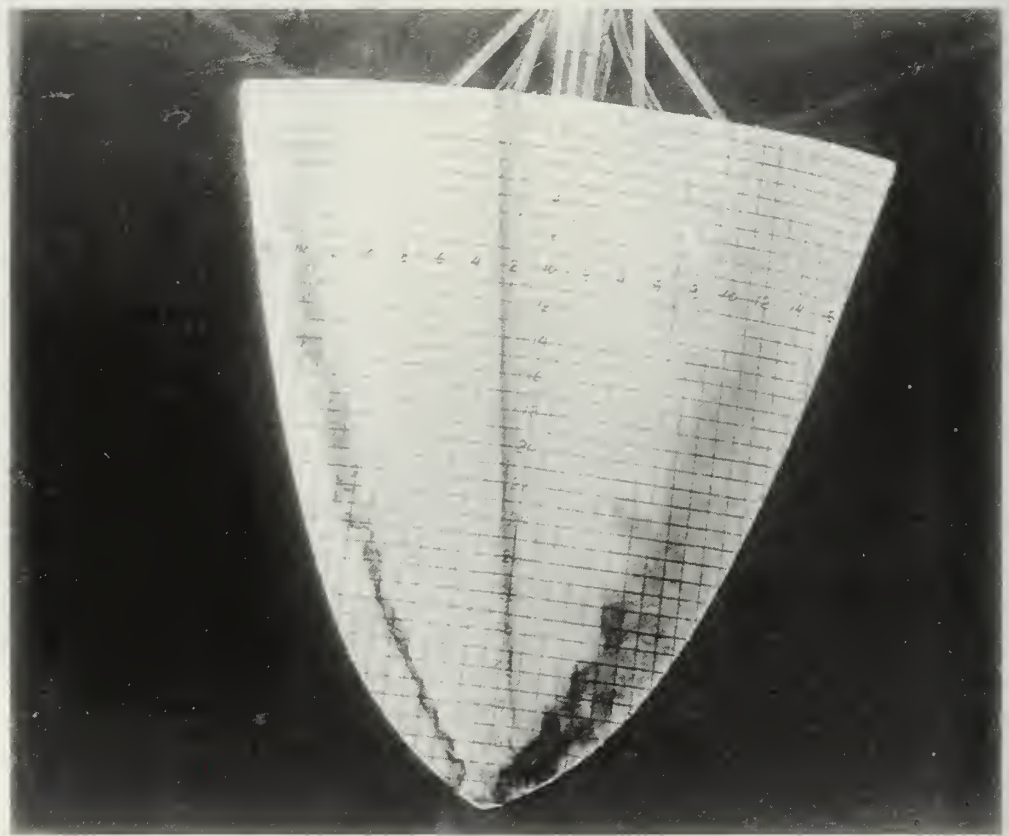
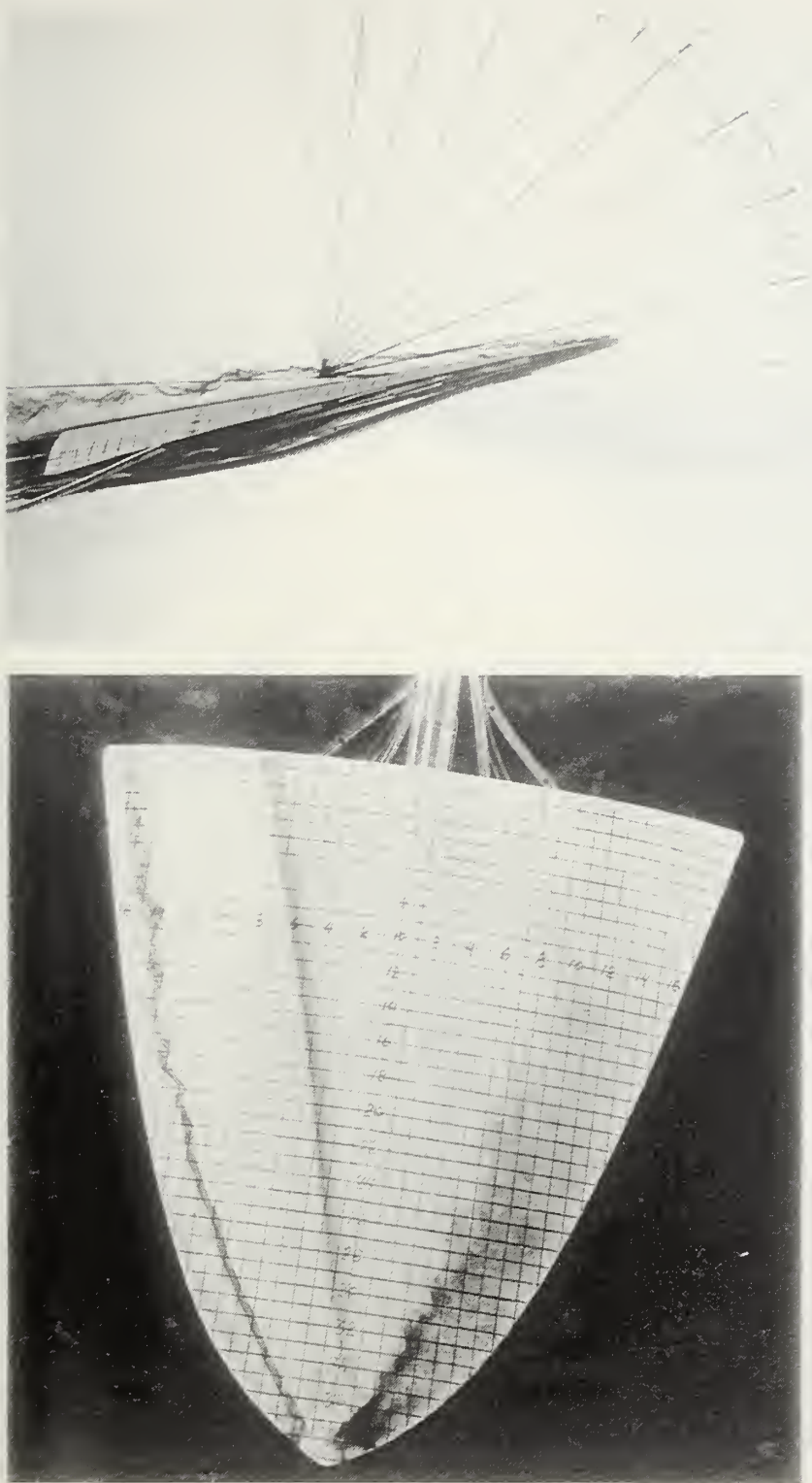


Figure 3.13 Sideslip Effects, Baseline Model, $\alpha=7^\circ$, $\beta=5^\circ$



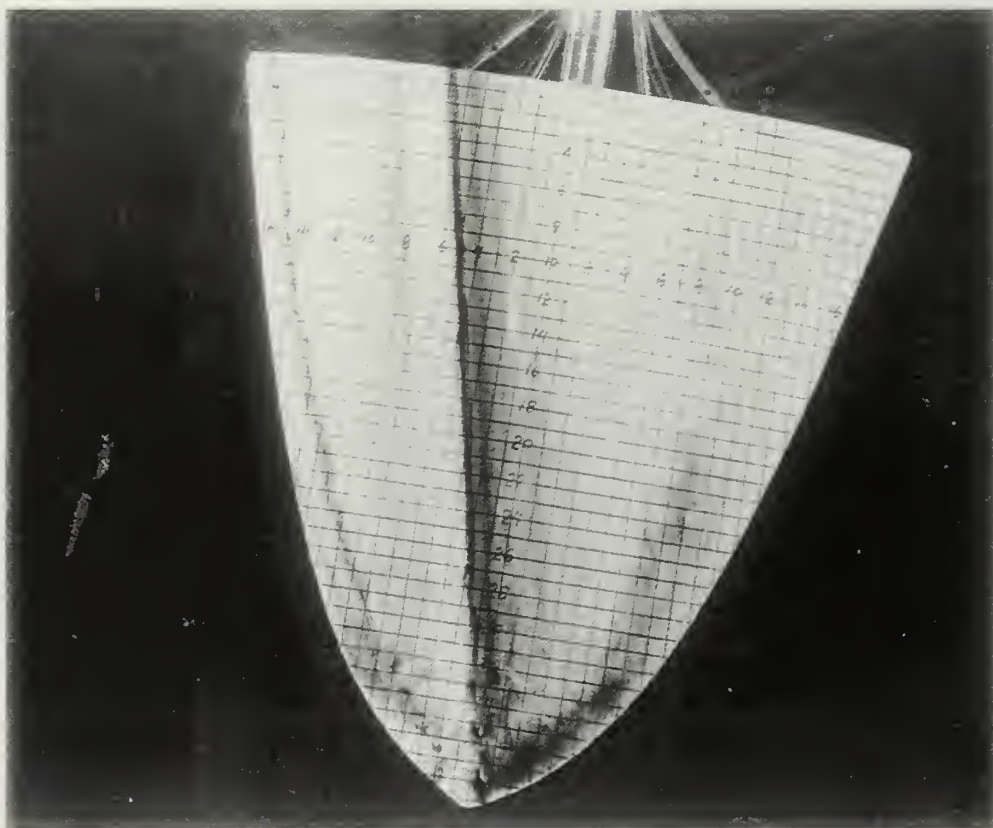


Figure 3.15 Sideslip Effects, Baseline Model, $\alpha=2^\circ$, $\beta=10^\circ$

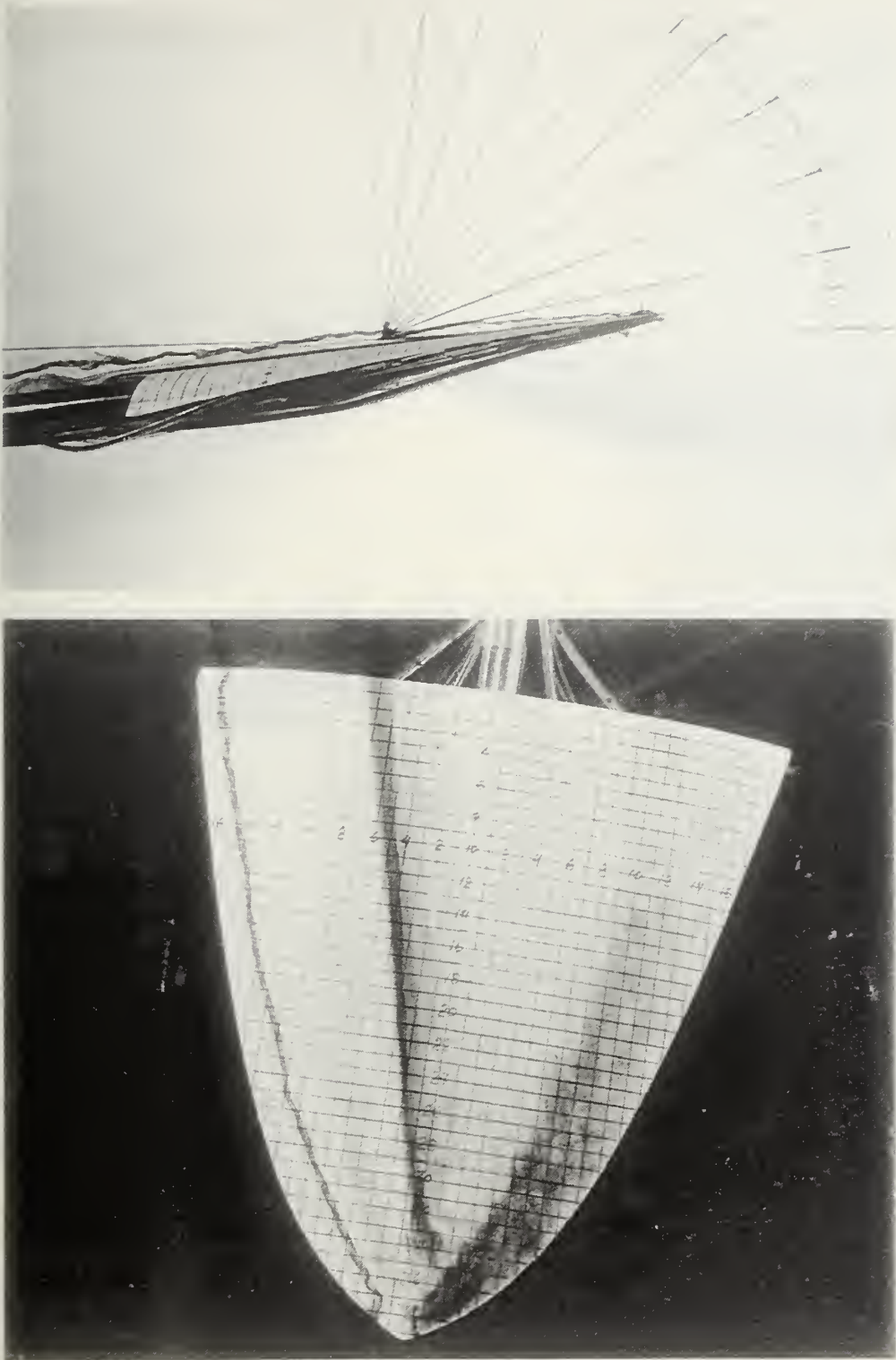


Figure 3.16 Sideslip Effects, Baseline Model, $\alpha=4^\circ$, $\beta=10^\circ$

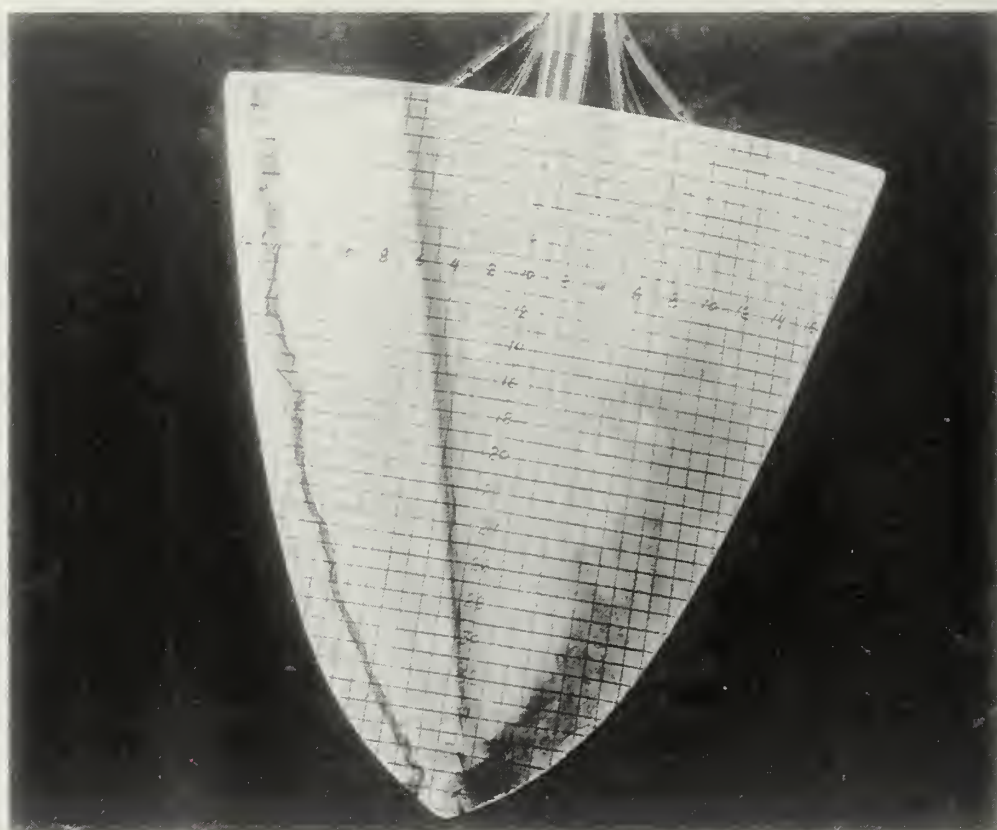


Figure 3.17 Sideslip Effects, Baseline Model, $\alpha=5^\circ$, $\beta=10^\circ$

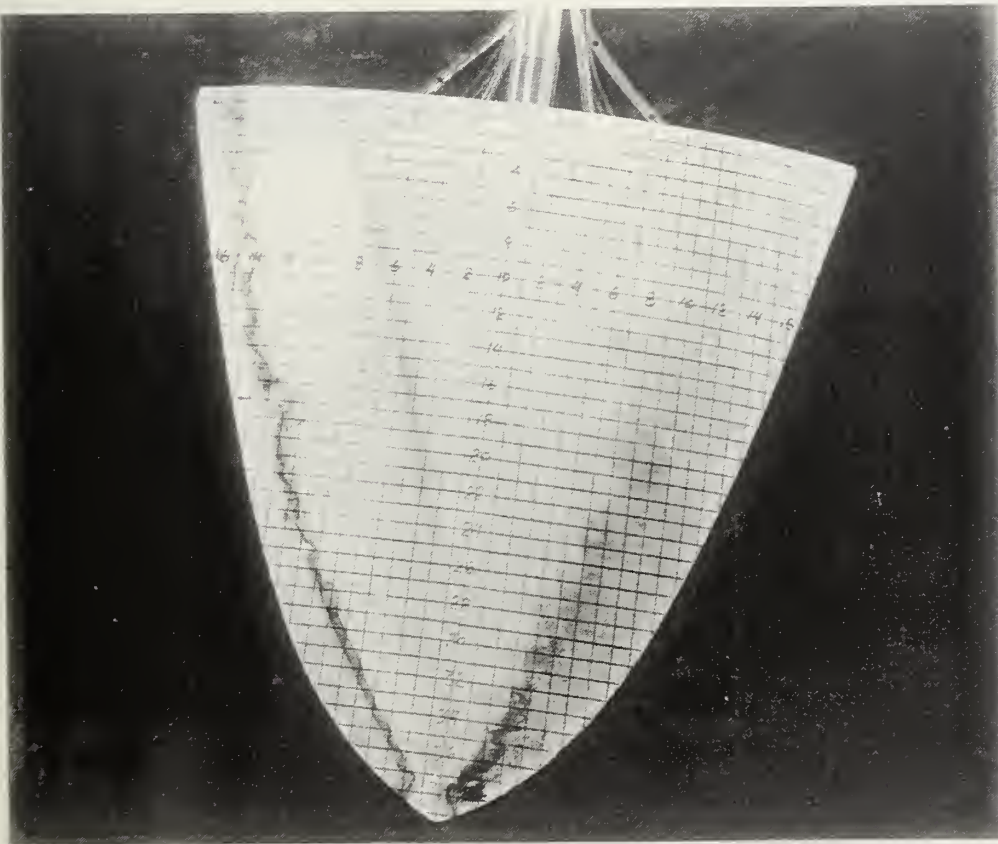


Figure 3.18 Sideslip Effects, Baseline Model, $\alpha=7^\circ$, $\beta=10^\circ$

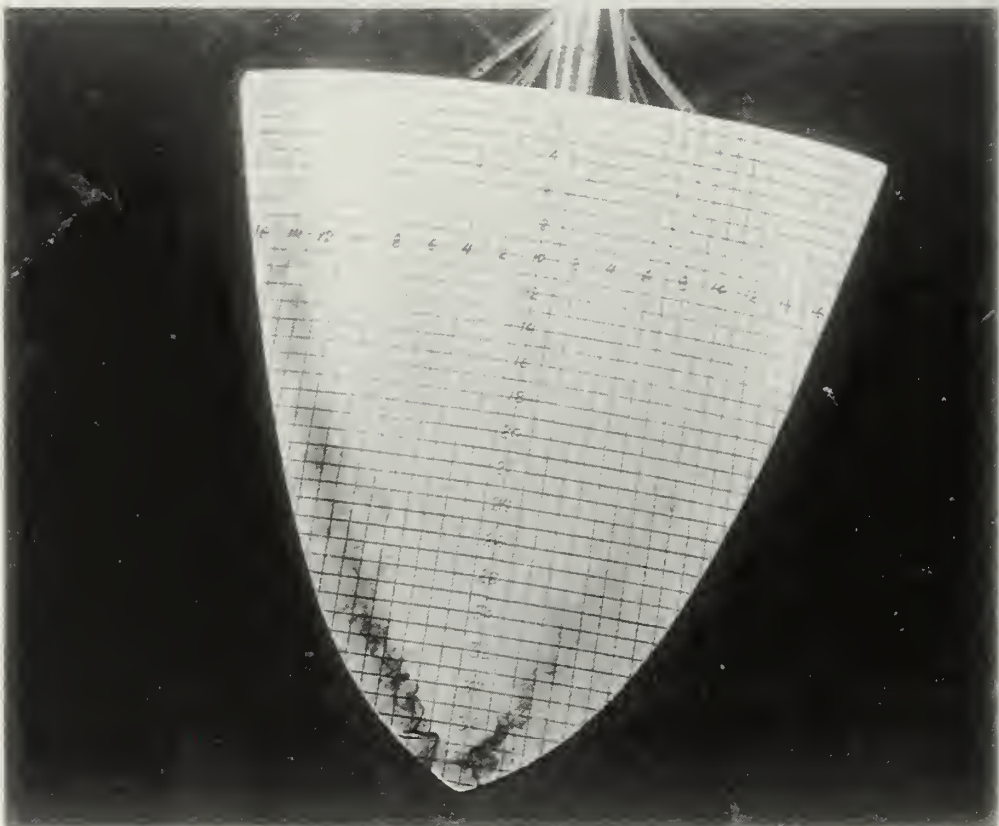


Figure 3.19 Sideslip Effects, Baseline Model, $\alpha=9^\circ$, $\beta=10^\circ$

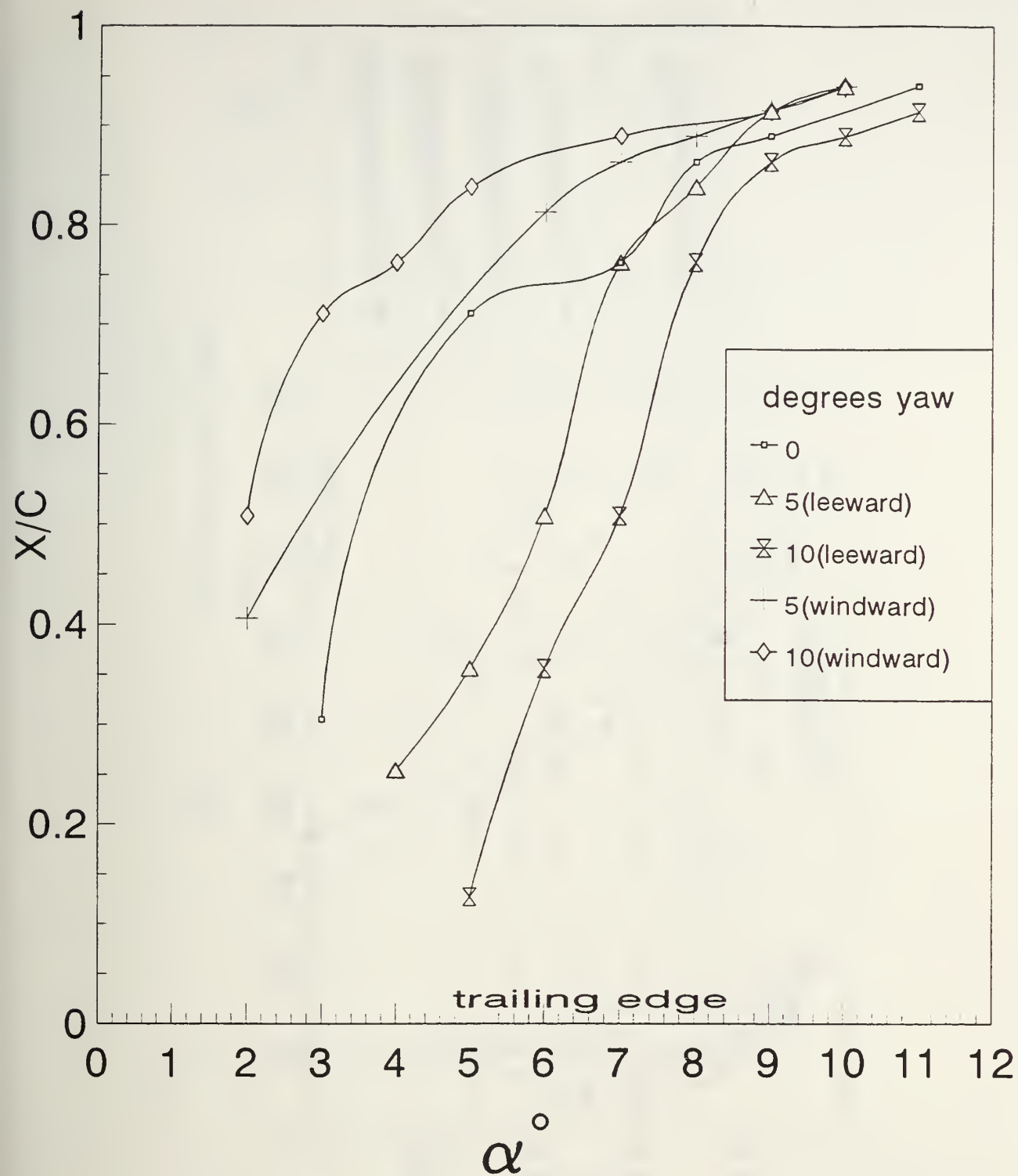


Figure 3.20a Baseline Model, Vortex Burst Asymmetry

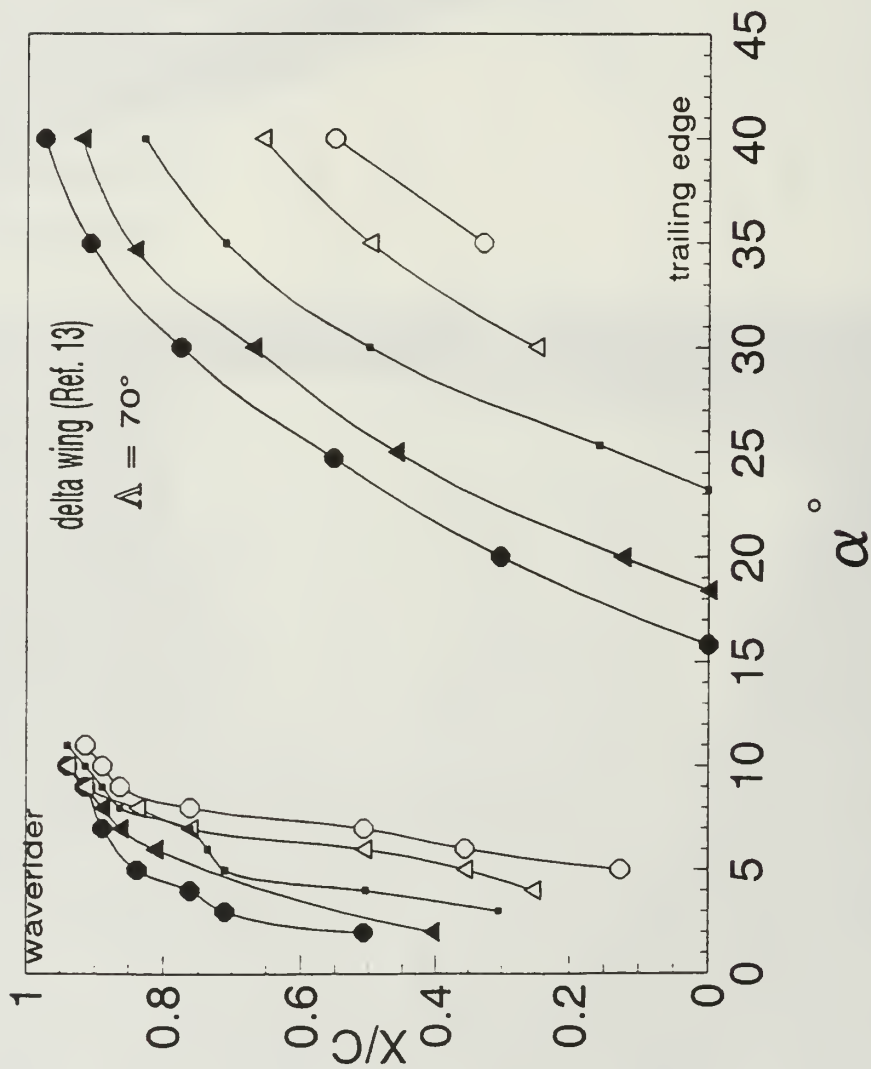


Figure 3.20b Baseline Model Compared to 70° Delta Wing, Vortex Burst Asymmetry

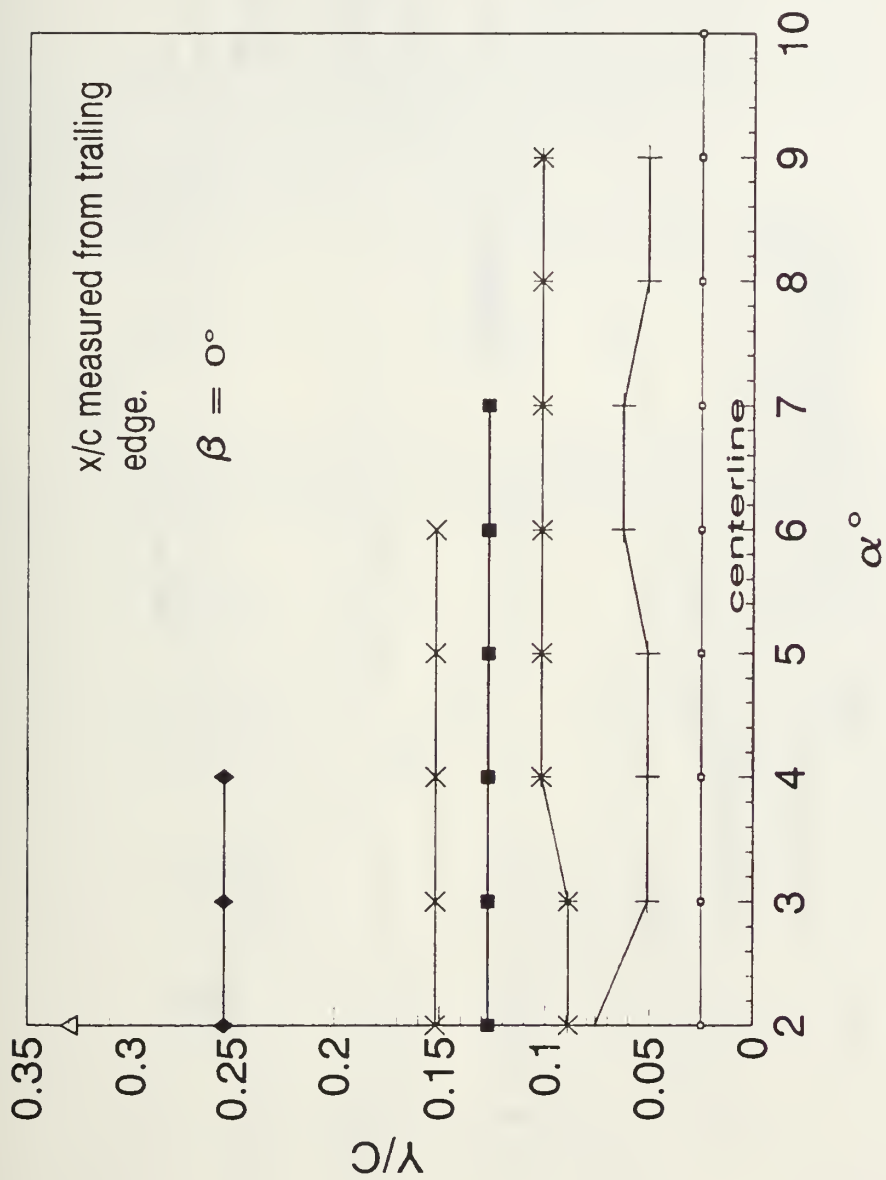


Figure 3.21 Baseline Model, Angle of Attack Effects on Vortex Core Lateral Position, $\beta=0^\circ$

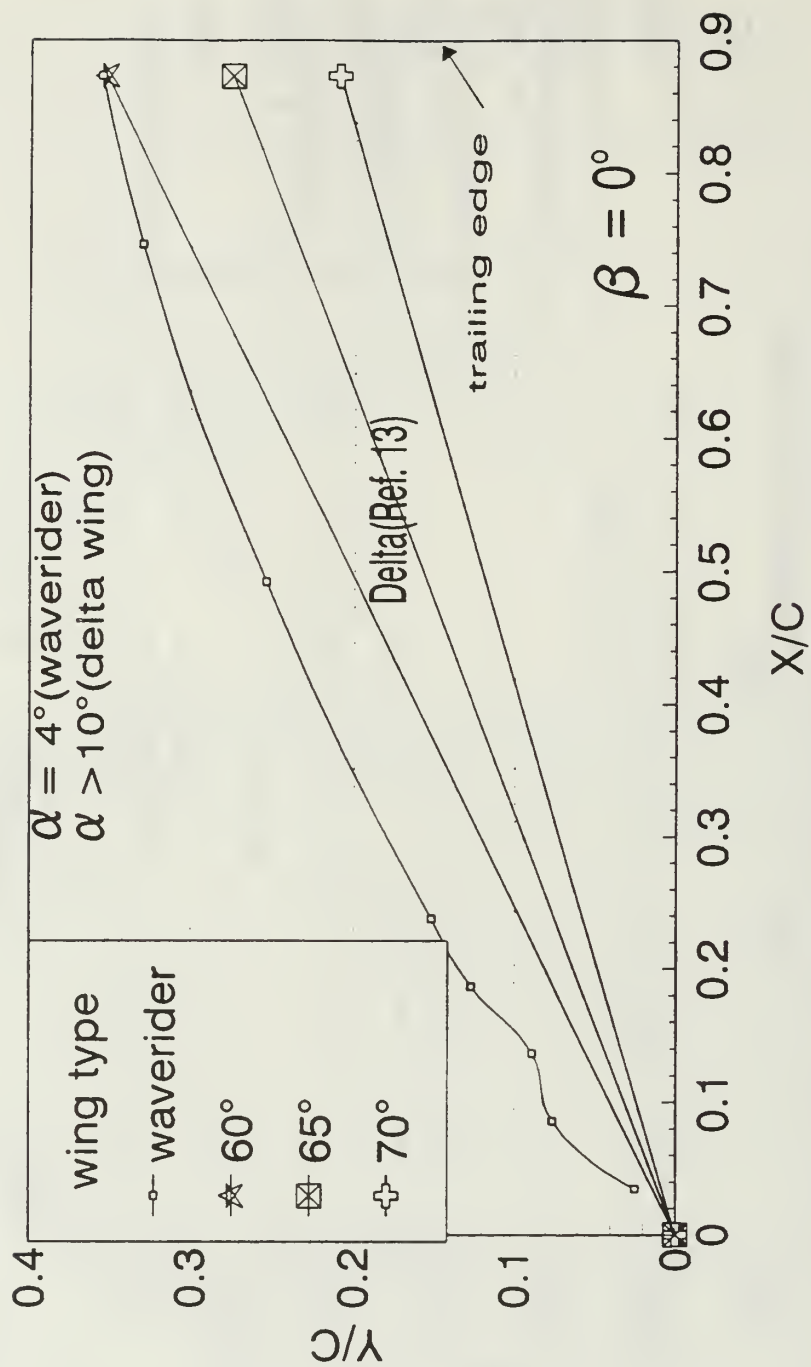


Figure 3.22 Baseline Model Compared to Delta Wing, Vortex Core Lateral Position, $\beta=0^\circ$

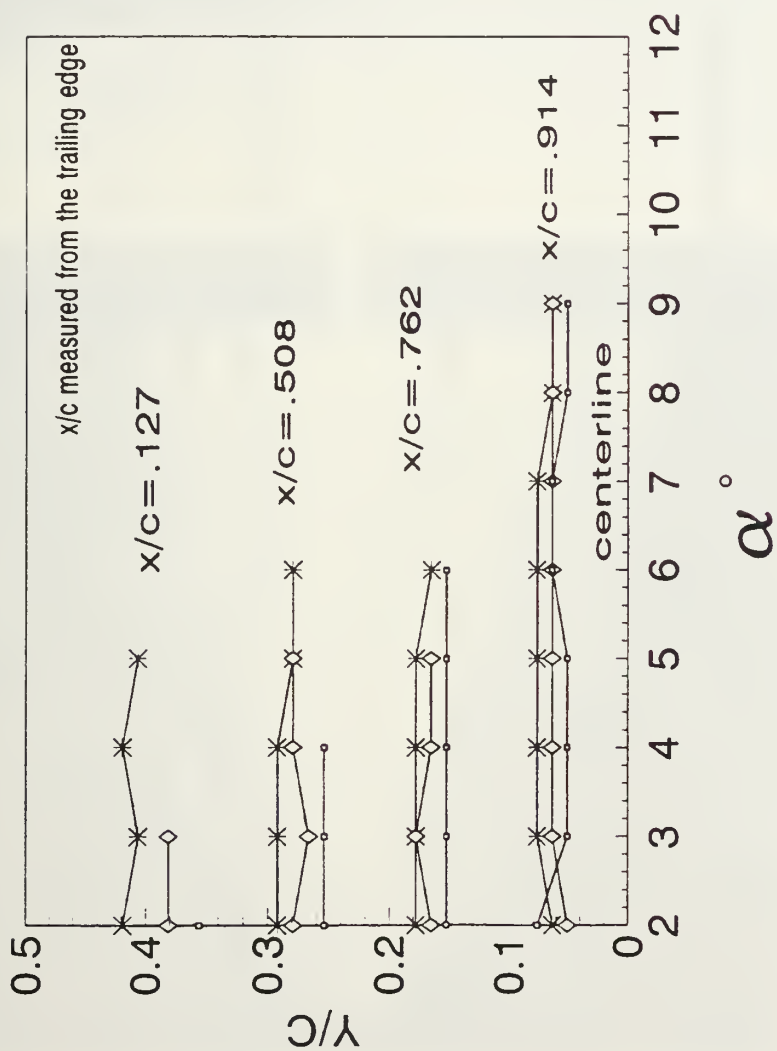


Figure 3.23 Baseline Model, Sideslip Effects on Vortex Core Lateral Position (leeward Side)

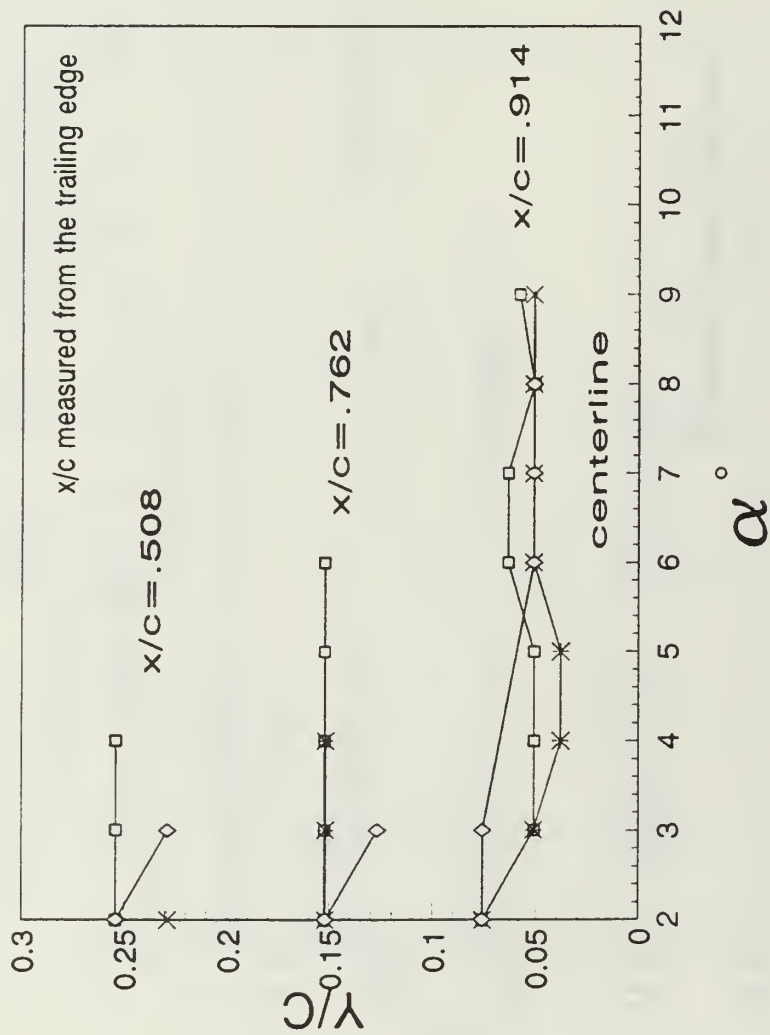


Figure 3.24 Baseline Model, Sideslip Effects on Vortex Core Lateral Position (Windward Side)

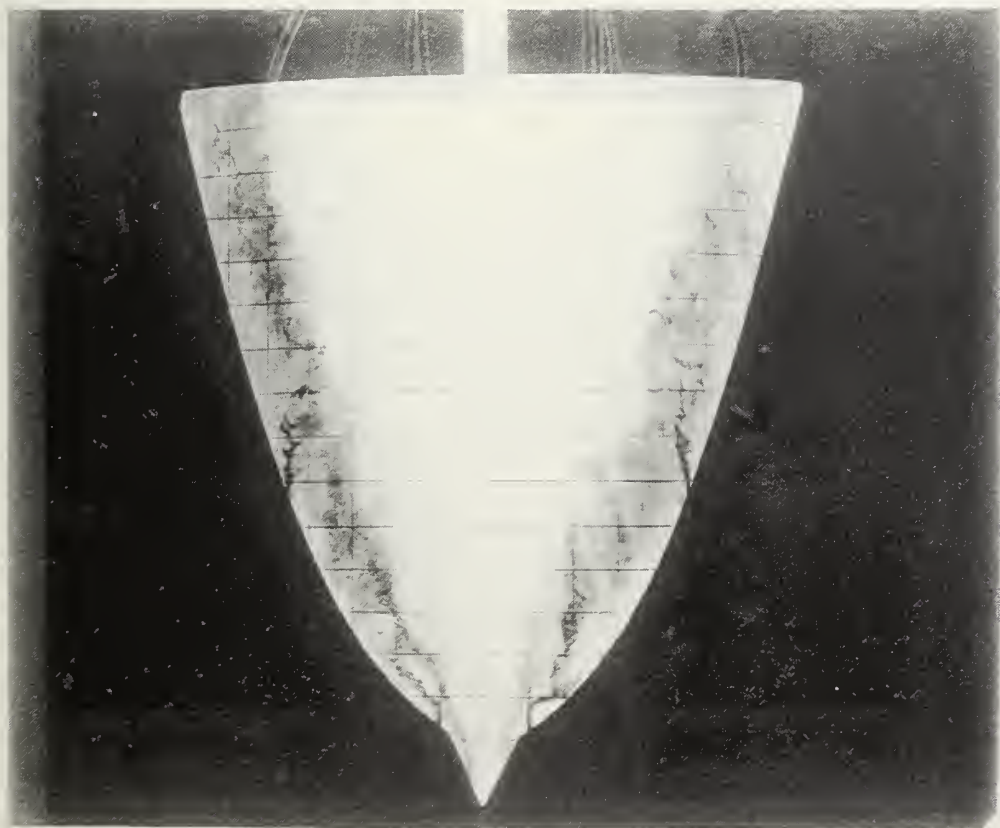
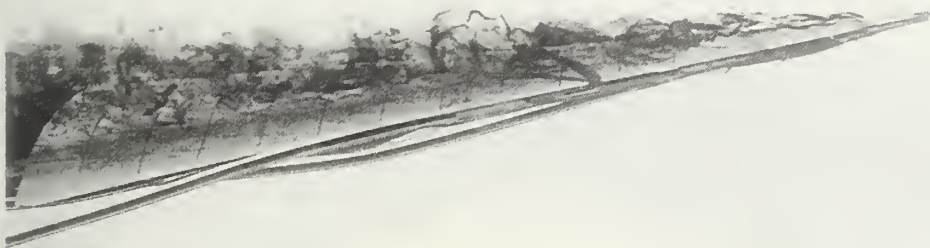


Figure 3.25 Entrainment, Modification One, $\alpha=4^\circ$, $\beta=0^\circ$

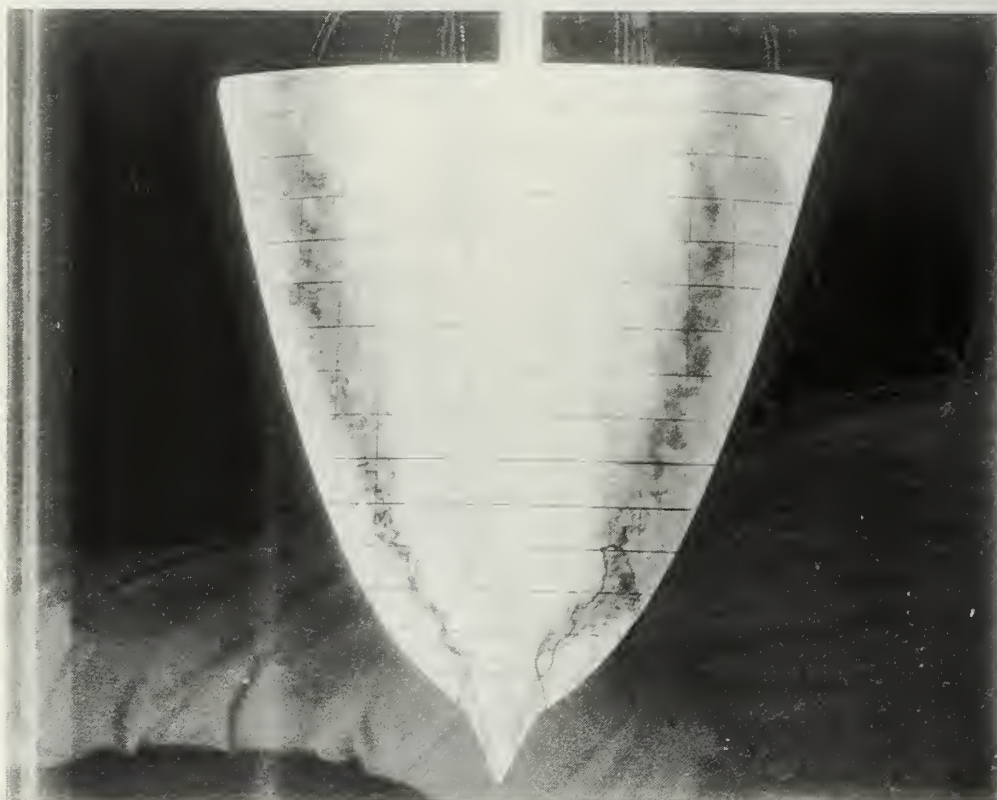
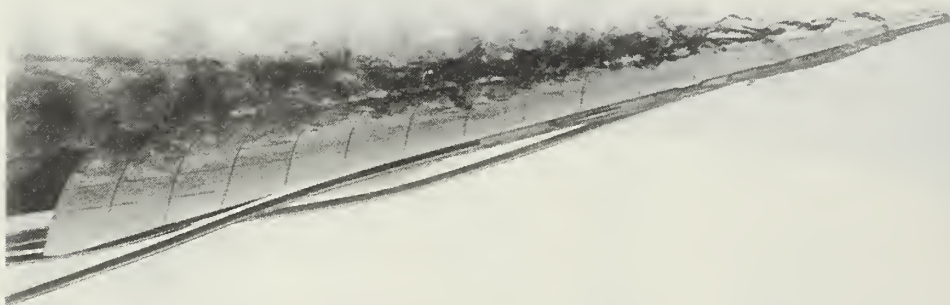


Figure 3.26 Entrainment, Modification One, $\alpha=6^\circ$, $\beta=0^\circ$

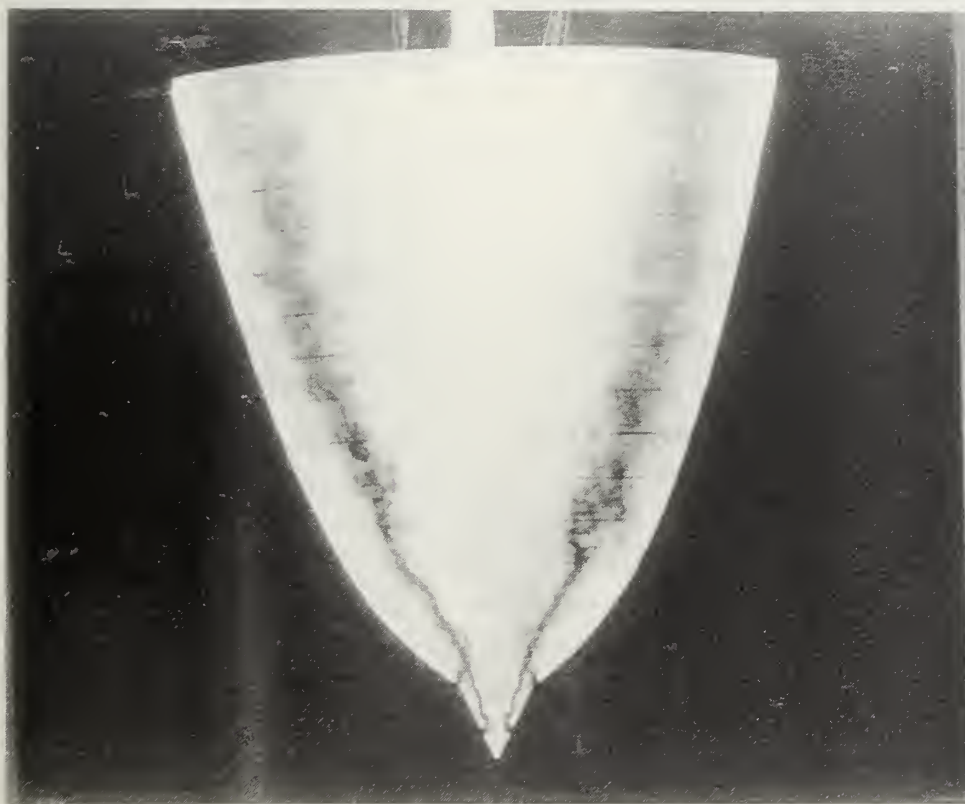
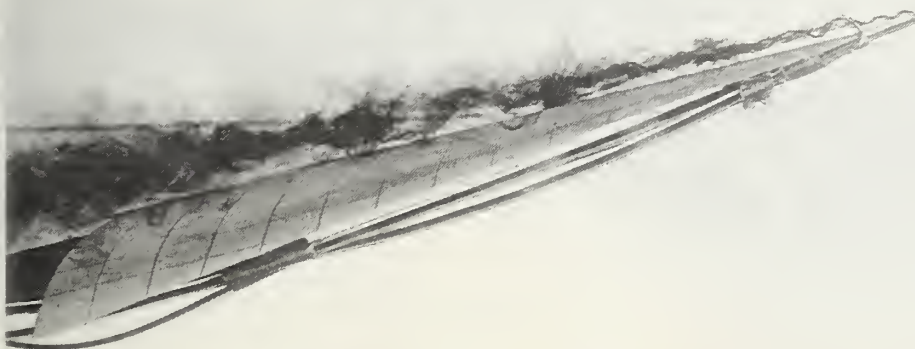


Figure 3.27 Entrainment, Modification One, $\alpha=10^\circ$, $\beta=0^\circ$

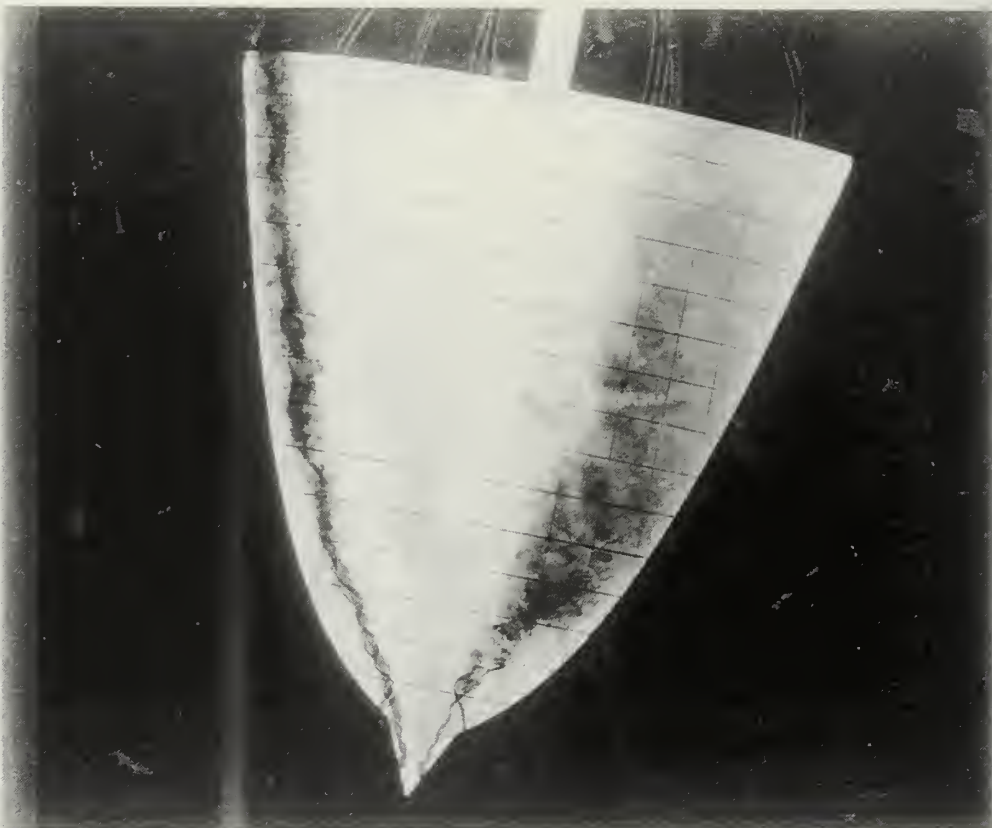
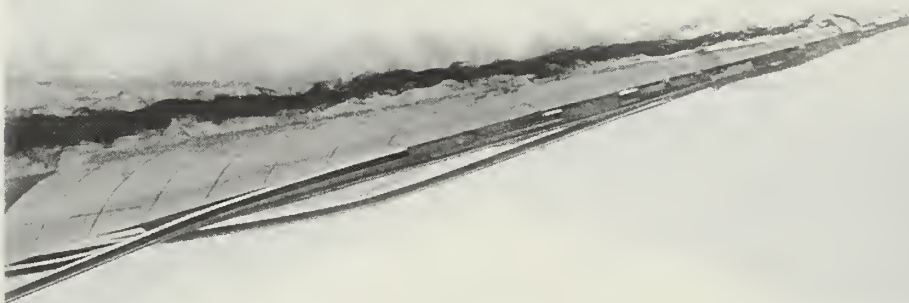


Figure 3.28 Entrainment, Modification One, $\alpha=8^\circ$, $\beta=10^\circ$

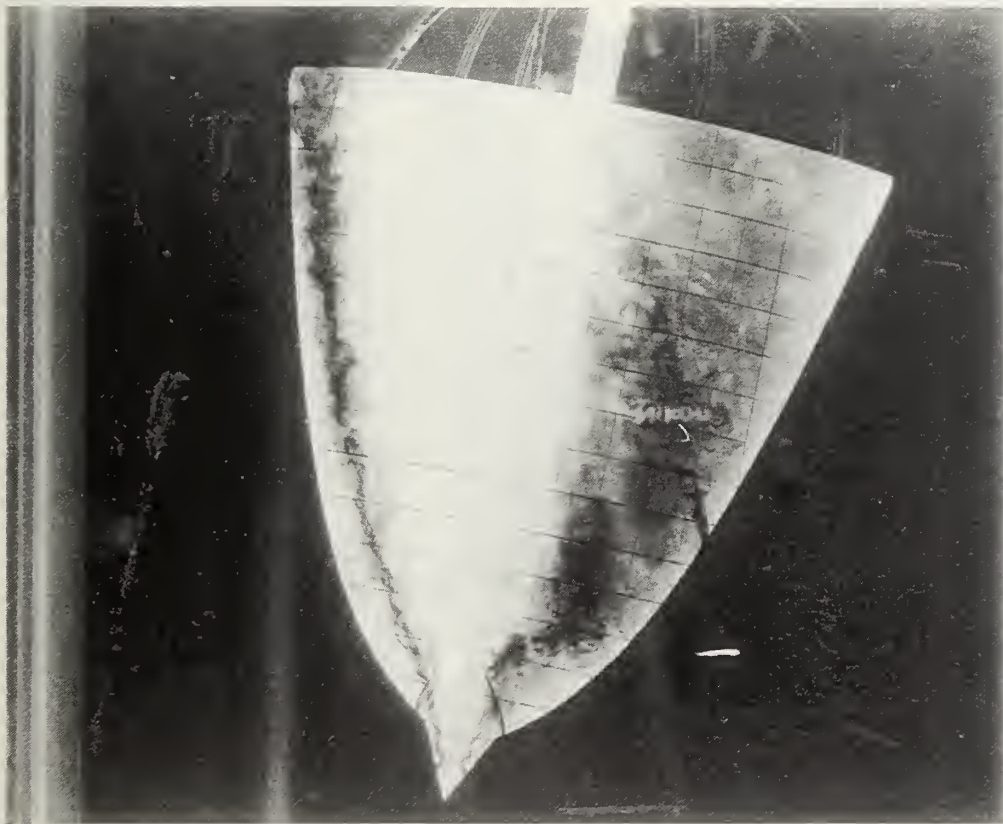


Figure 3.29 Entrainment, Modification One, $\alpha=12^\circ$, $\beta=10^\circ$

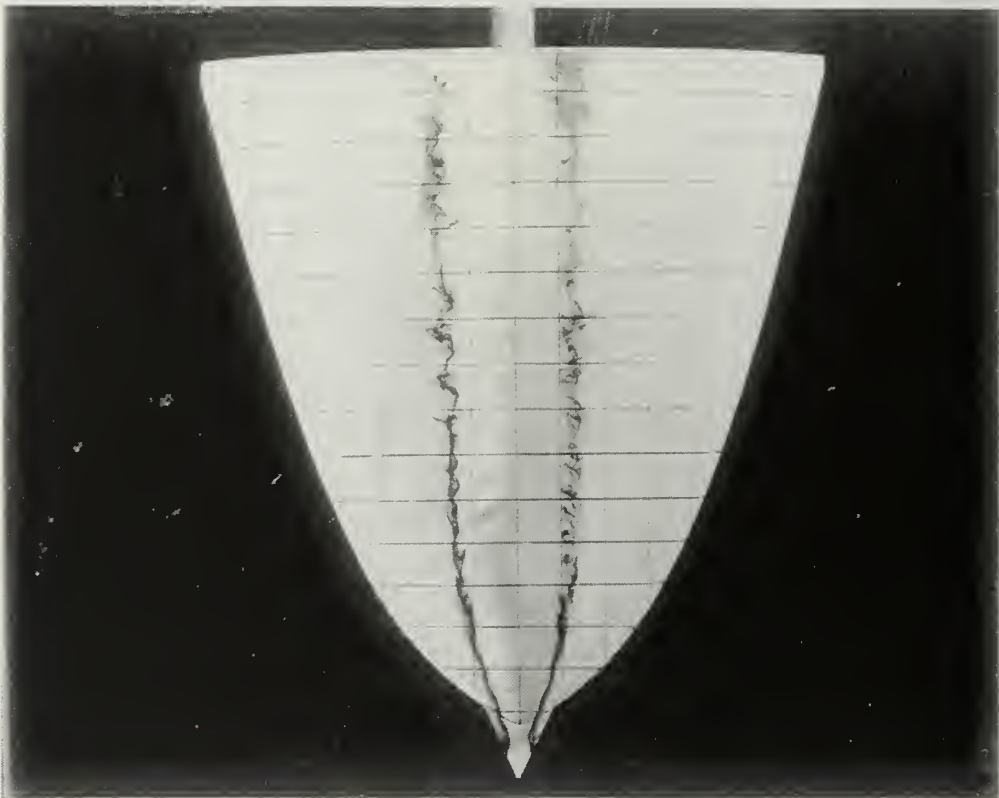
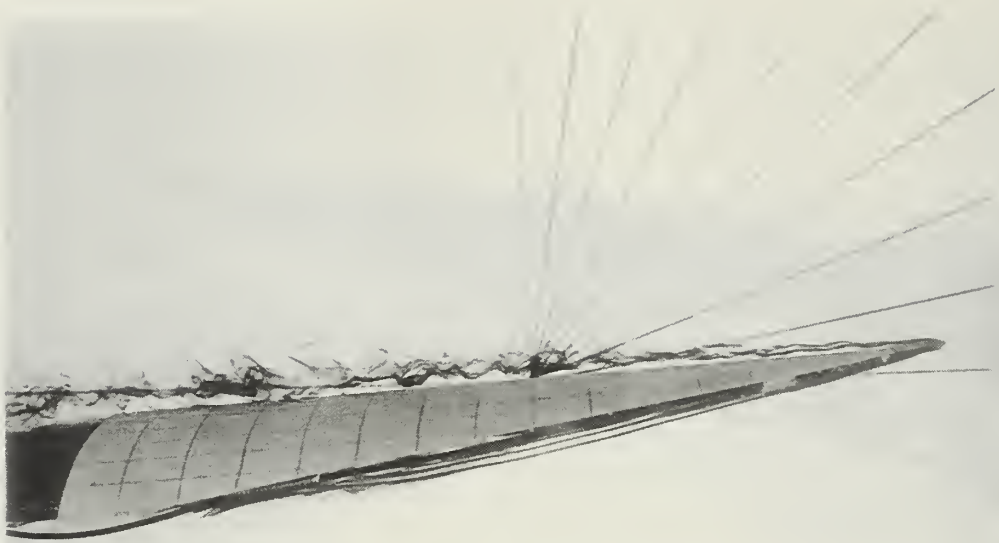


Figure 3.30 Angle of Attack Effects, Modification One, $\alpha=2^\circ$, $\beta=0^\circ$

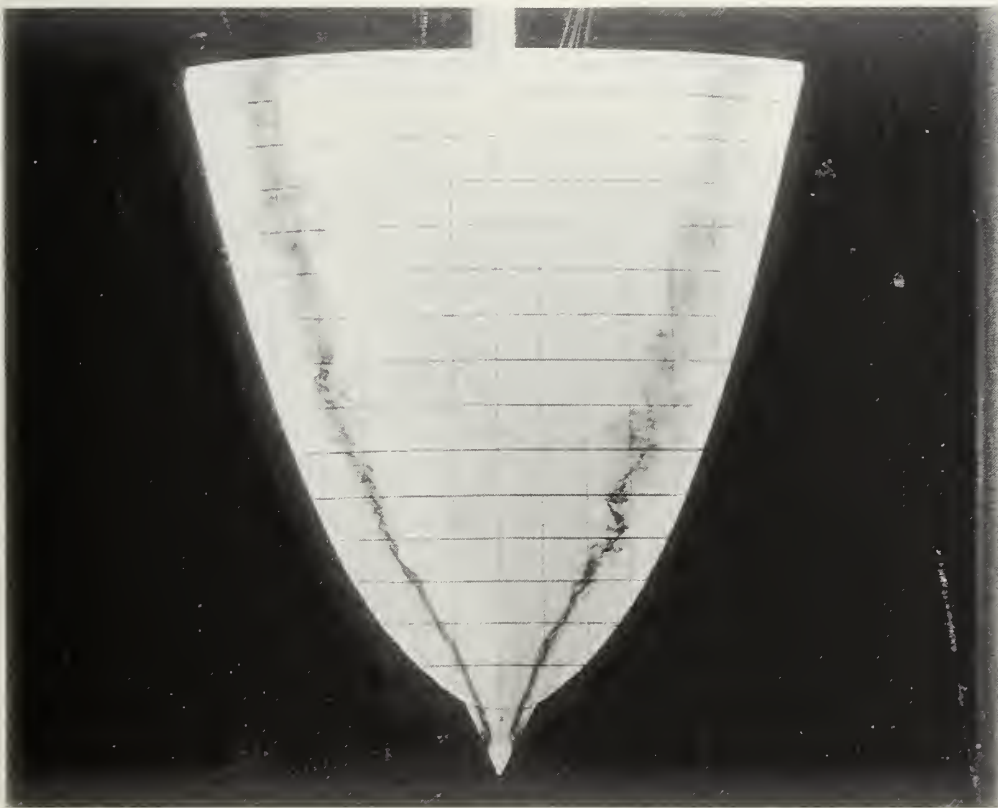


Figure 3.31 Angle of Attack Effects, Modification One, $\alpha=6^\circ$, $\beta=0^\circ$

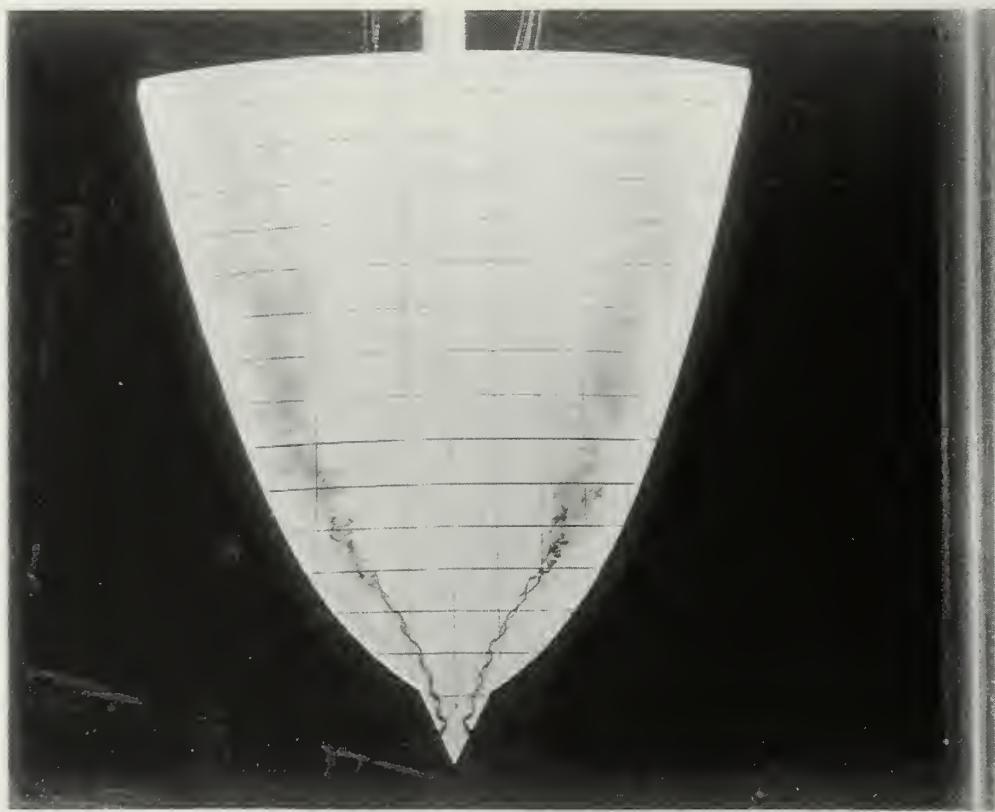
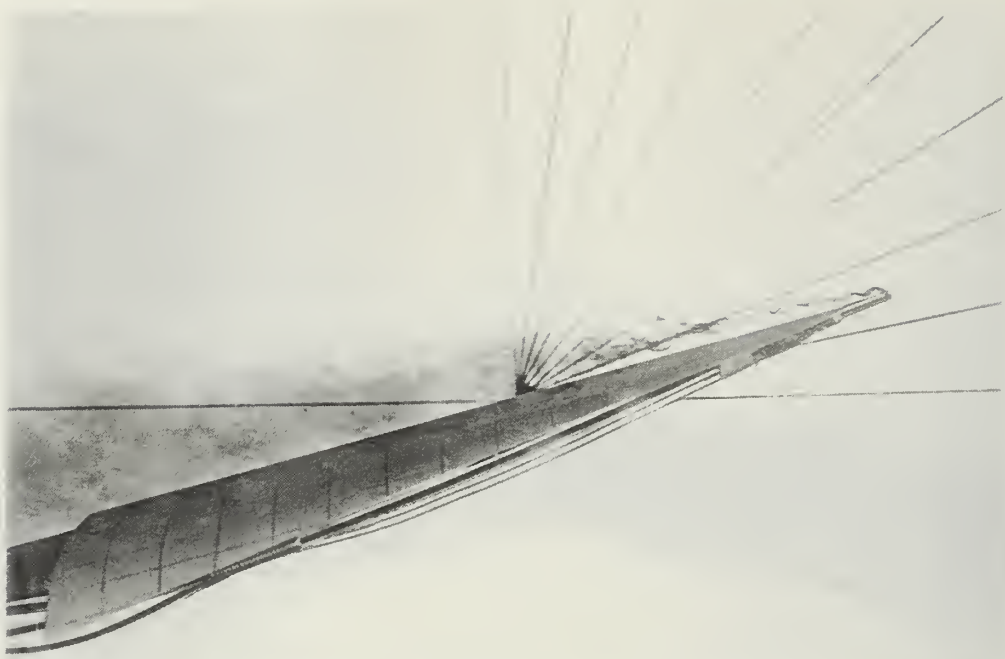


Figure 3.32 Angle of Attack Effects, Modification One, $\alpha=12^\circ$, $\beta=0^\circ$



Figure 3.33 Angle of Attack Effects, Modification One, $\alpha=16^\circ$, $\beta=0^\circ$

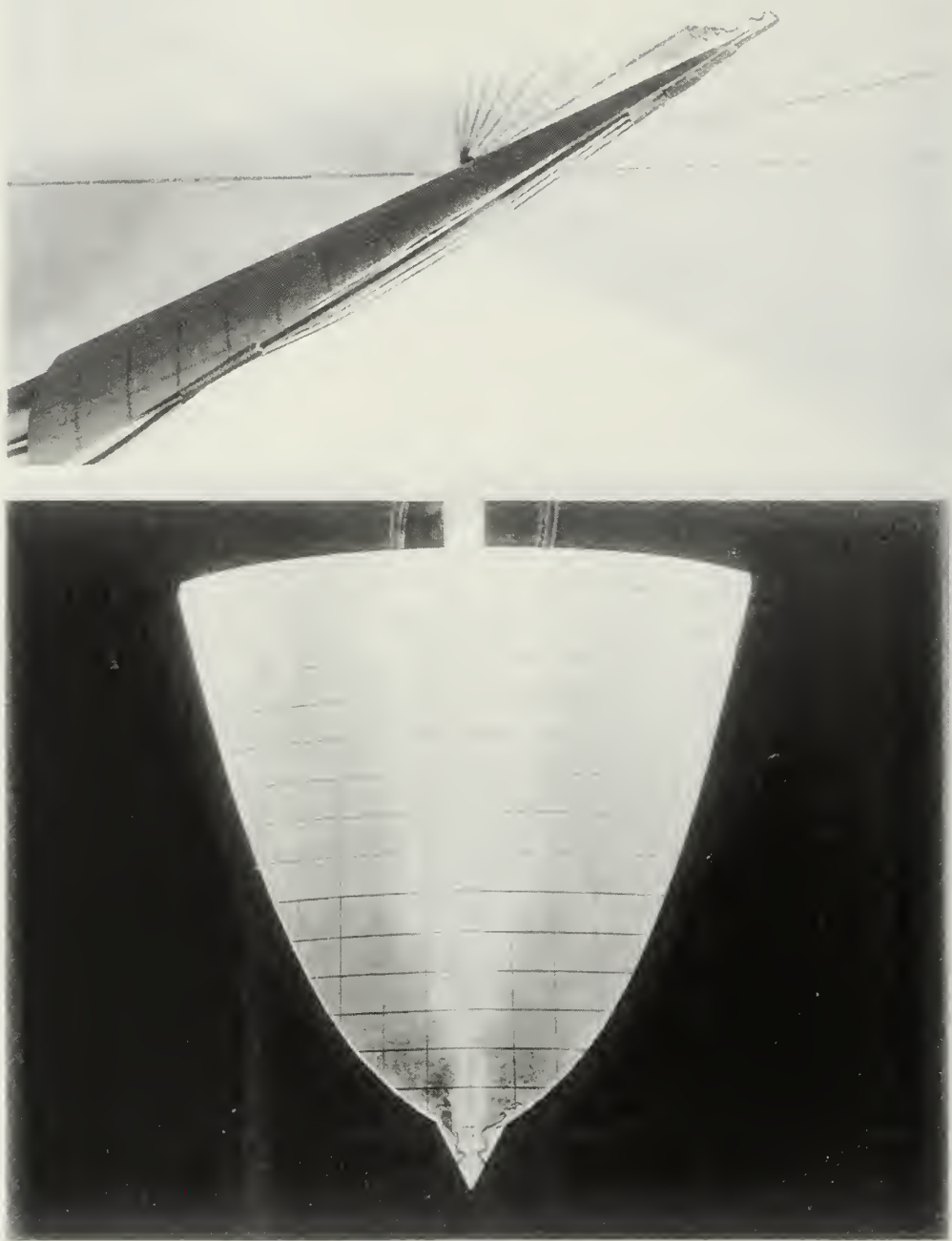


Figure 3.34 Angle of Attack Effects, Modification One, $\alpha=20^\circ$, $\beta=0^\circ$

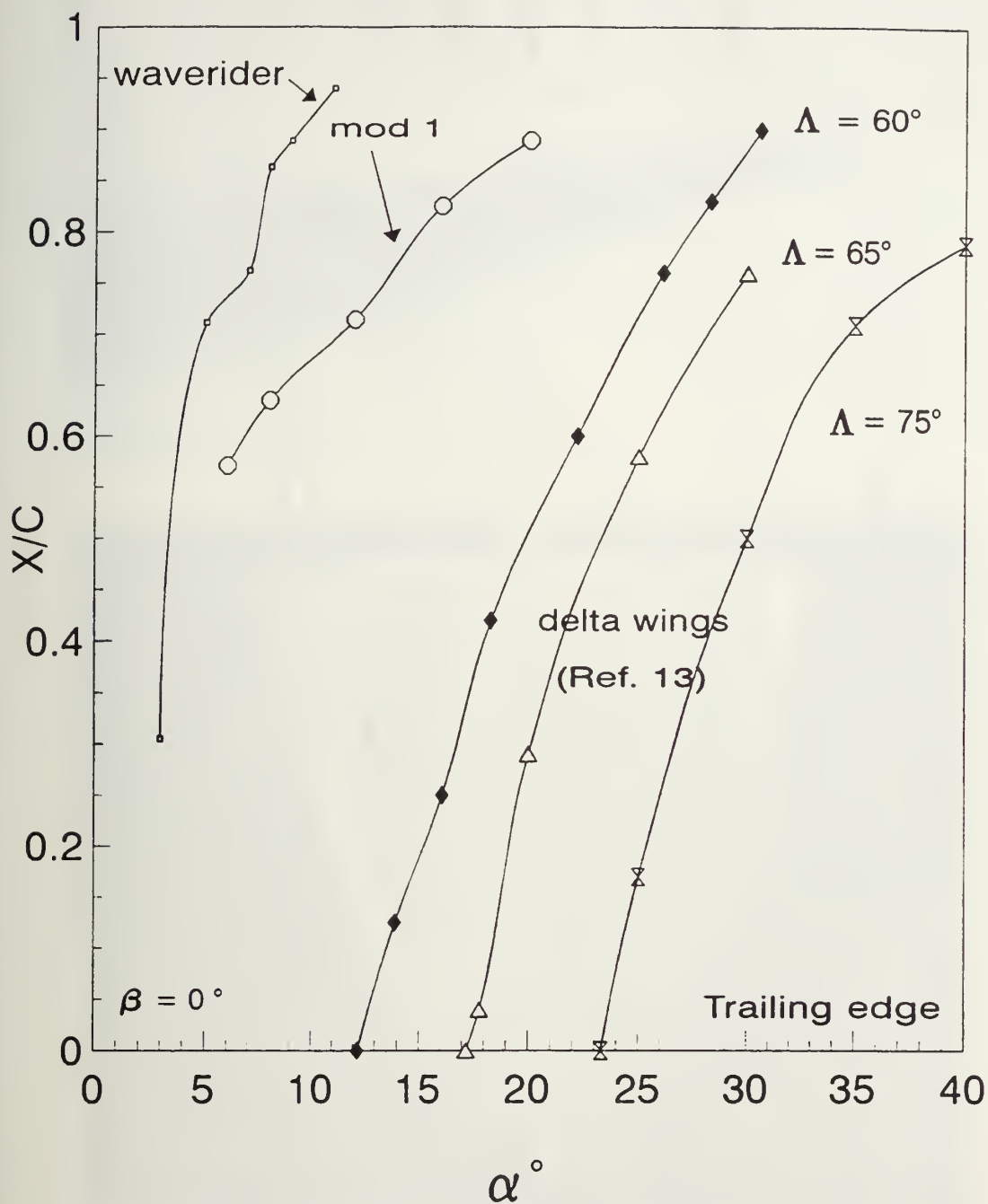


Figure 3.35 Vortex Burst Location as a Function of Angle of Attack, Baseline Model Compared to Modification One and Delta Wing, $\beta=0^\circ$

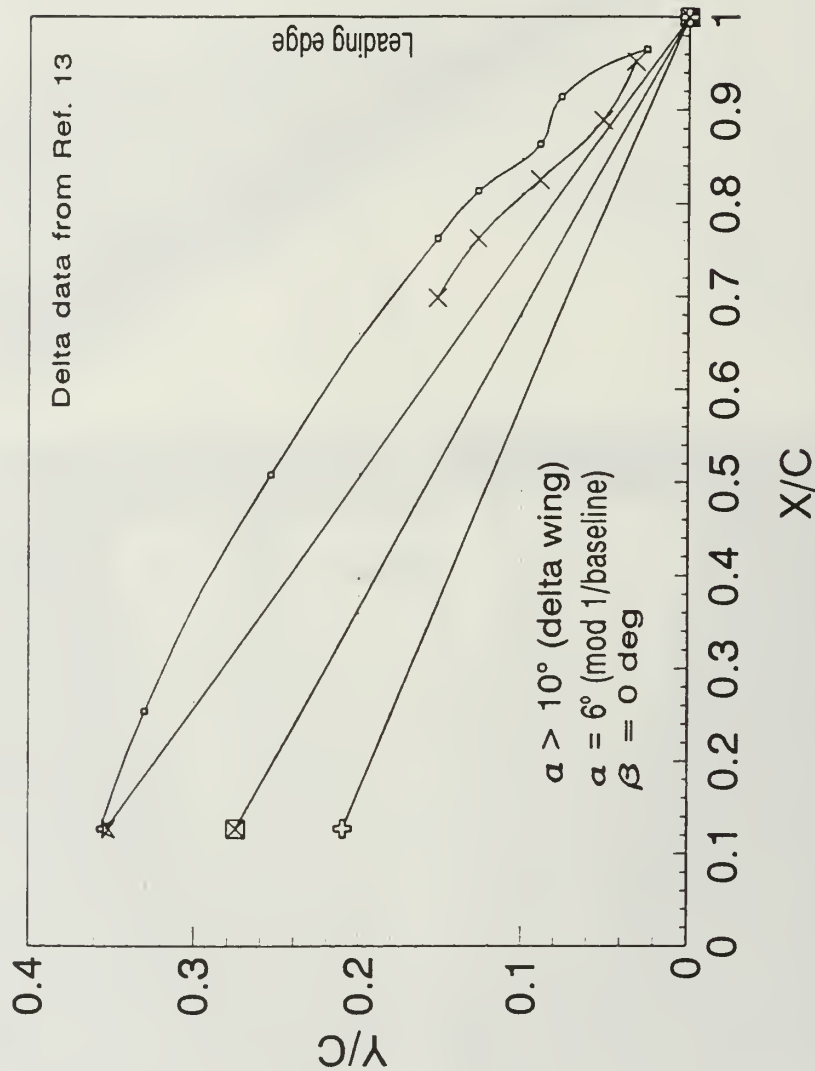


Figure 3.36 Baseline Model Compared to Modification One and Delta Wing, Vortex Core Lateral Position, $\beta=0^\circ$

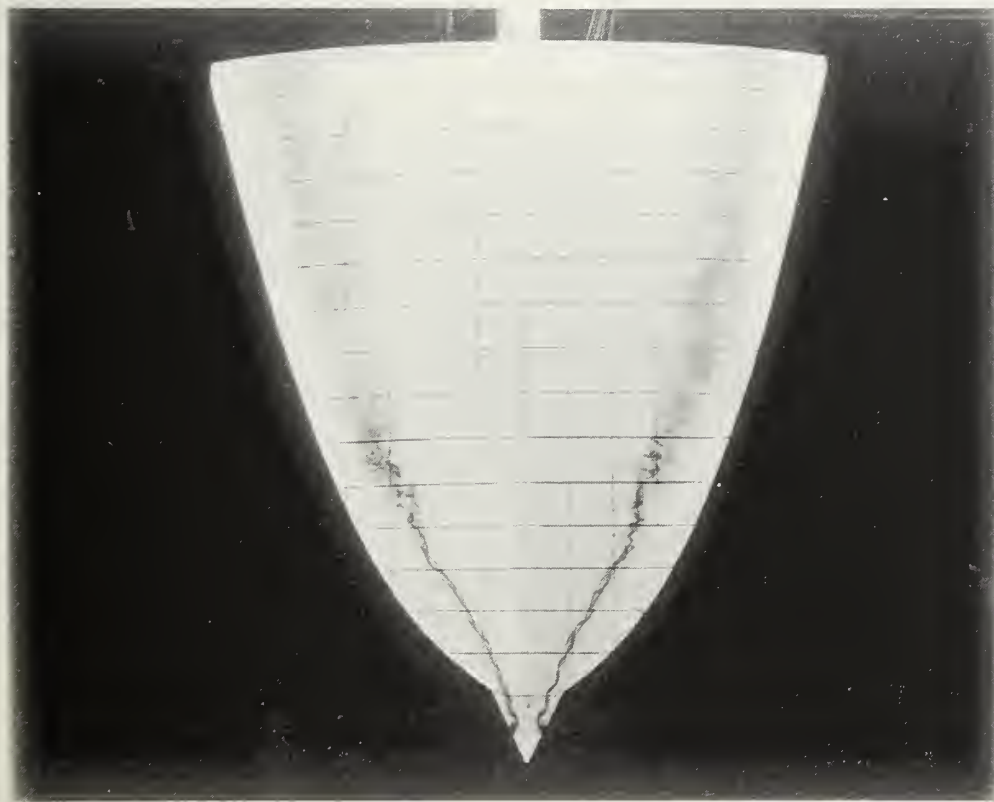


Figure 3.37 Sideslip Effects, Modification One, $\alpha=8^\circ$, $\beta=0^\circ$

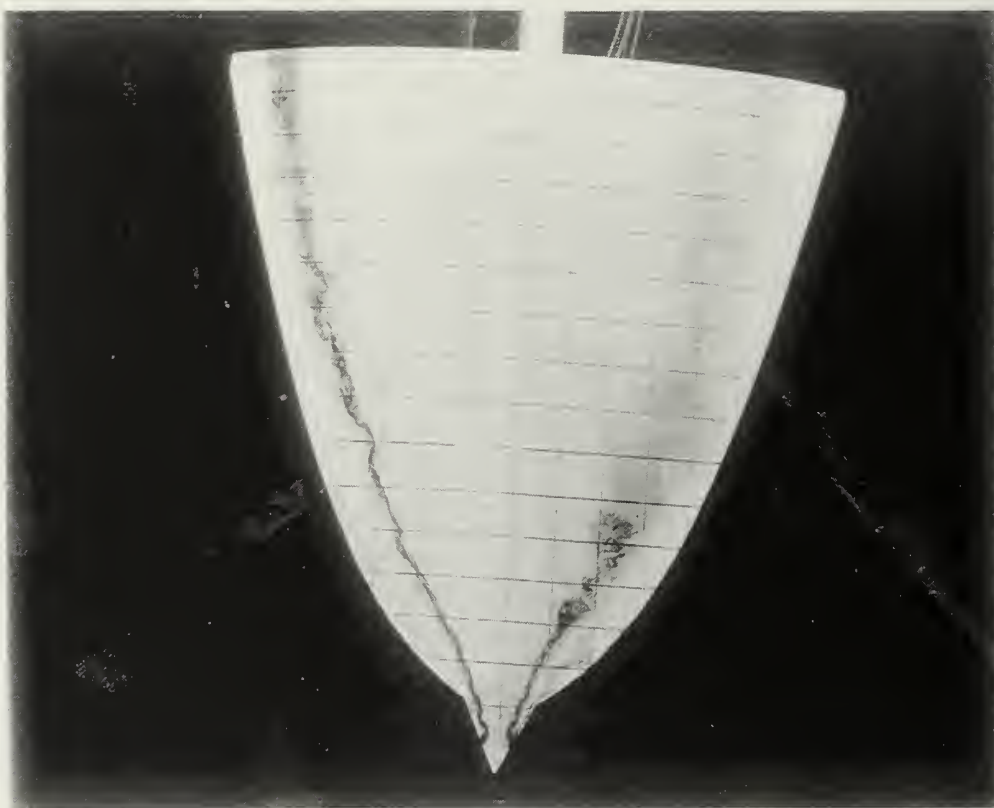
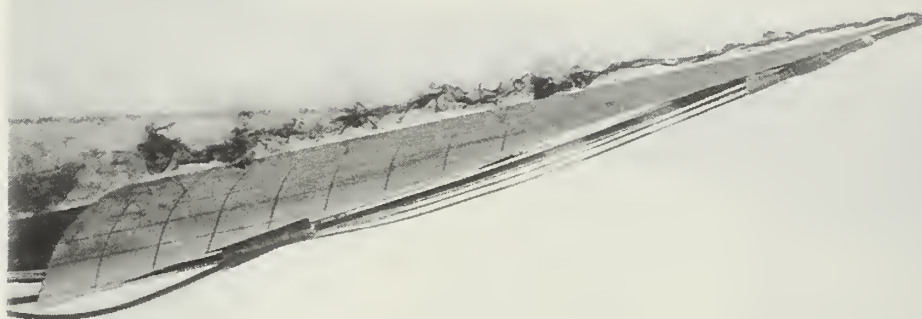


Figure 3.38 Sideslip Effects, Modification One, $\alpha=8^\circ$, $\beta=5^\circ$

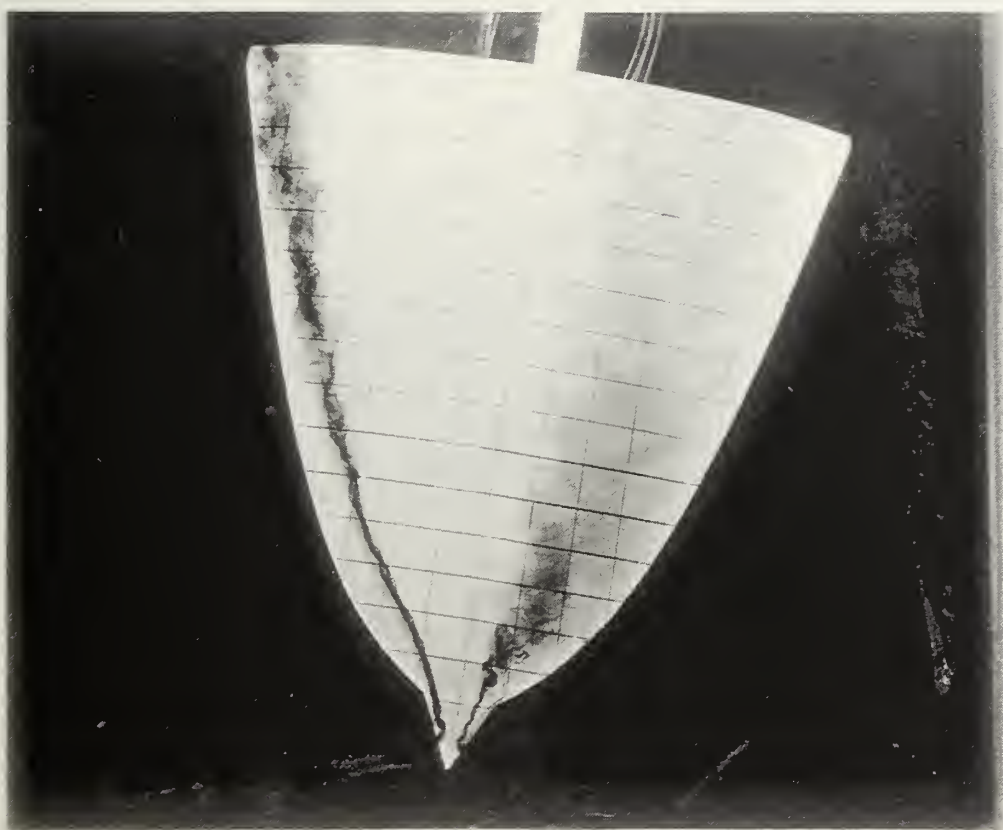


Figure 3.39 Sideslip Effects, Modification One, $\alpha=8^\circ$, $\beta=10^\circ$

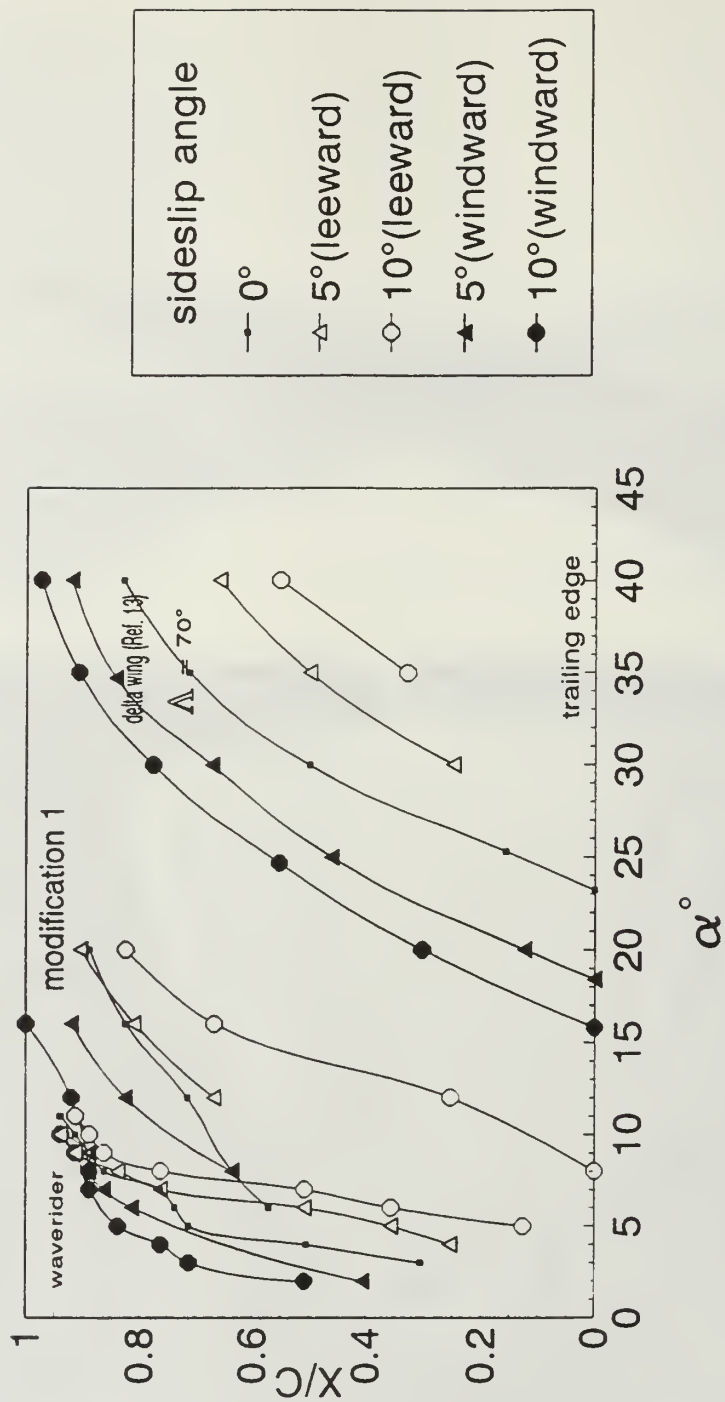


Figure 3.40 Modification One, Vortex Burst Asymmetry

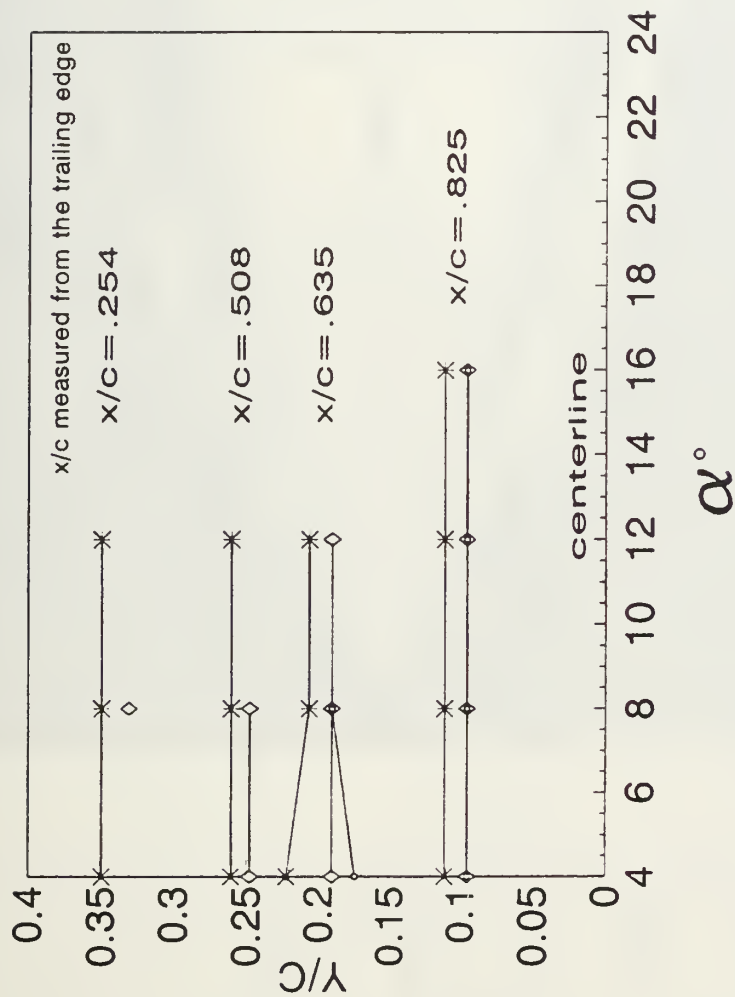


Figure 3.41 Modification One, Sideslip Effects on Vortex Core Lateral Position (leeward Side)

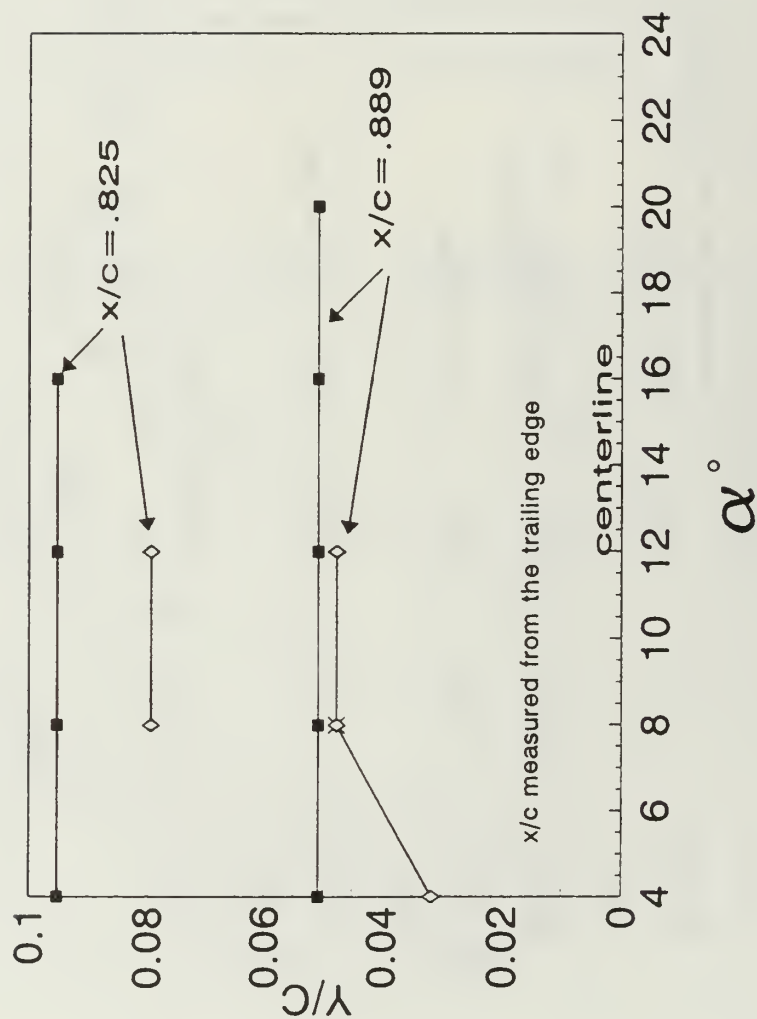


Figure 3.42 Modification One, Sideslip Effects on Vortex Core Lateral Position (Windward Side)

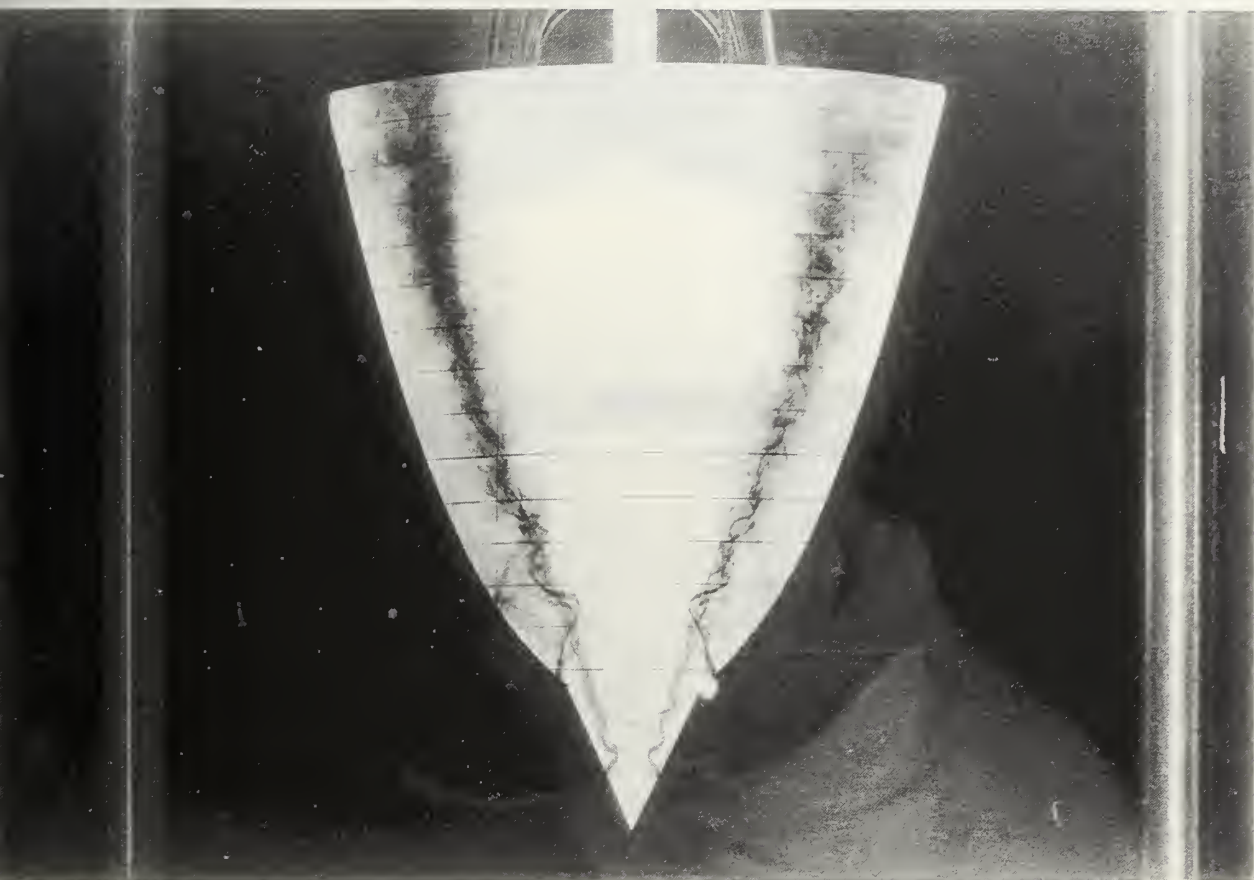


Figure 3.43 Modification Two, Entrainment, Angle of Attack Effects, $\alpha=4^\circ$,
 $\beta=0^\circ$

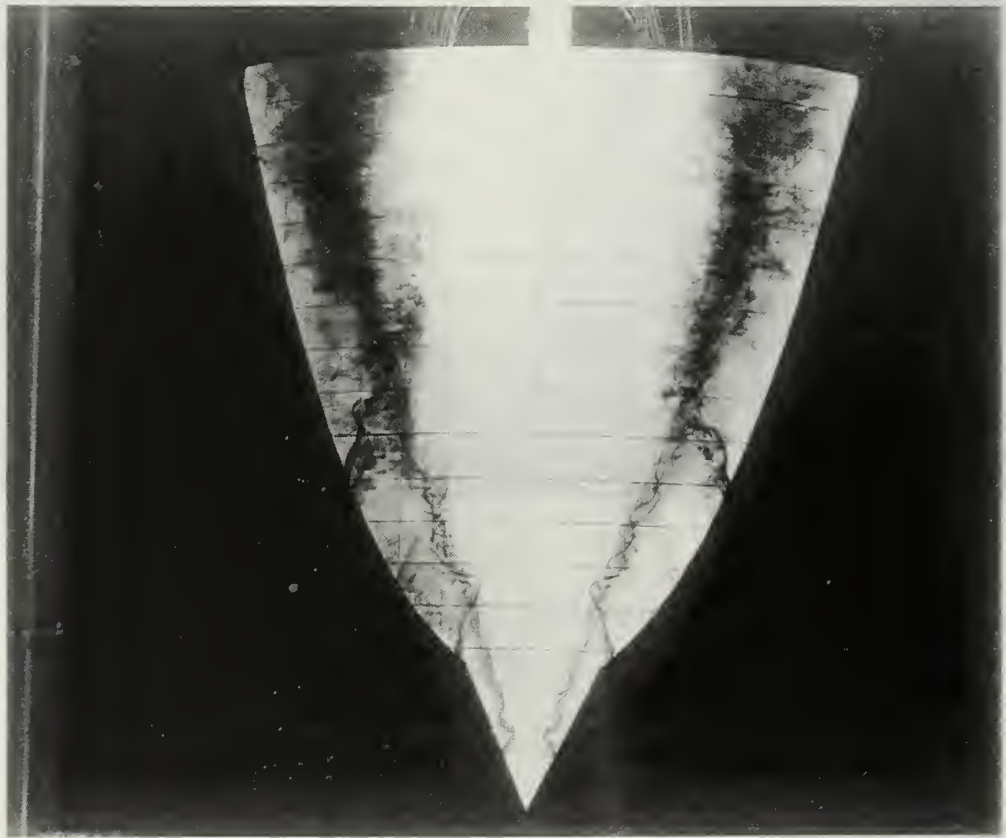
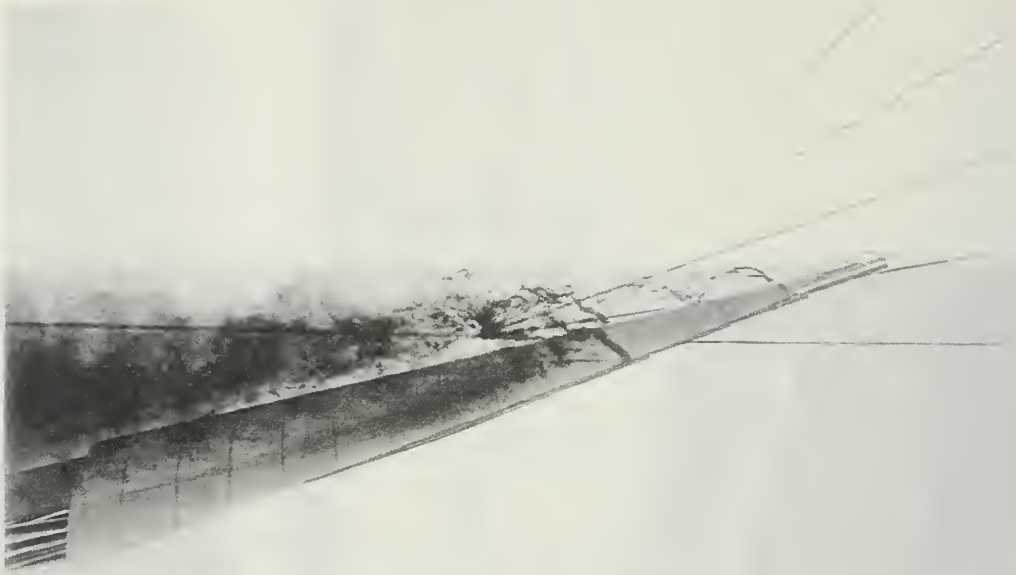


Figure 3.44 Modification Two, Entrainment, Angle of Attack Effects, $\alpha=12^\circ$,
 $\beta=0^\circ$

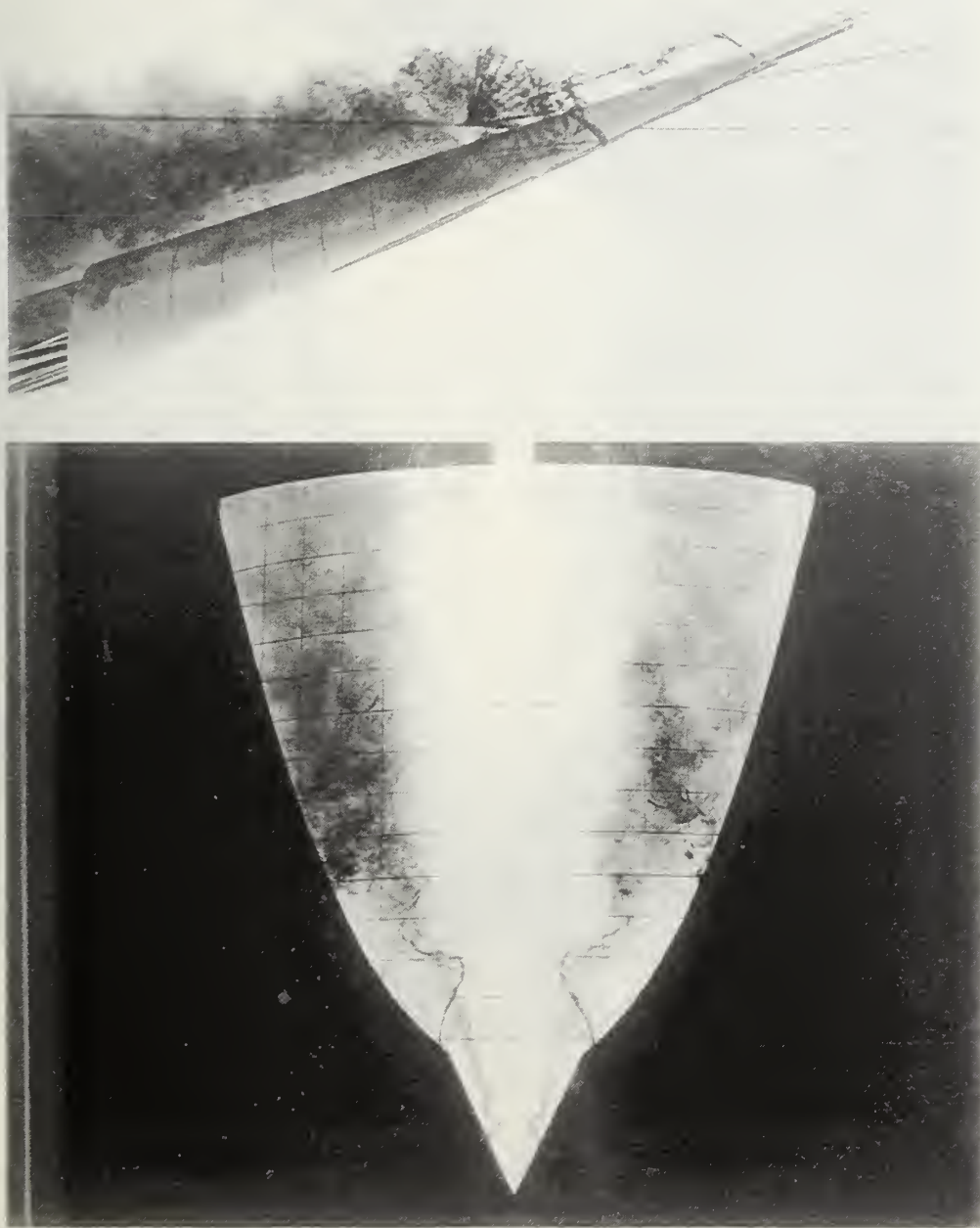


Figure 3.45 Modification Two, Entrainment, Angle of Attack Effects, $\alpha=16^\circ$,
 $\beta=0^\circ$

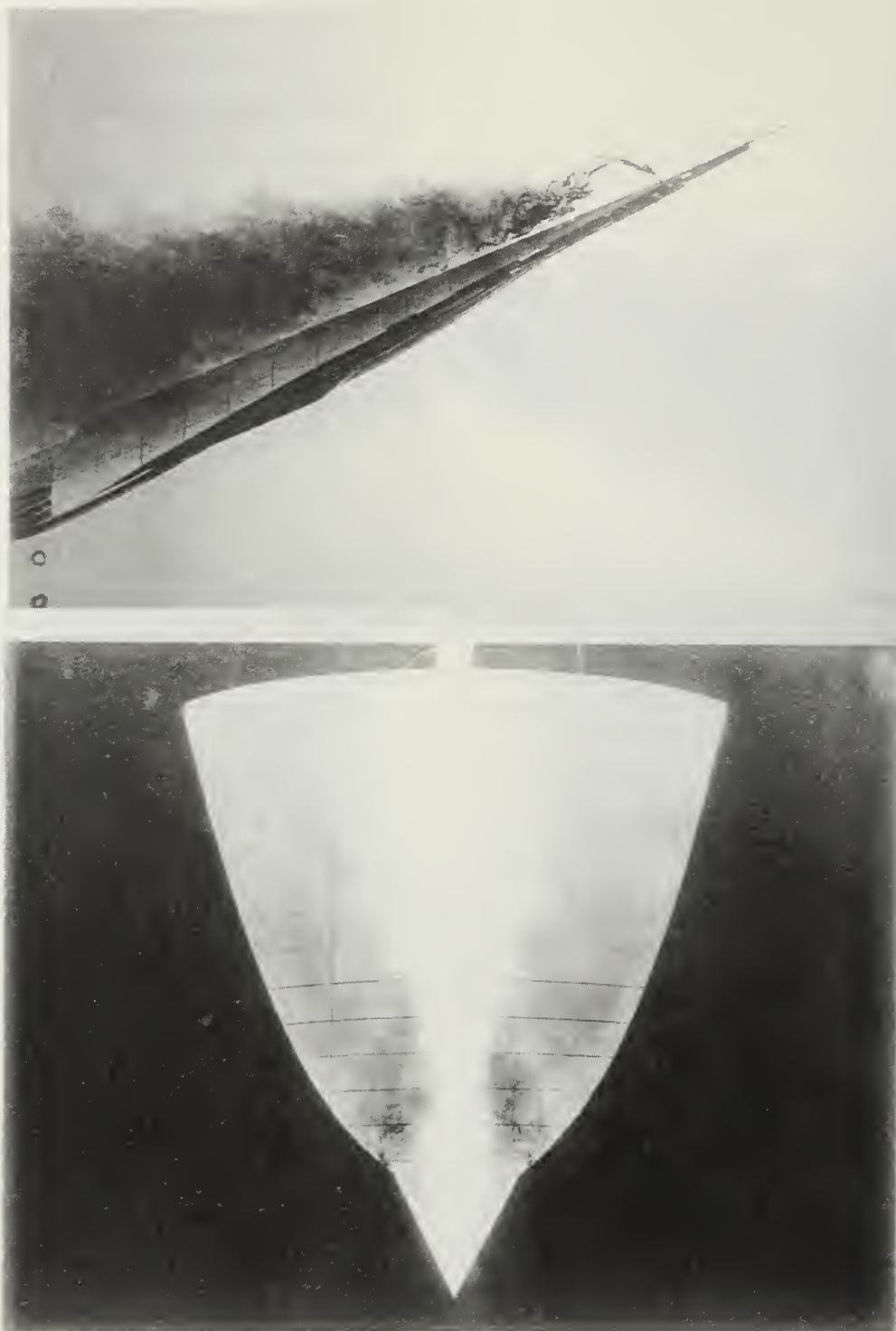


Figure 3.46 Modification Two, Entrainment, Angle of Attack Effects, $\alpha=24^\circ$,
 $\beta=0^\circ$

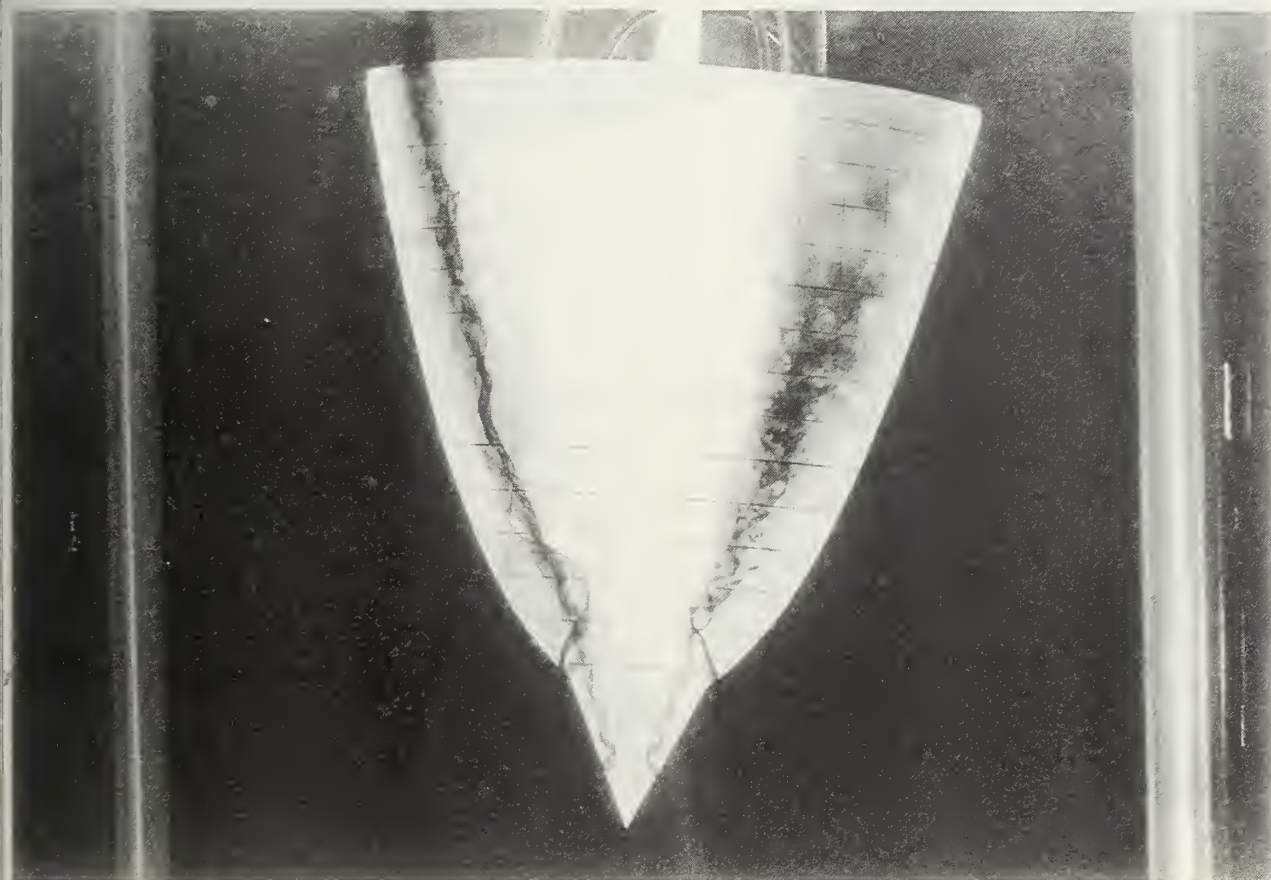


Figure 3.47 Modification Two, Entrainment, Sideslip Effects, $\alpha=12^\circ$, $\beta=5^\circ$

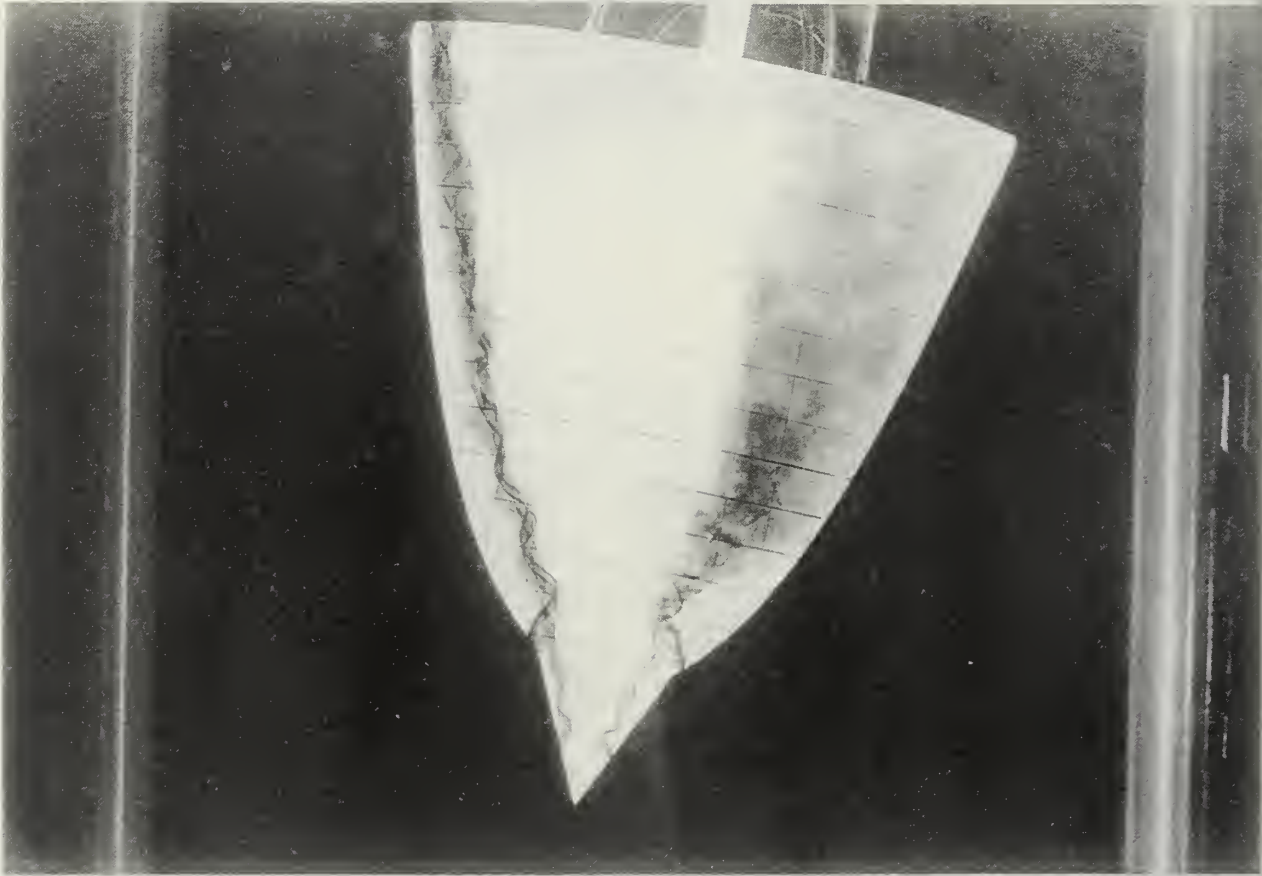


Figure 3.48 Modification Two, Entrainment, Sideslip Effects, $\alpha=12^\circ$, $\beta=10^\circ$

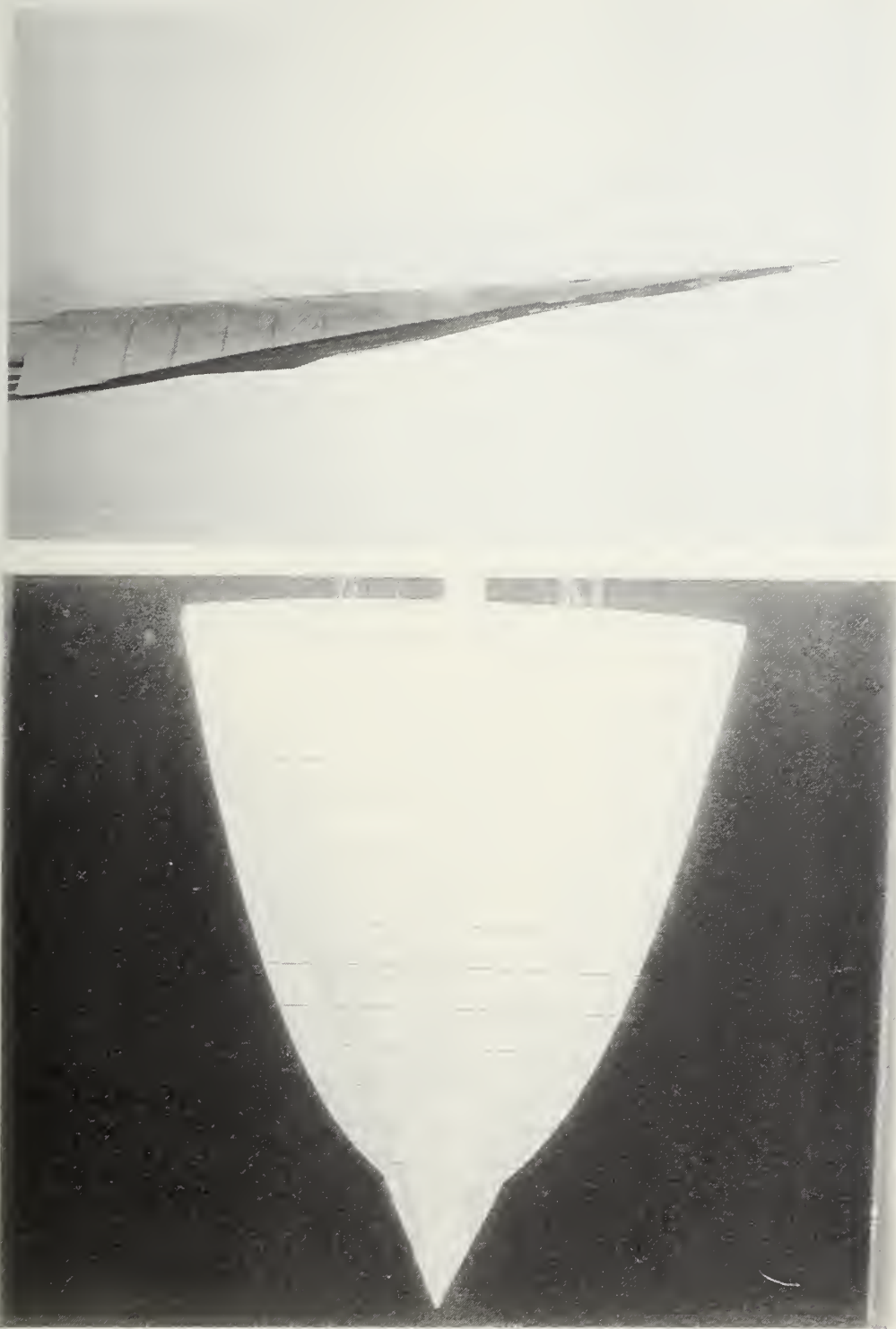


Figure 3.49 Angle of Attack Effects, Modification Two, $\alpha=4^\circ$, $\beta=0^\circ$

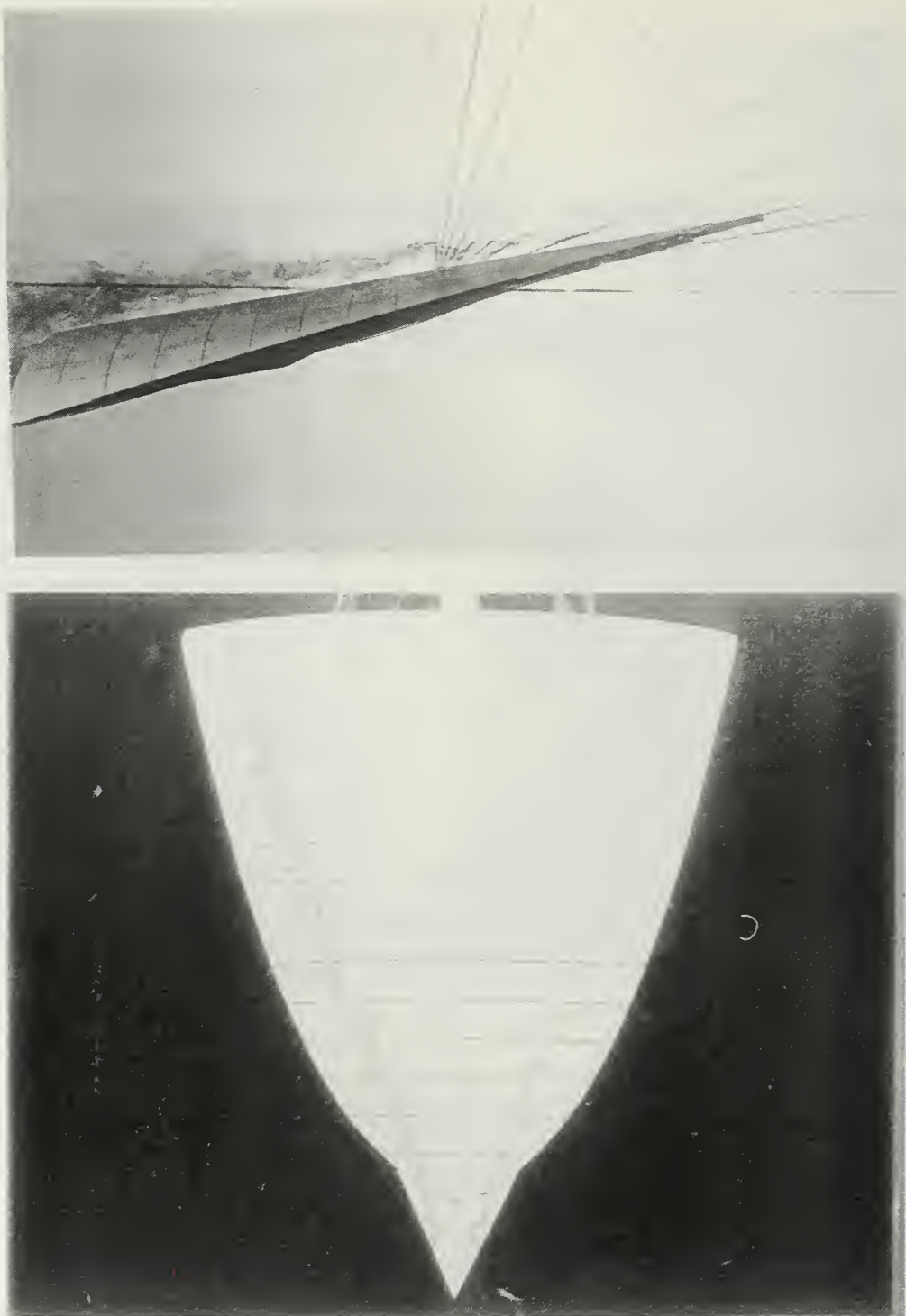


Figure 3.50 Angle of Attack Effects, Modification Two, $\alpha=12^\circ$, $\beta=0^\circ$



Figure 3.51 Angle of Attack Effects, Modification Two, $\alpha=16^\circ$, $\beta=0^\circ$

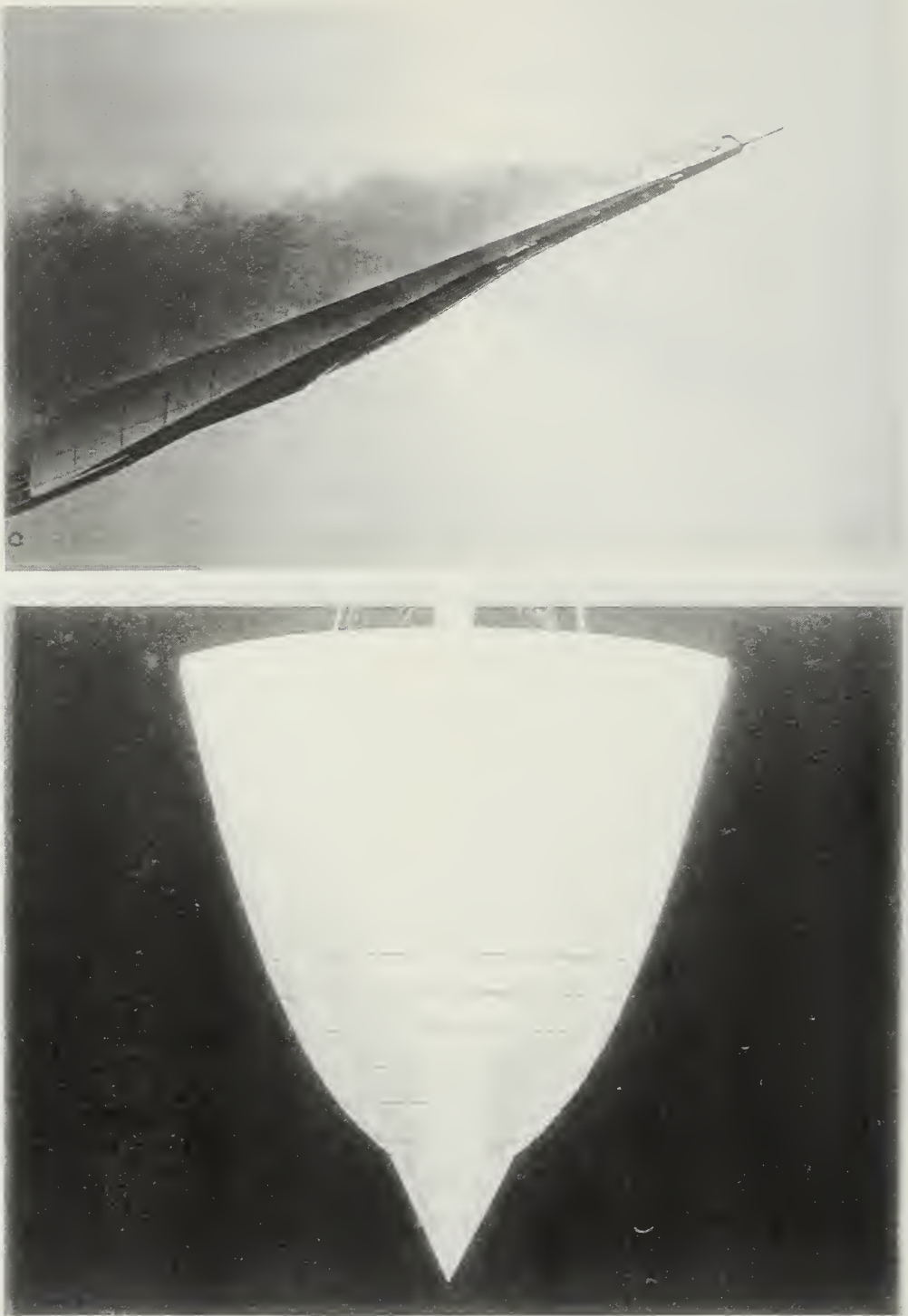


Figure 3.52 Angle of Attack Effects, Modification Two, $\alpha=20^\circ$, $\beta=0^\circ$

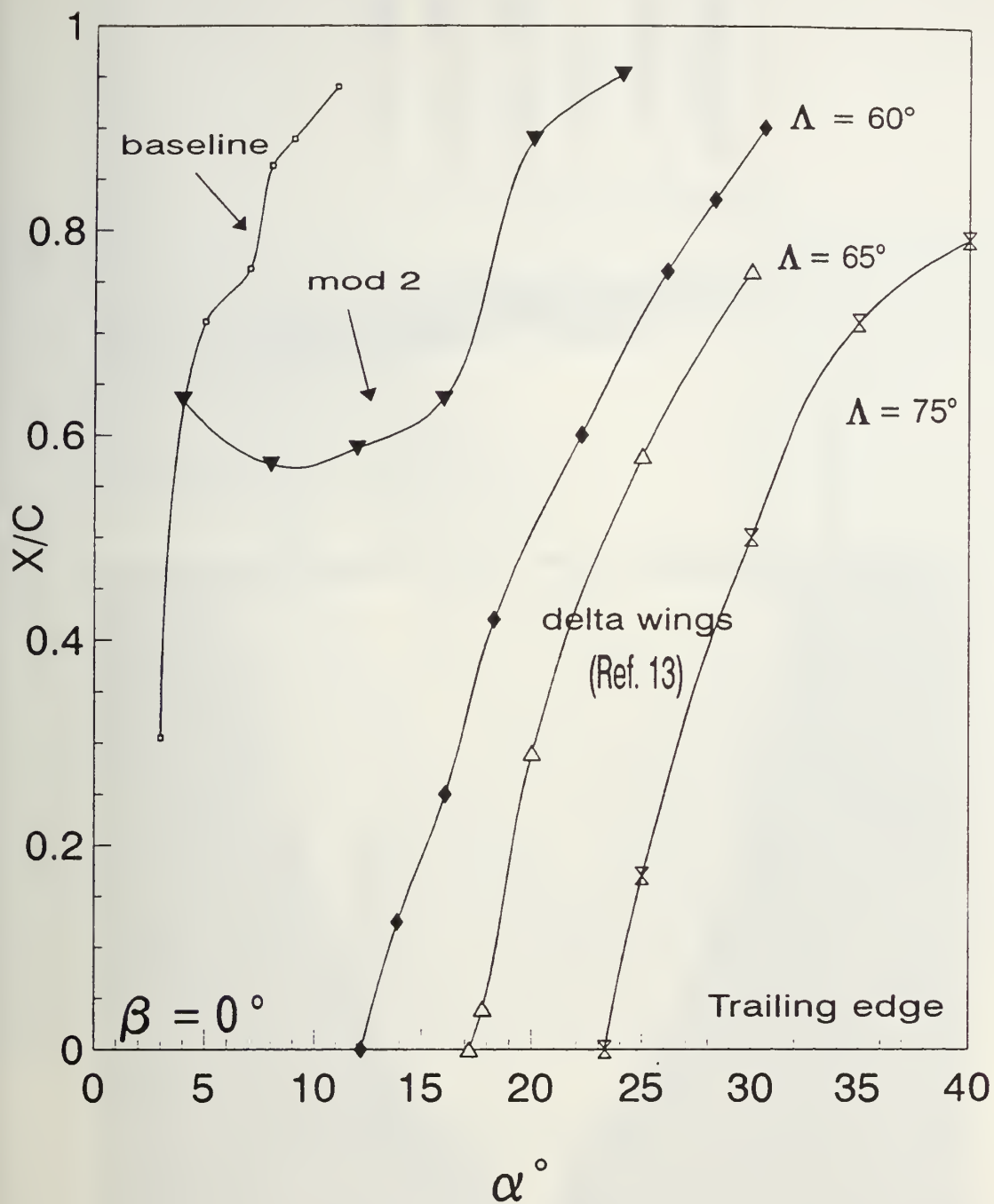


Figure 3.53 Vortex Burst Location as a Function of Angle of Attack, Baseline Model Compared to Modification Two and Delta Wing, $\beta=0^\circ$

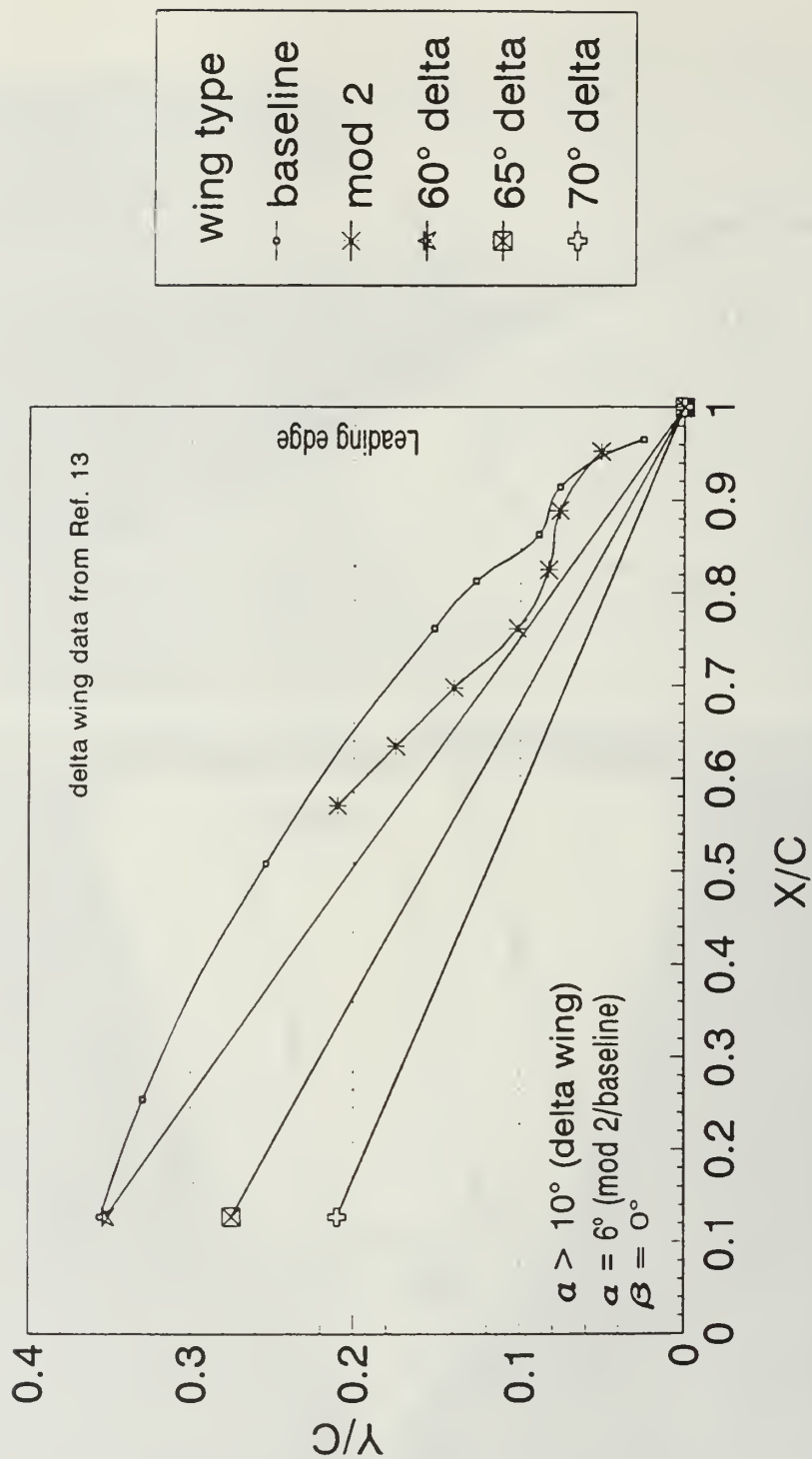


Figure 3.54 Baseline Model Compared to Modification Two and Delta Wing, Vortex Core Lateral Position, $\beta=0^\circ$

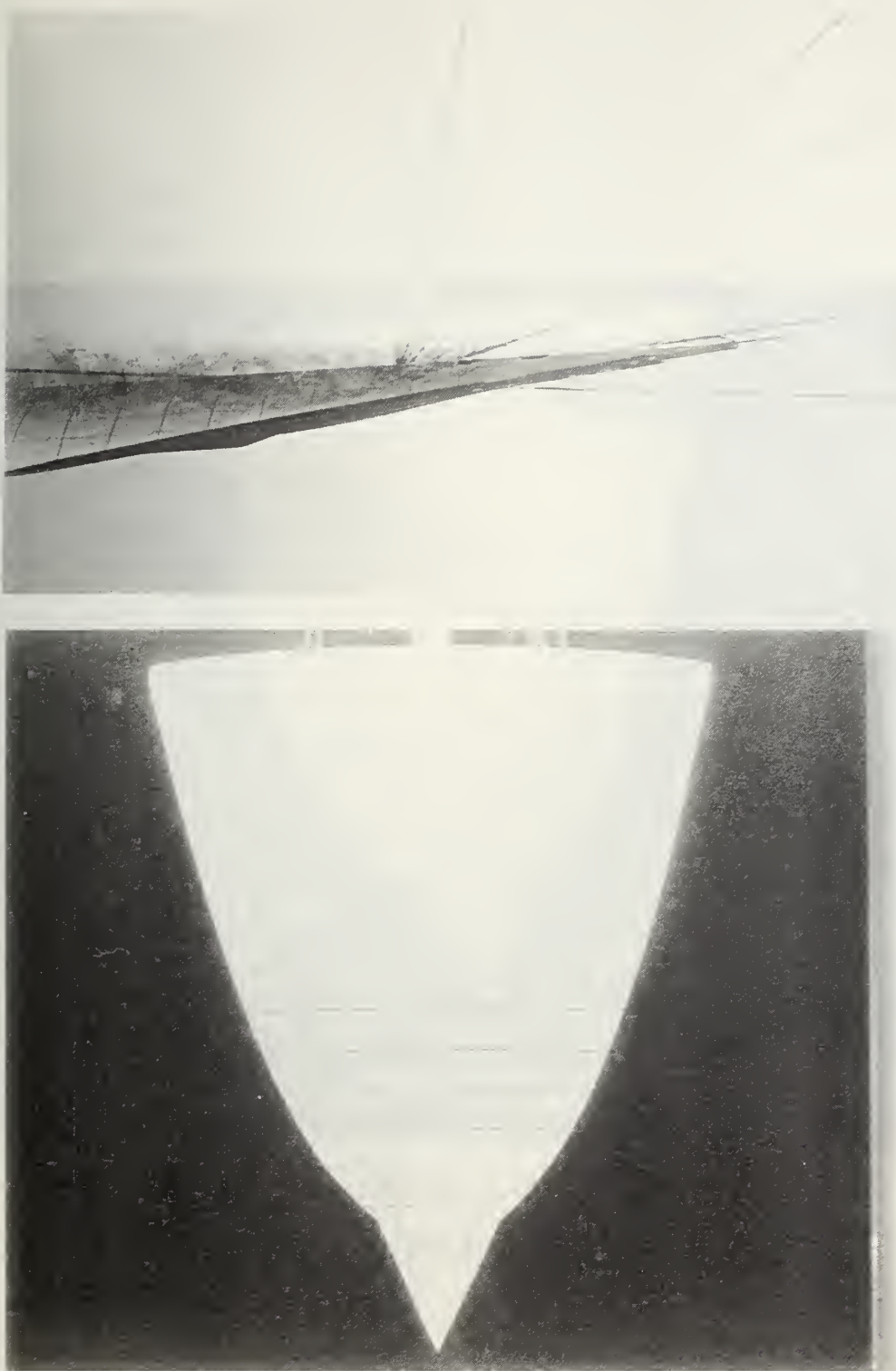


Figure 3.55 Sideslip Effects, Modification Two, $\alpha=8^\circ$, $\beta=0^\circ$

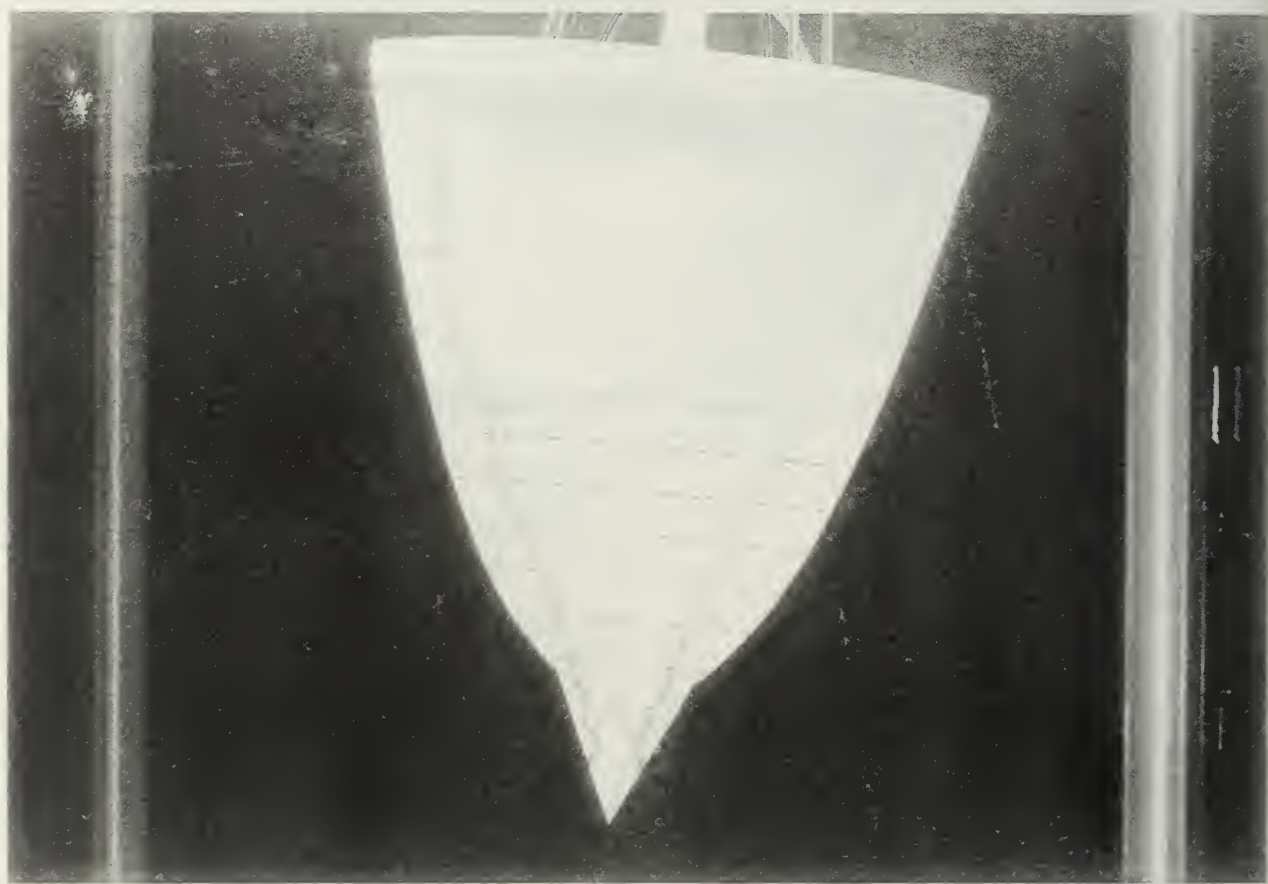


Figure 3.56 Sideslip Effects, Modification Two. $\alpha=8^\circ$, $\beta=5^\circ$

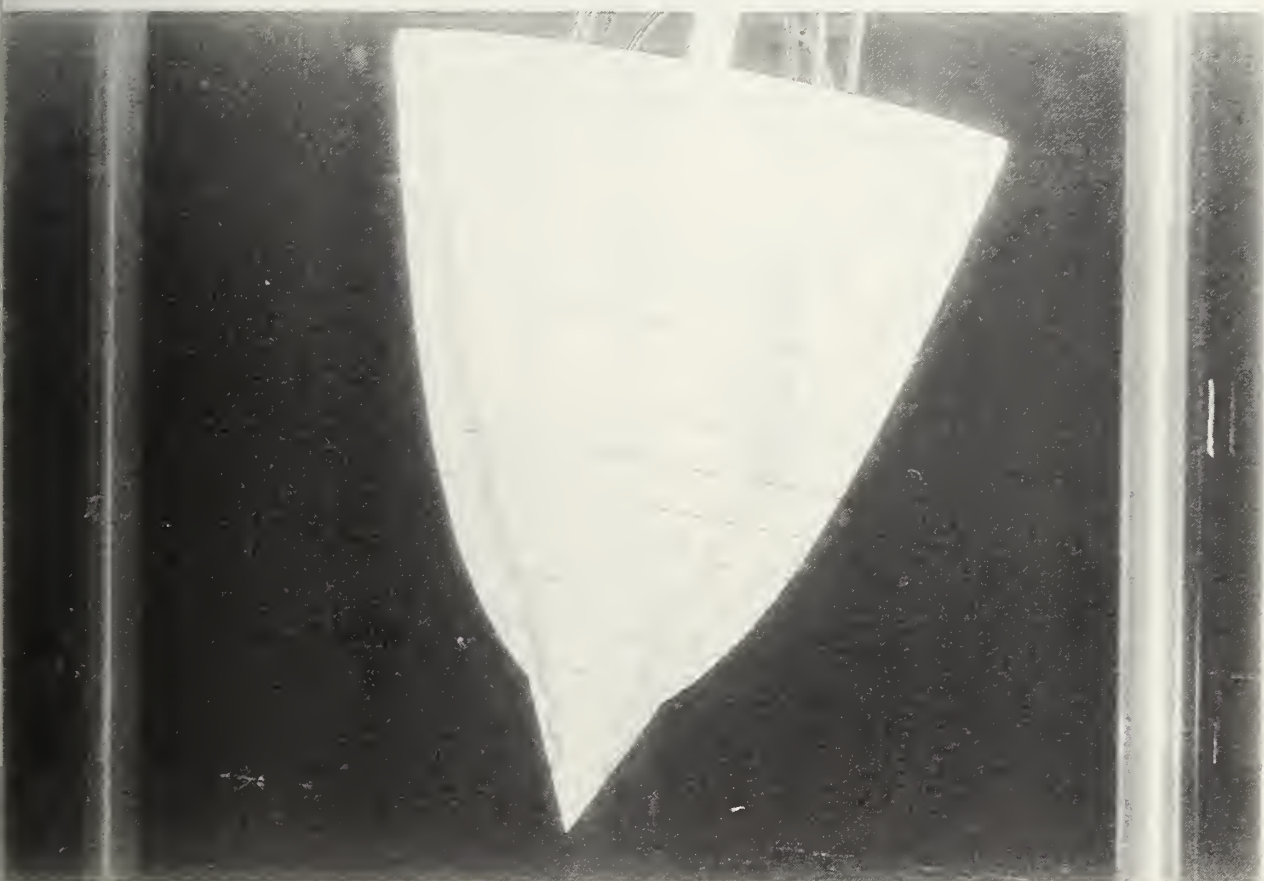


Figure 3.57 Sideslip Effects, Modification Two, $\alpha=8^\circ$, $\beta=10^\circ$

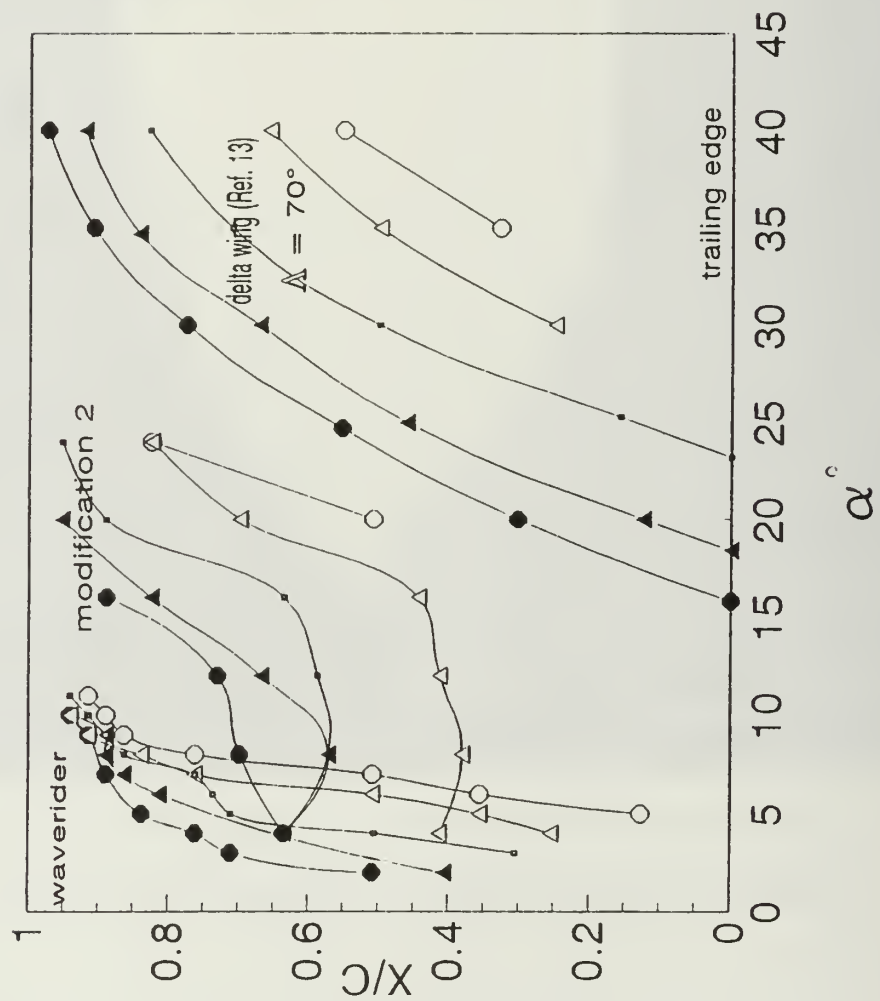


Figure 3.58 Modification Two, Vortex Burst Asymmetry

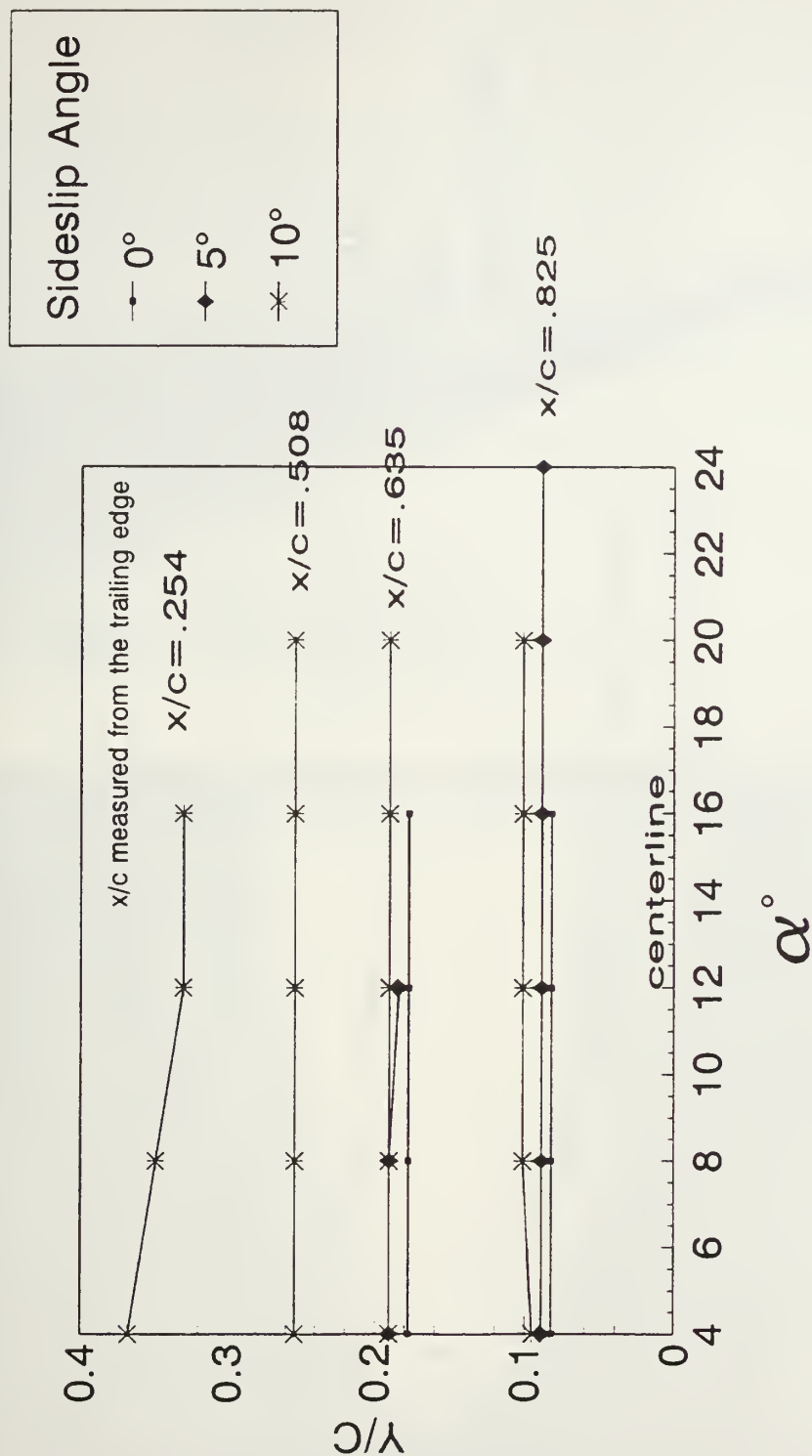


Figure 3.59 Modification Two, Sideslip Effects on Vortex Core Lateral Position (leeward Side)

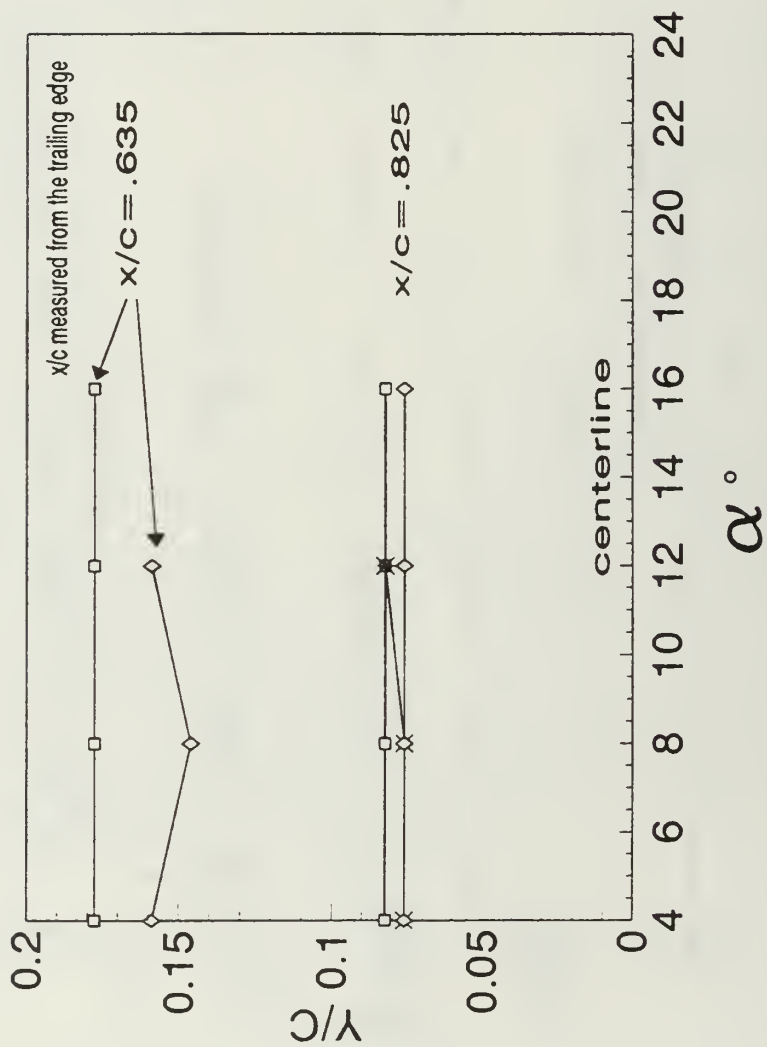


Figure 3.60 Modification Two, Sideslip Effects on Vortex Core Lateral Position (Windward Side)

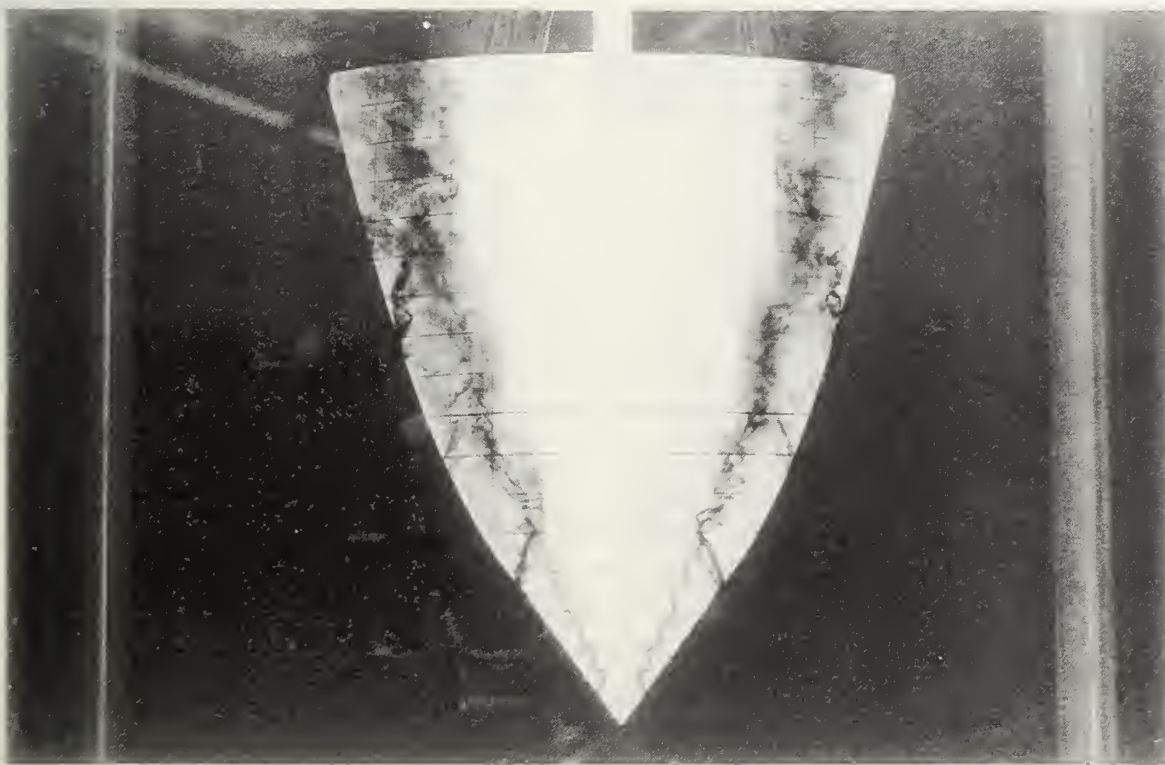
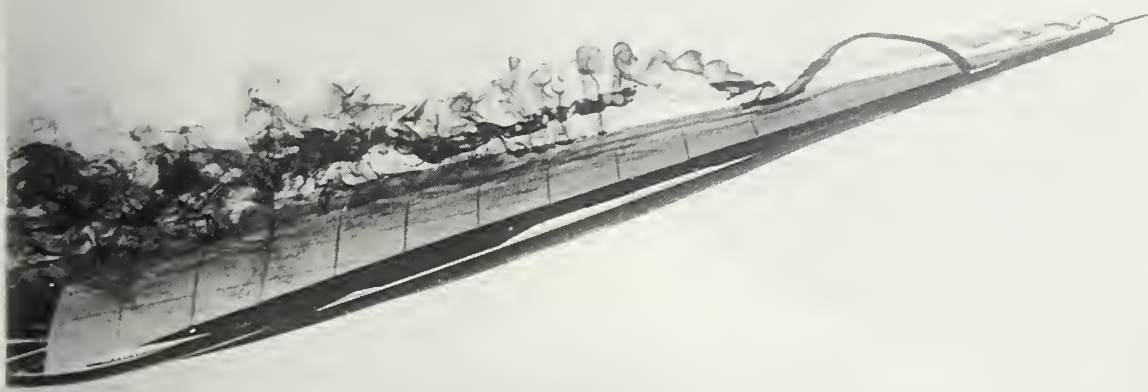


Figure 3.61 Modification Three Entrainment, Angle of Attack Effects, $\alpha=8^\circ$,
 $\beta=0^\circ$

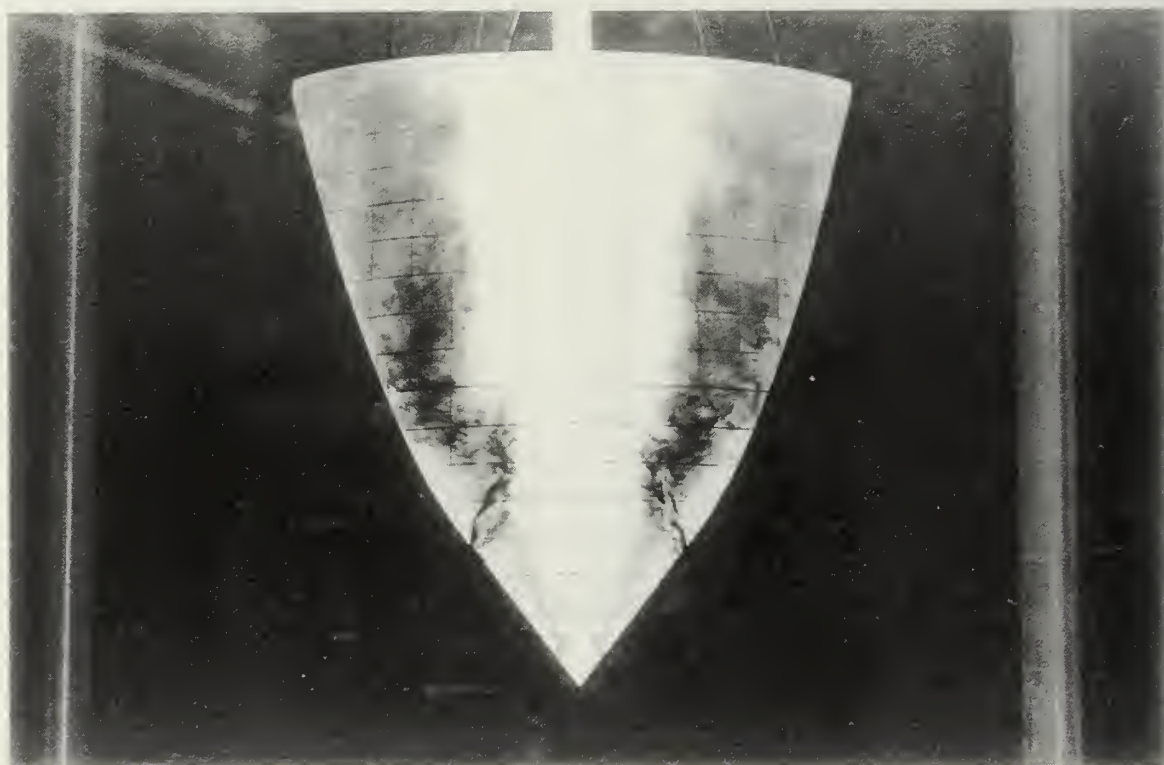


Figure 3.62 Modification Three, Entrainment, Angle of Attack Effects,
 $\alpha=16^\circ$, $\beta=0^\circ$

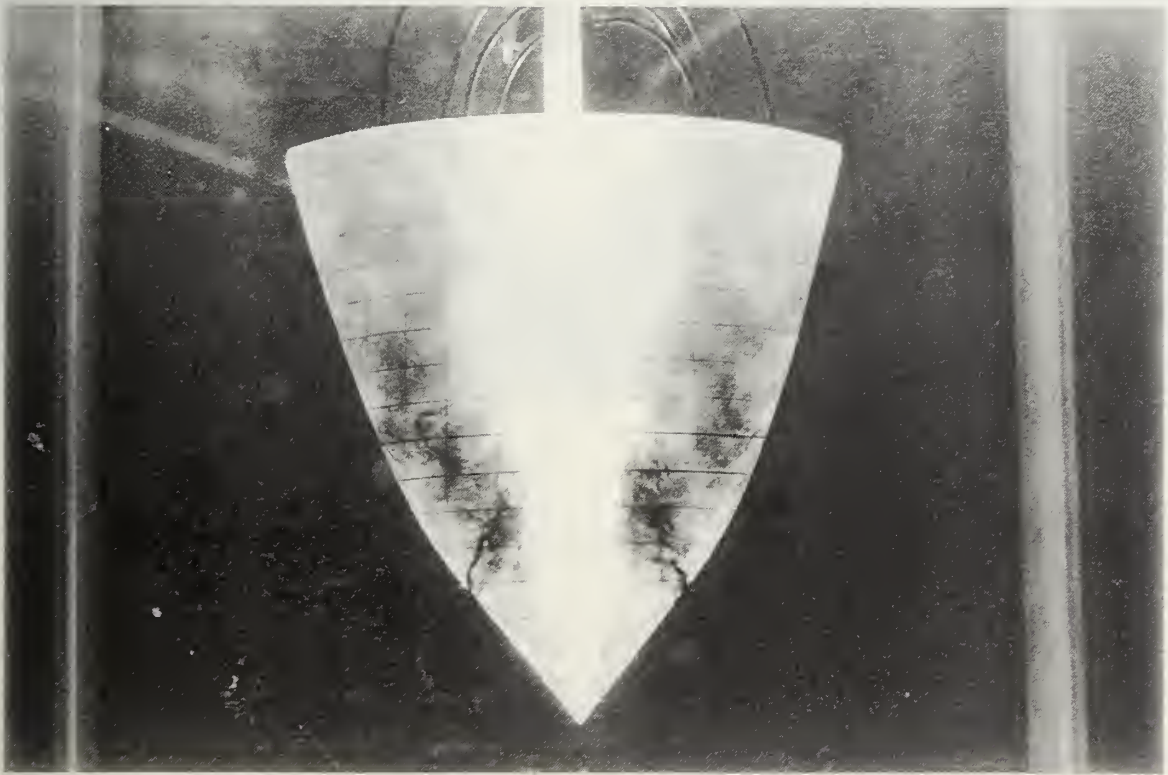


Figure 3.63 Modification Three, Entrainment, Angle of Attack Effects,
 $\alpha=20^\circ$, $\beta=0^\circ$

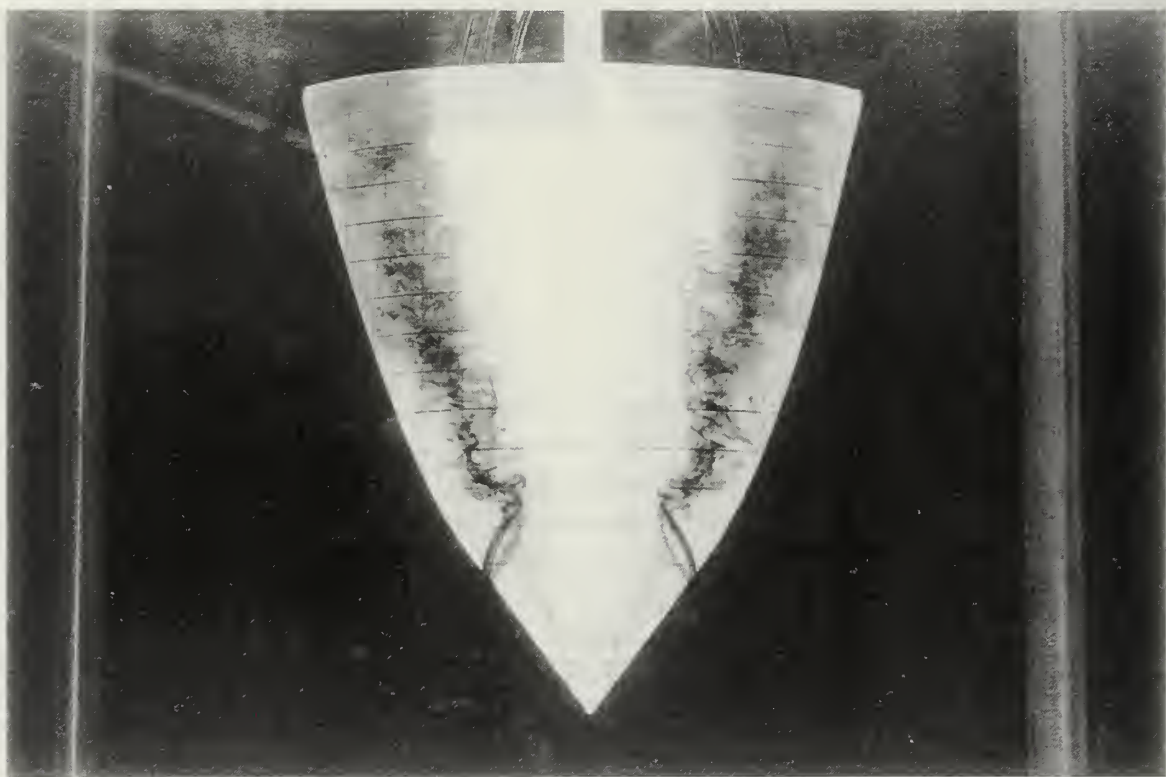


Figure 3.64 Modification Three. Entrainment, Sideslip Effects, $\alpha=12^\circ$, $\beta=0^\circ$

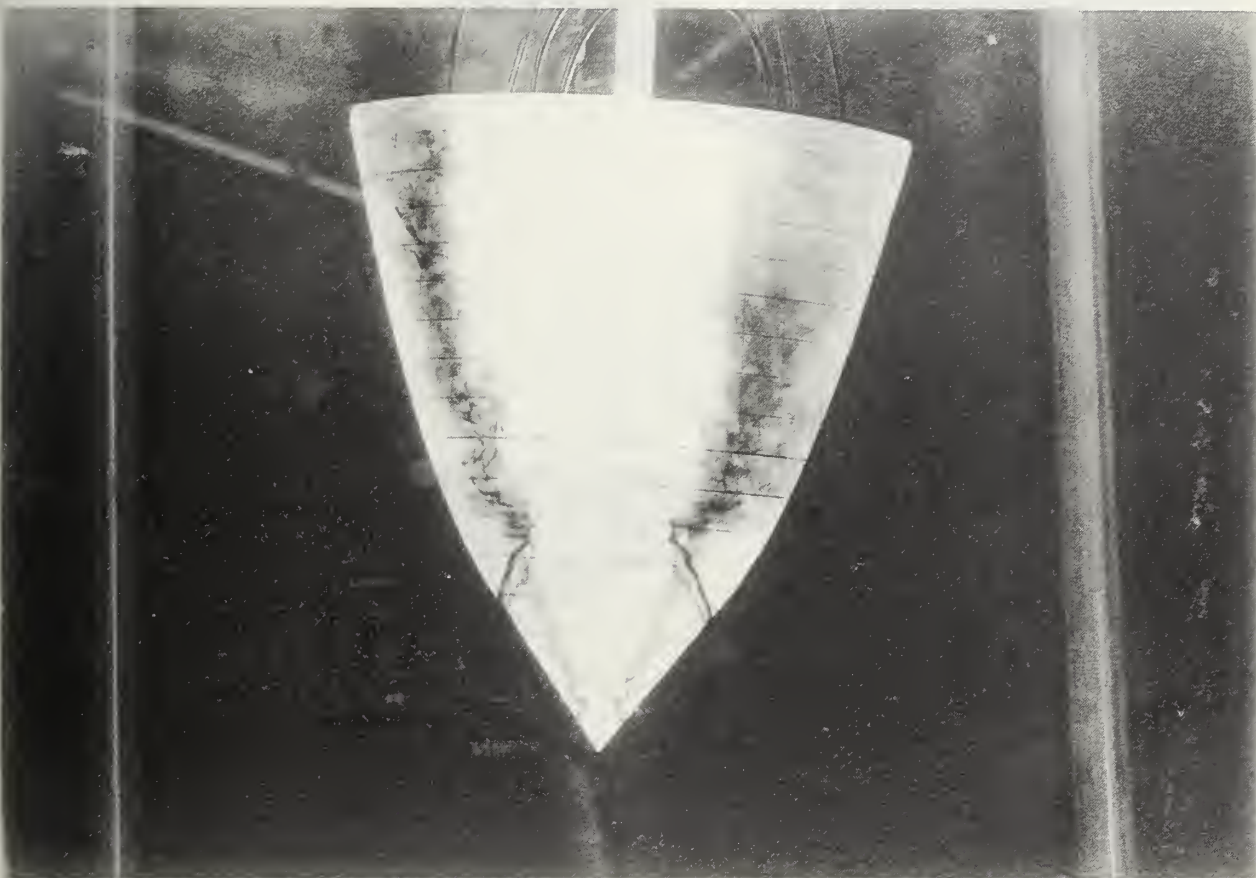


Figure 3.65 Modification Three, Entrainment, Sideslip Effects, $\alpha=12^\circ$, $\beta=5^\circ$

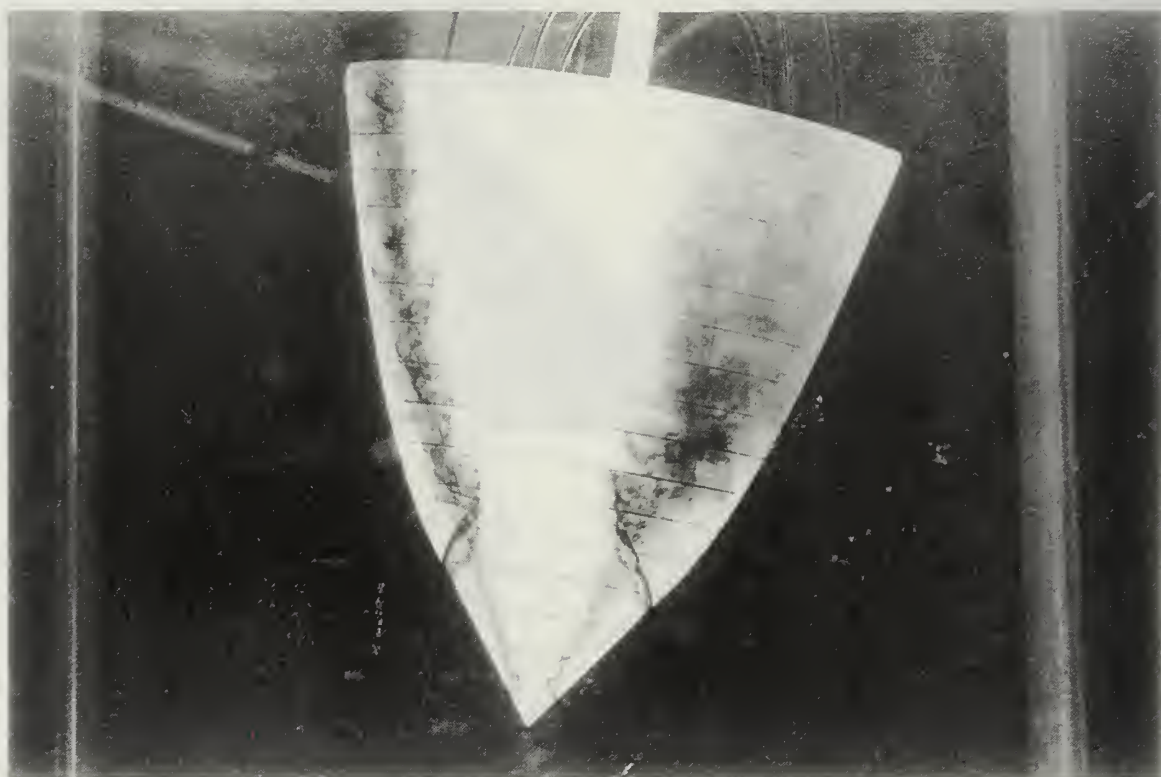


Figure 3.66 Modification Three, Entrainment, Sideslip Effects, $\alpha=12^\circ$, $\beta=10^\circ$



Figure 3.67 Modification Three, Entrainment, Sideslip Effects, $\alpha=8^\circ$, $\beta=+5^\circ$



Figure 3.68 Modification Three, Entrainment, Sideslip Effects, $\alpha=8^\circ$, $\beta=0^\circ$



Figure 3.69 Modification Three. Entrainment, Sideslip Effects, $\alpha=8^\circ$, $\beta=-5^\circ$

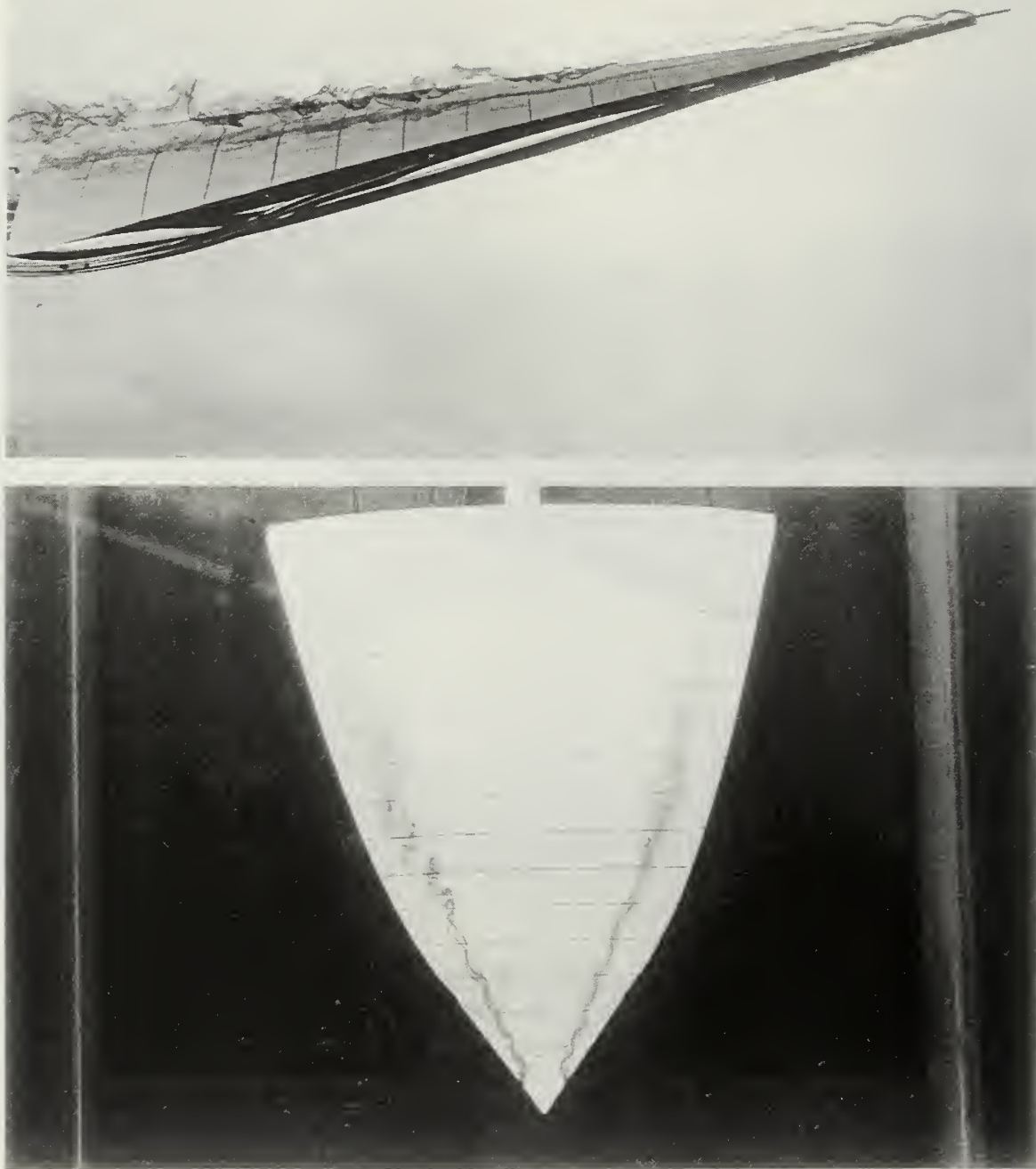


Figure 3.70 Angle of Attack Effects, Modification Three, $\alpha=4^\circ$, $\beta=0^\circ$

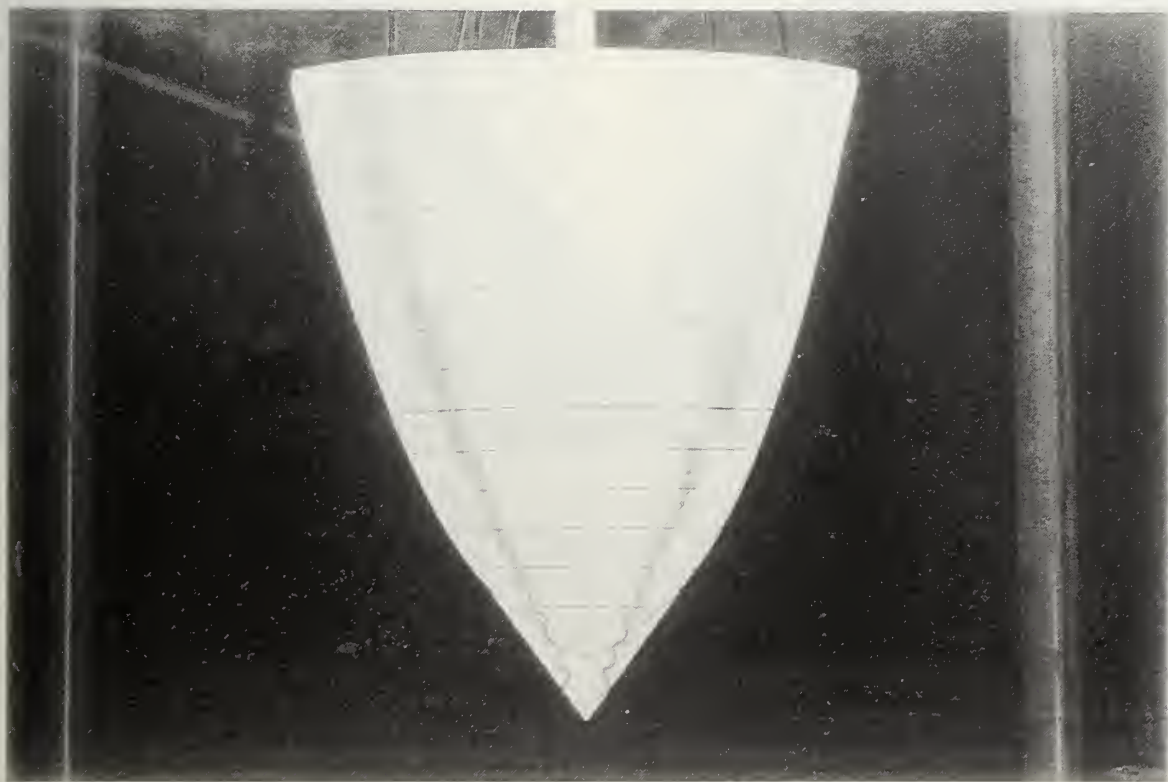


Figure 3.71 Angle of Attack Effects, Modification Three, $\alpha=8^\circ$, $\beta=0^\circ$

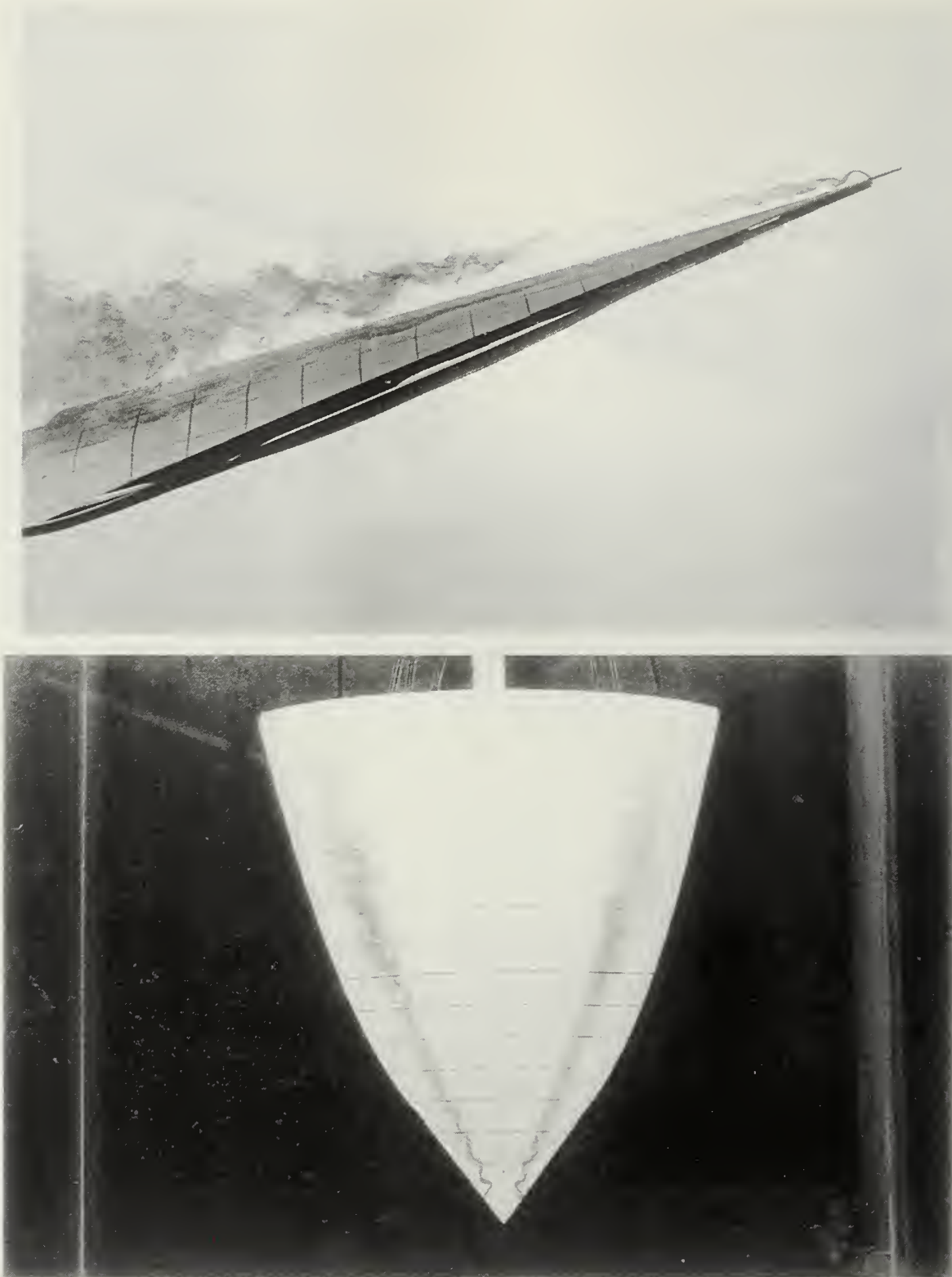


Figure 3.72 Angle of Attack Effects, Modification Three, $\alpha=12^\circ$, $\beta=0^\circ$

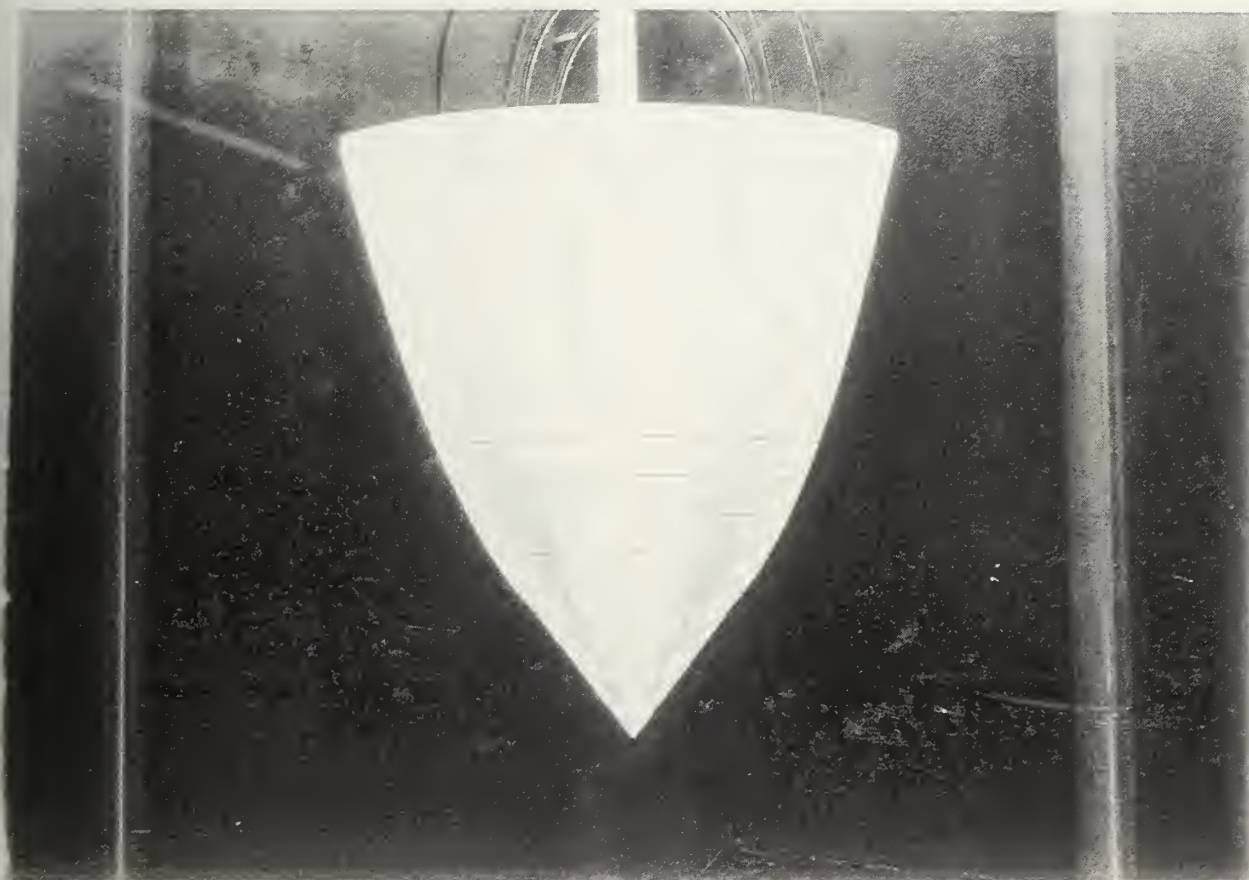


Figure 3.73 Angle of Attack Effects, Modification Three, $\alpha=16^\circ$, $\beta=0^\circ$

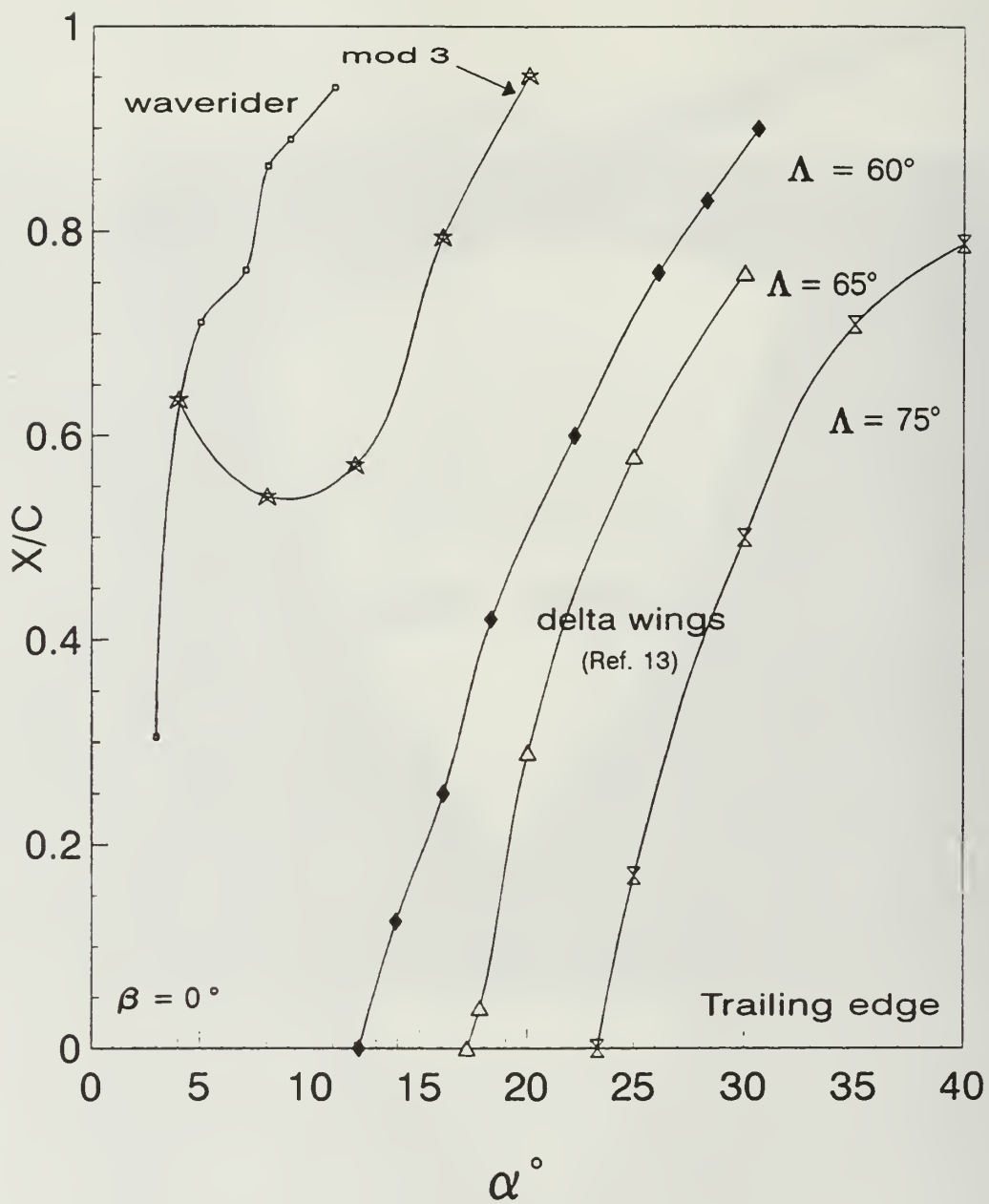


Figure 3.74 Vortex Burst Location as a Function of Angle of Attack, Baseline Model Compared to Modification Three and Delta Wing, $\beta=0^\circ$

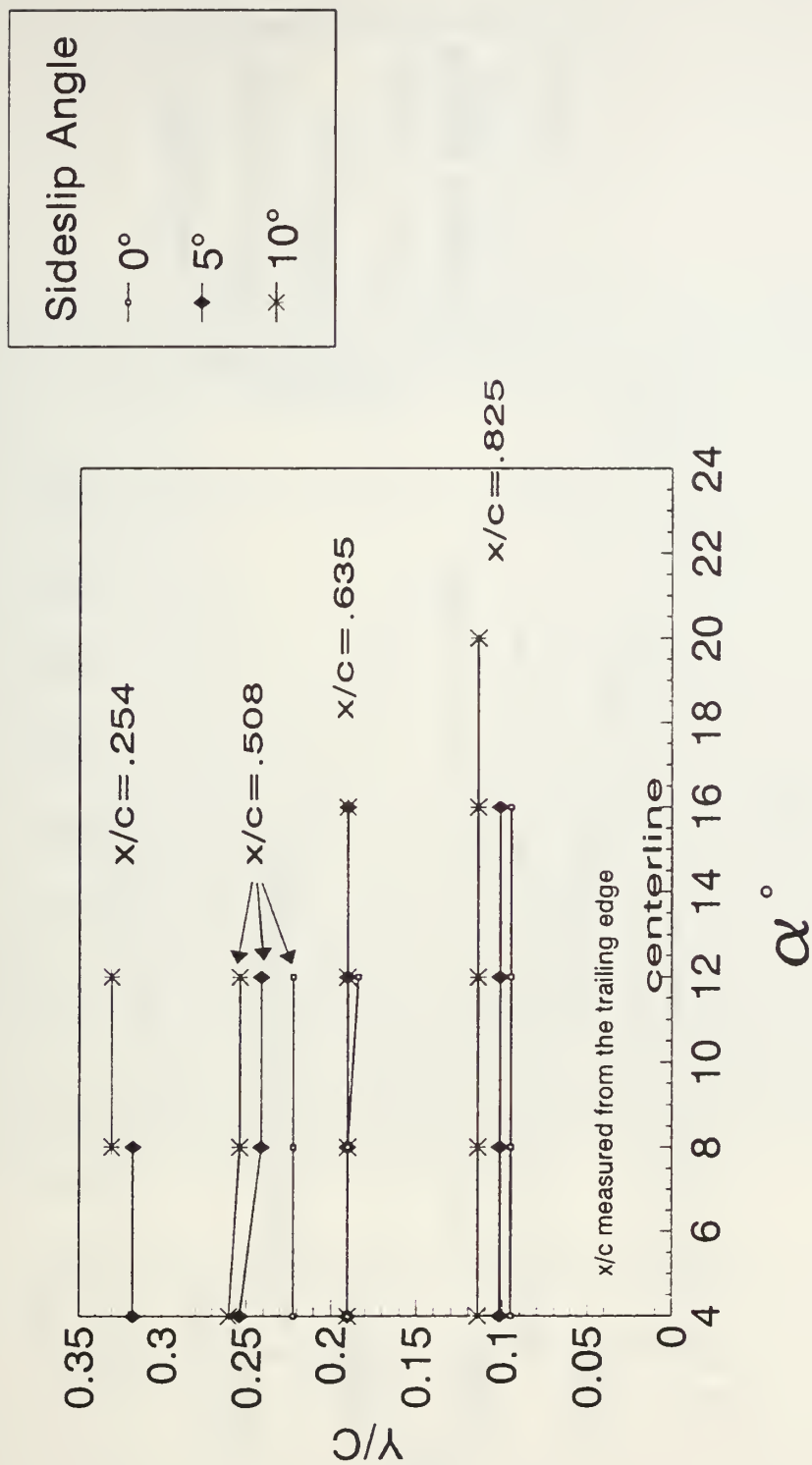


Figure 3.75 Modification Three, Sideslip Effects on Vortex Core Lateral Position (Leeward Side)

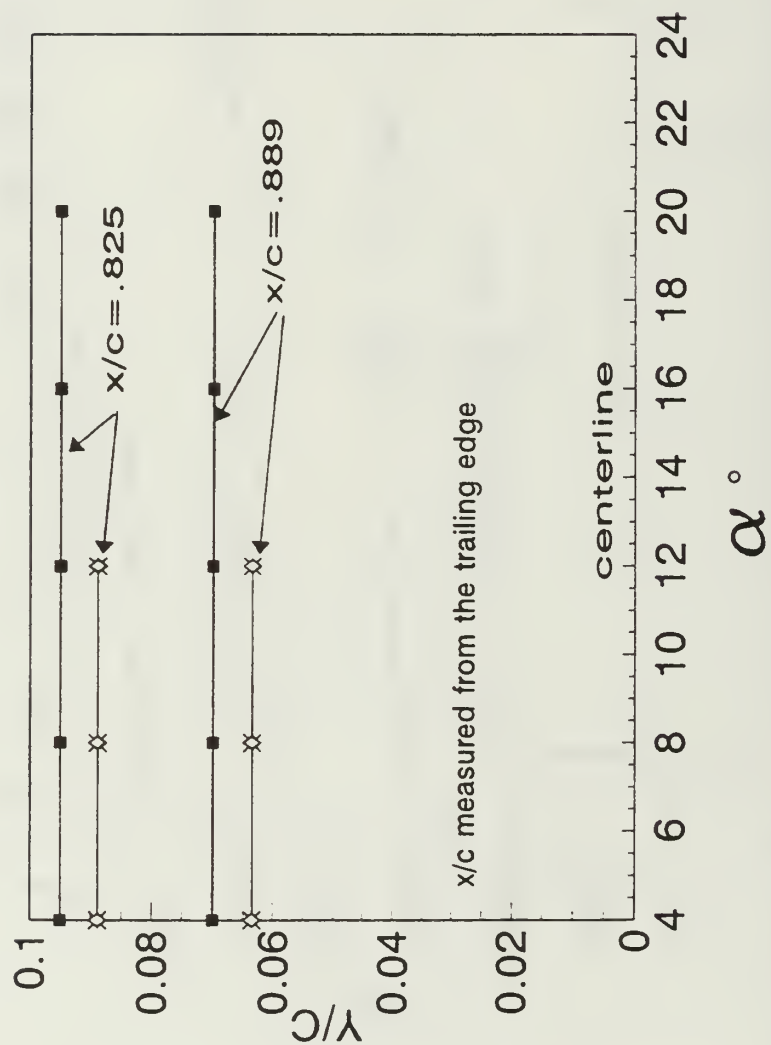


Figure 3.76 Modification Three, Sideslip Effects on Vortex Core Lateral Position (Windward Side)

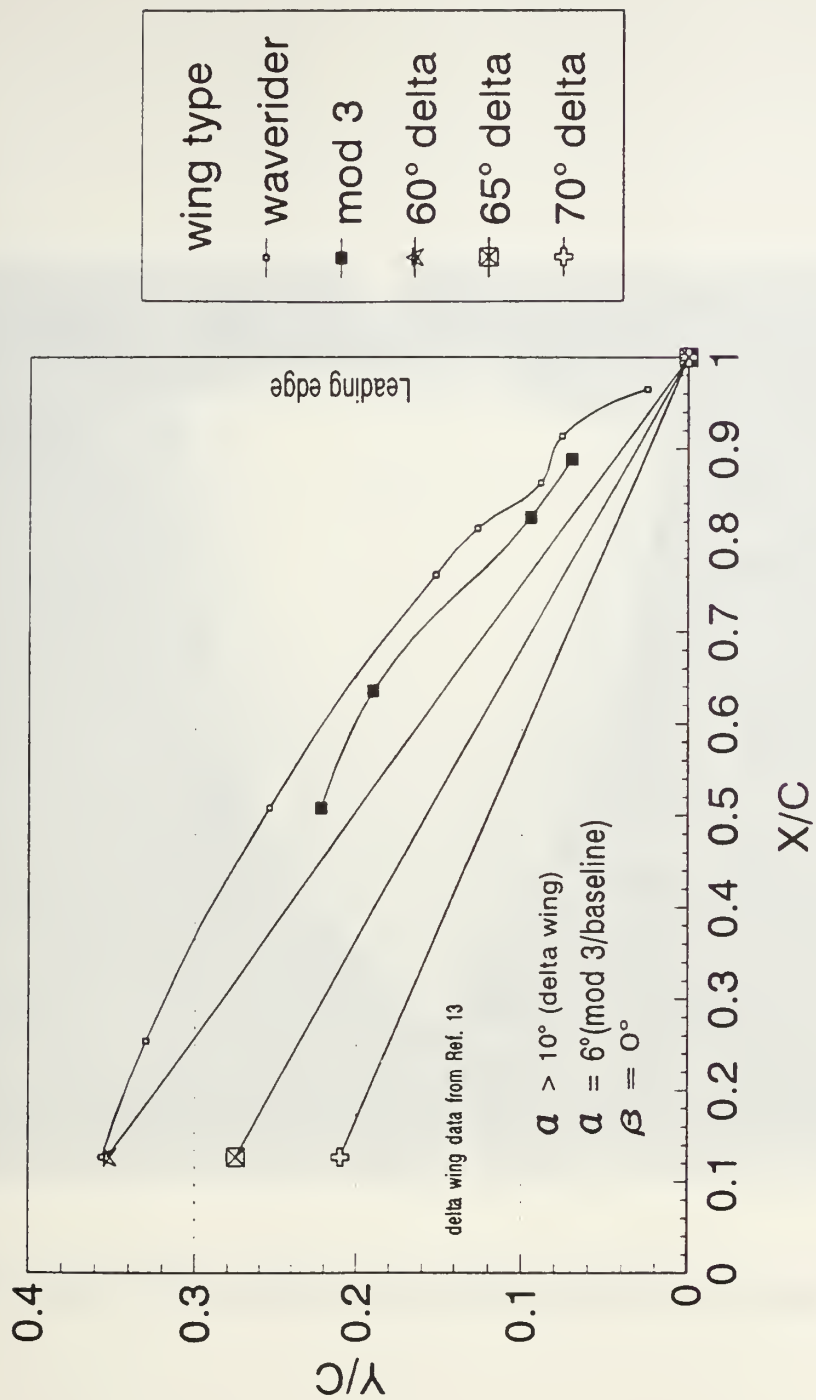


Figure 3.77 Baseline Model Compared to Modification Three and Delta Wing, Vortex Core Lateral Position, $\beta=0^\circ$

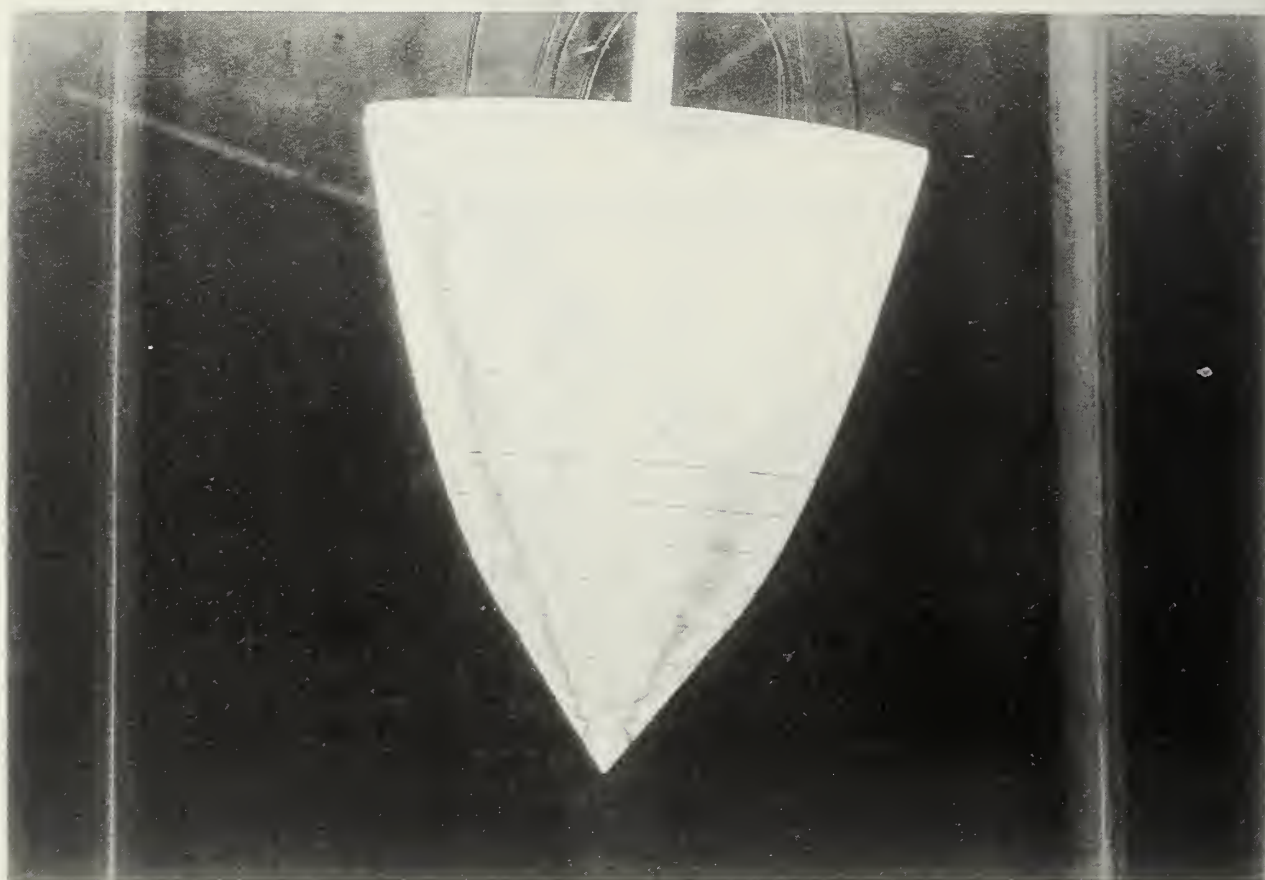


Figure 3.78 Sideslip Effects, Modification Three, $\alpha=8^\circ$, $\beta=5^\circ$

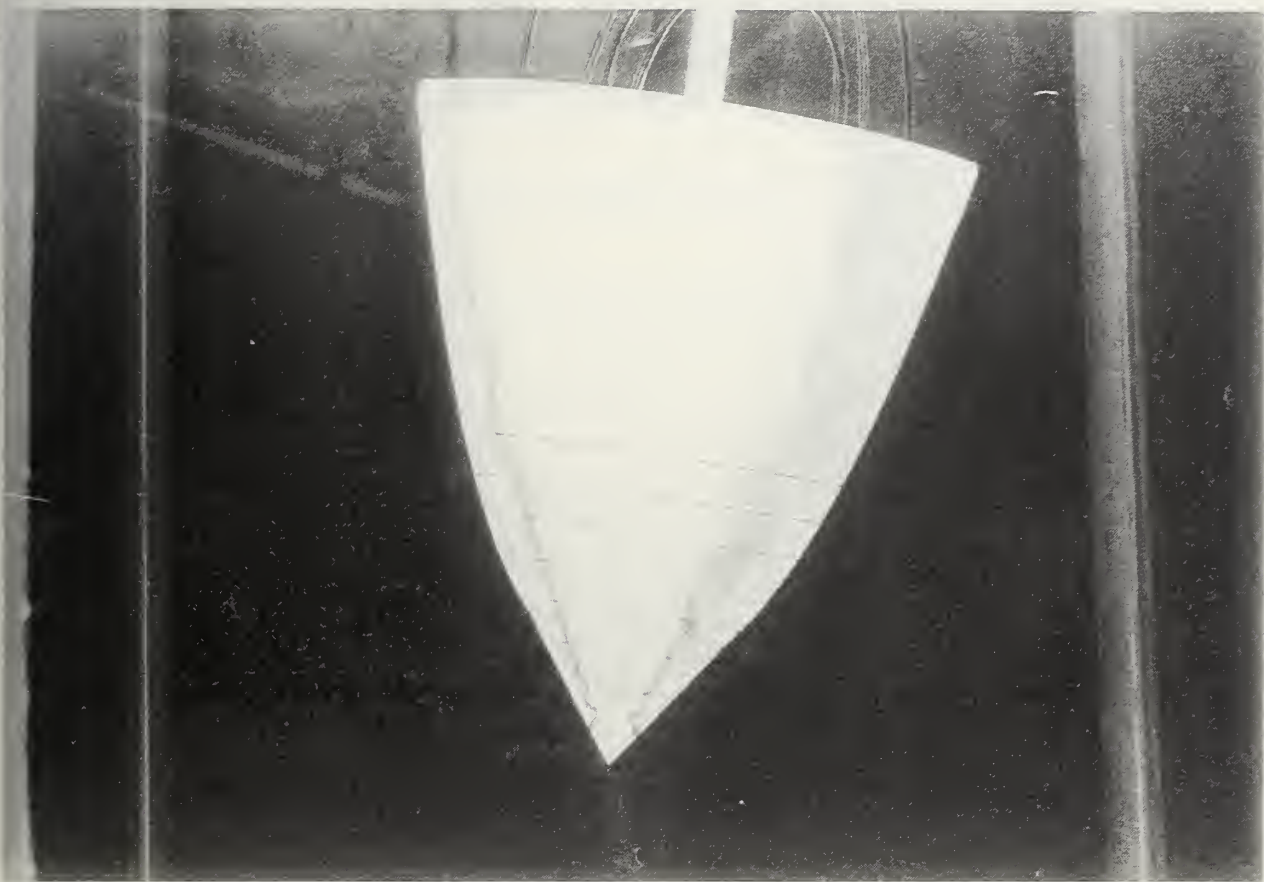


Figure 3.79 Sideslip Effects, Modification Three, $\alpha=8^\circ$, $\beta=10^\circ$

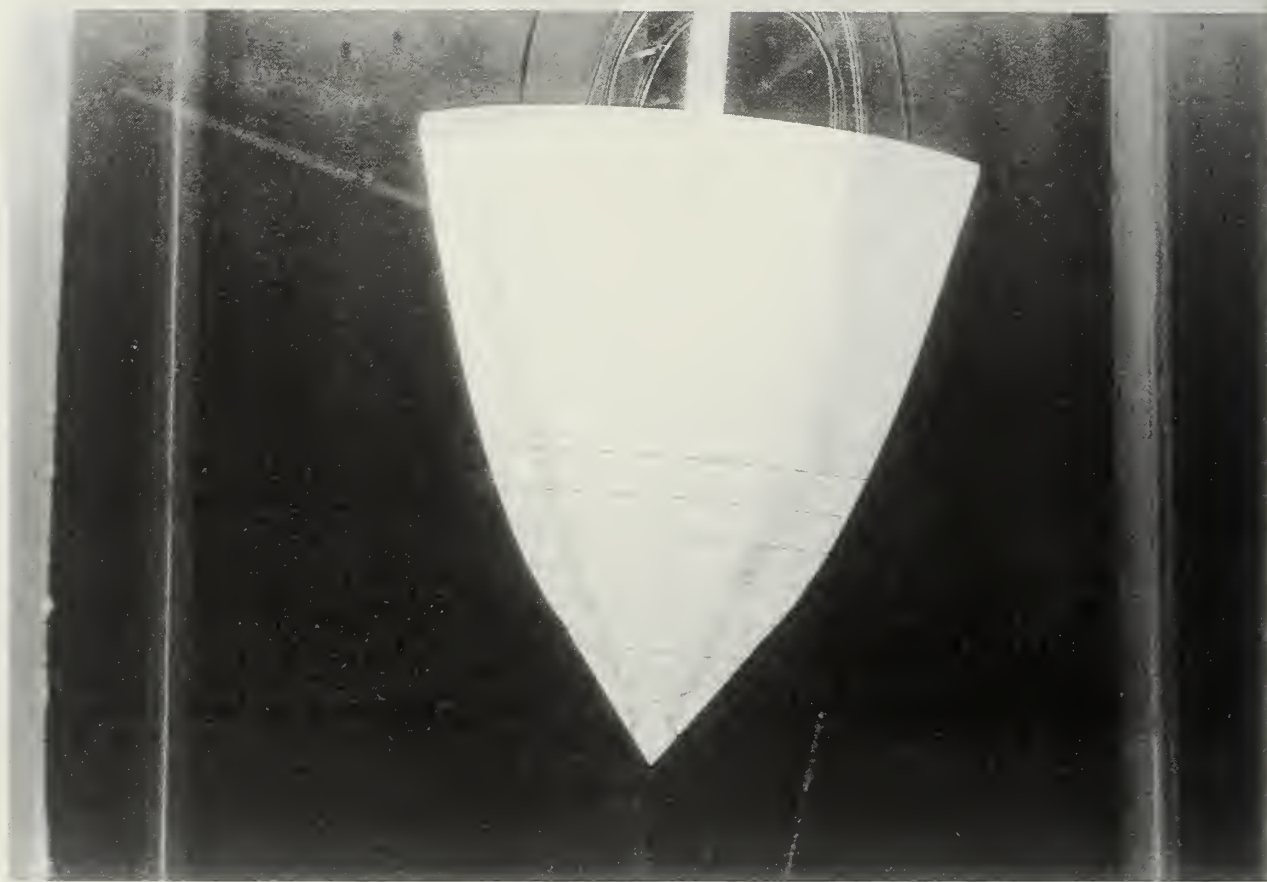


Figure 3.80 Sideslip Effects, Modification Three, $\alpha=16^\circ$, $\beta=5^\circ$

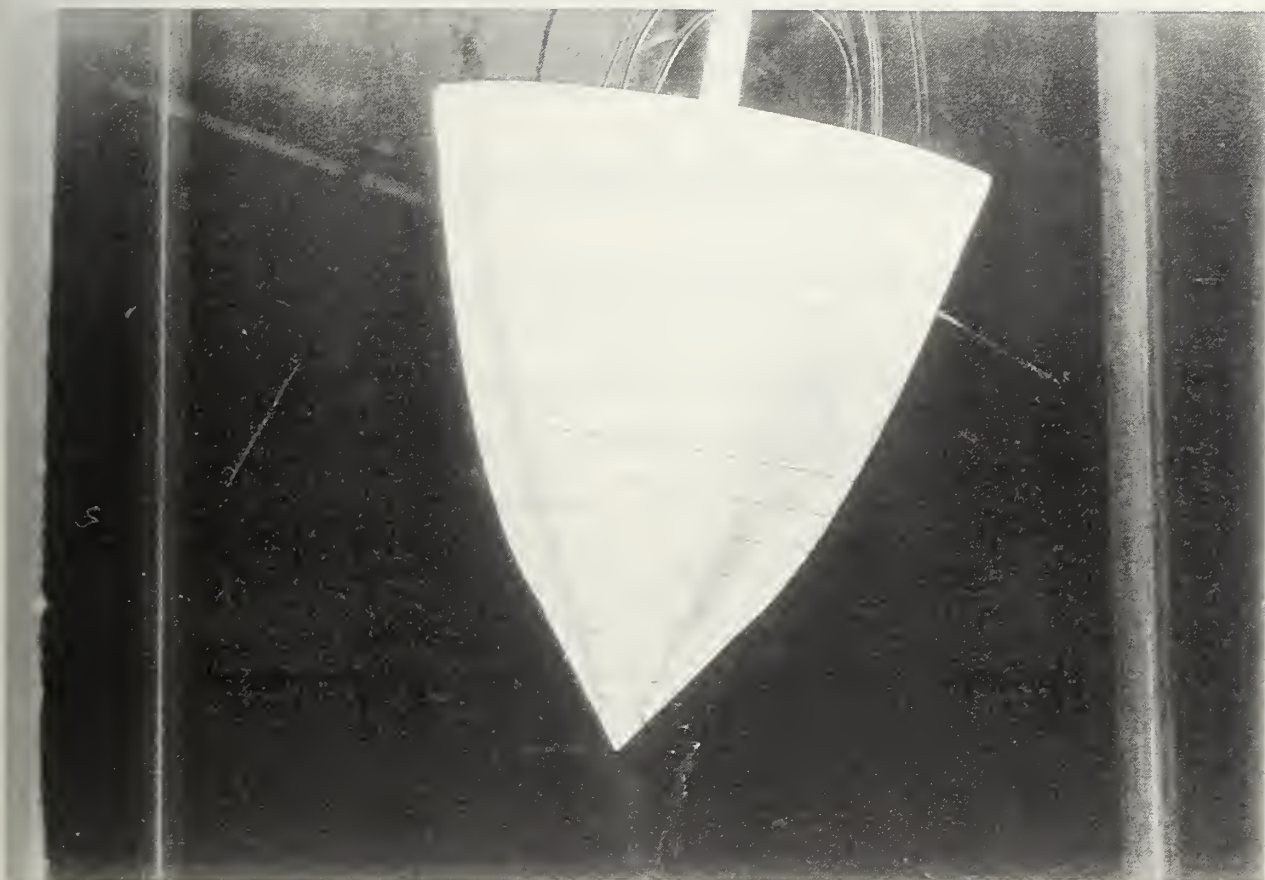


Figure 3.81 Sideslip Effects, Modification Three, $\alpha=16^\circ$, $\beta=10^\circ$

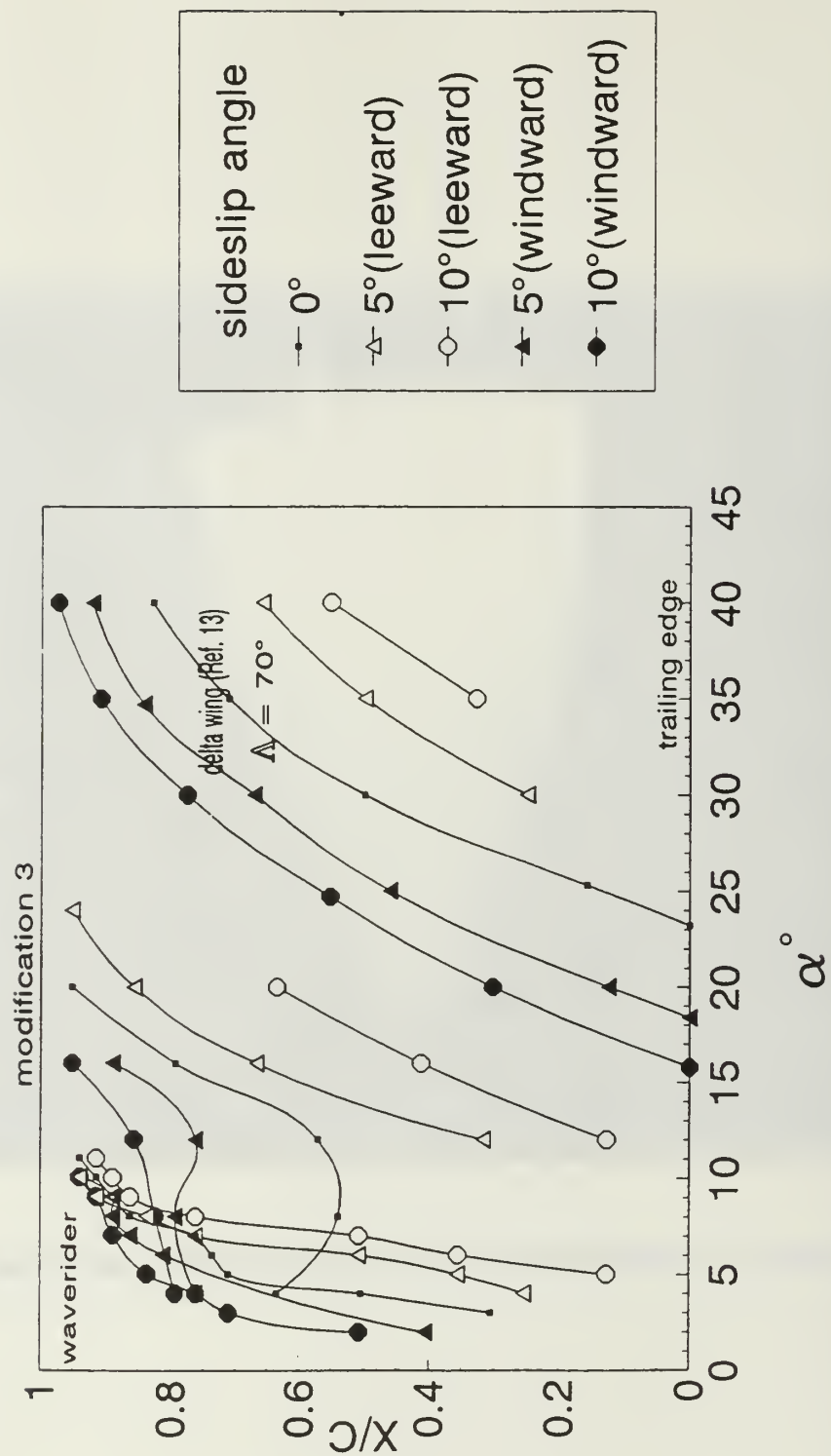


Figure 3.82 Modification Three, Vortex Burst Asymmetry

IV. CONCLUSIONS AND RECOMMENDATIONS

A low speed flow visualization investigation was performed to study the development and bursting phenomena of a 1.1% scale model of a Mach 6 viscous optimized $[(L/D)(I_{sp})]$ waverider aircraft using dye injection in the NPS water tunnel. The main focus of this study was two-fold:

1. study the effect of angle of attack and sideslip on the vortical flowfield.
2. study the sweep and area ratio effects on vortex core stability of several modifications of the baseline model configuration.

The water tunnel visualization data reported here is believed to be the first of its kind for a waverider type aircraft. The following conclusions are drawn from the results of the experimental investigation.

A. BASELINE MODEL

1. Angle of Attack Effects

As the angle of attack increases from 2° to 10° , a pair of symmetric vortices develops and the bursting locations move upstream over the top surface of the model. The vortex becomes completely turbulent at 12° angle of attack.

Lateral vortex core location parallels the leading edge and is independent of angle of attack. Vertical core location above the model surface increases with angle of attack but vortex breakdown occurs at such low angles of attack that changes in vortex core angle of attack were too small to measure.

2. Sideslip Effects

Vortex core bursting location is also a function of sideslip angle. At a constant angle of attack, as sideslip angle is increased, the leeward vortex burst

location moves downstream and parallel to the leading edge and the windward vortex burst location moves forward parallel to the leading edge. Vortex burst asymmetry decreases at approximately 9° angle of attack. Lateral vortex core location changes with sideslip angle. The leeward core moves outboard of its 0° yaw position and the windward core moves inboard inboard of its 0° yaw position.

B. APEX DELTA MODIFICATIONS

Figure 4.1 indicates that the overall effect of adding delta planform extensions was to delay vortex bursting compared to the baseline model. The largest gains in terms of delaying vortex bursting came by increasing the area ratio. Although not enough different configurations were studied to come to any firm conclusions, it appears that increasing leading edge sweep decreases the rate of progression of the vortex burst point.

1. Area Ratio Effects

The area ratio of the exposed area of the apex delta to that of the waverider planform area model was increased from 0.5% to 2.0% while leading edge sweep angle of the apex delta was kept constant at 65° (modification two compared to modification one). Figure 4.1 indicates that vortex bursting was delayed by increasing the area ratio but that the rate of vortex burst progression was greater at higher angles-of-attack.

3. Leading Edge Sweep Effects

The leading edge sweep angle was decreased from 65° to 55° while the area ratio was held constant at 2.0% (modification three compared to modification two). Figure 4.1 indicates that vortex core stability was decreased (bursting occurred sooner) for modification three but was still better than

modification one up to about 17° angle-of-attack. The rate of vortex burst progression appears to be similar for the two modifications with equal area ratios (modifications two and three) up to 20° angle-of-attack, where modification three became very unstable.

C. RECOMMENDATIONS

The following recommendations are made based on this investigation:

1. Perform water tunnel testing of more apex delta planform variations to more fully understand the effect area ratio and leading edge sweep angle have on the vortical flow field.
2. Investigate other high lift concepts in an effort to delay vortex bursting up to the angles-of-attack seen in delta wings.
3. Perform low speed wind tunnel testing on the baseline configuration and on the most promising of the high lift modification concepts.
4. Evaluate the effect the apex delta has on the on-design performance of the optimized waverider.
5. To get a clearer picture of vortex core strength, measure primary vortex core longitudinal and circumferential velocities utilizing laser doppler velocimetry.

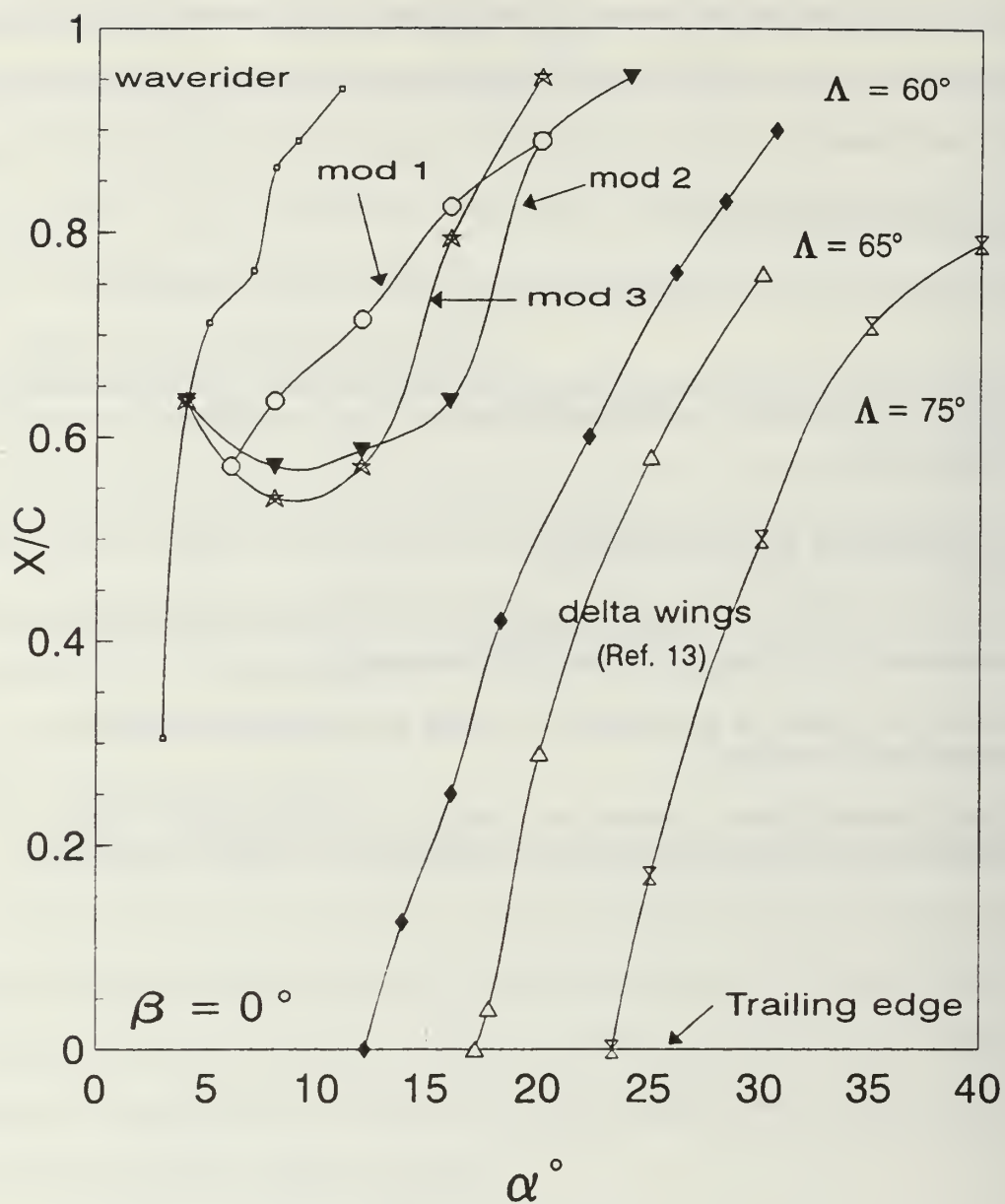


Figure 4.1 Comparison of 0° Sideslip Burst Behavior

APPENDIX A-MODEL SETUP AND INSTRUMENTATION

A. DYE PORT ATTACHMENT AND LOCATION

The injection dye tubes consisted of small brass tubes attached to the bottom surface of the model with cloth duct tape . Both the location of the tip of the dye tube and the injection rate were crucial to obtain good visualization of the model flowfield.

The dye tube was located flat on the model surface very close to the apex and oriented parallel to the flow. To investigate the entire planform flowfield, dye was also injected at arbitrary points along the leading edge of the model. Figure A.1 shows the position of the dye ports on the baseline model.

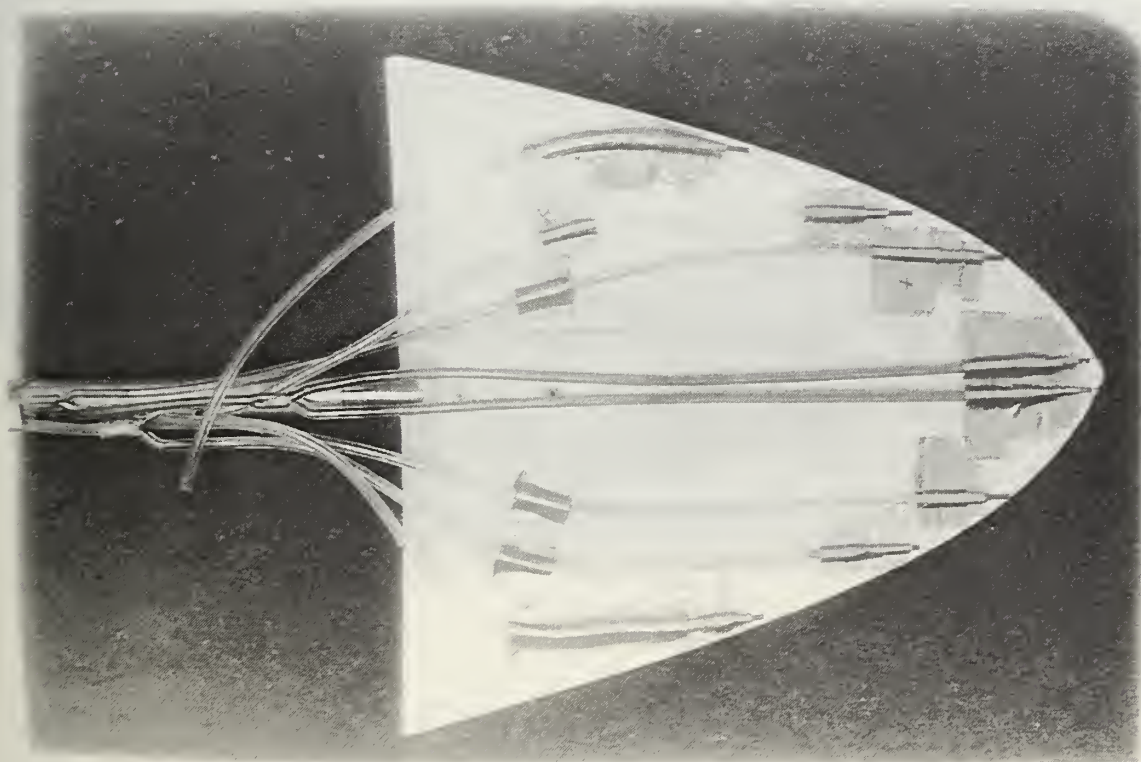


Figure A.1 Baseline model Dye Port Location

B. MODEL ALIGNMENT

Good model alignment in the test section was crucial to accurate flowfield visualization. Before each test, a spirit level was used to set the 0° pitch, roll, and yaw positions. Figures A.2 and A.3 show this procedure for the roll case. To adjust for flow angularity in the test section yaw alignment was visually confirmed by making sure the flowfield was symmetric with respect to the model centerline at the 0° yaw setting.

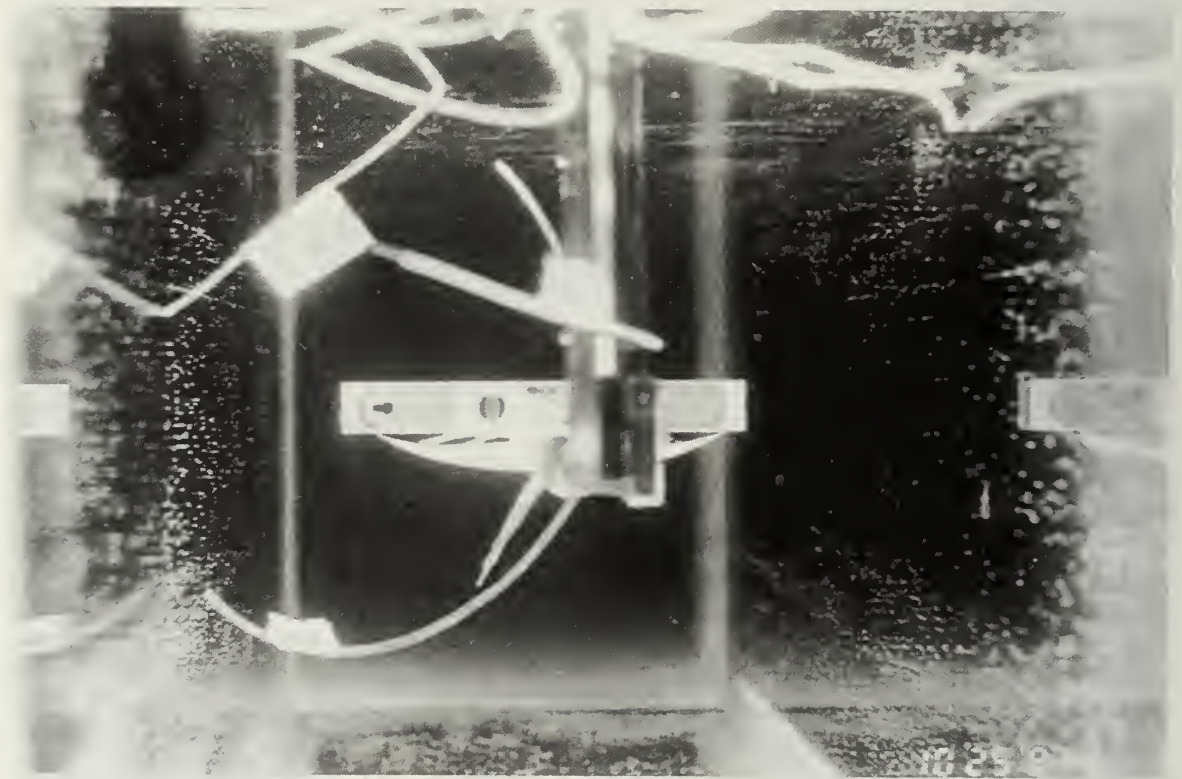


Figure A.2 Roll Level Adjustment (Rear View)



Figure A.3 Roll Level Adjustment (Top View)

APPENDIX B-APEX DELTA DESIGN

Three apex delta modifications were studied. Sweep angle and area ratio were varied as shown in Table 3.2. Each apex delta modification was constructed of 0.02 inch thick styrene plastic. This thickness was chosen because it very nearly matched the model leading edge thickness. The apex delta was then glued to the waverider leading edge, flush with the top surface of the model using Kwik Bond2 glue, made by Global Hobby Distributors of Fountain Valley, California. The removal process consisted of applying Z7 Debonding Agent, made by Pacer Technology of Rancho Cucamonga, California, and gently pulling the apex delta from the model. This was found to be the best procedure as the model leading edge and paint were left undamaged.

Sizing of each delta was critical to achieve the desired area ratios and was accomplished using basic geometry. Figure B.1 shows a sketch of the apex delta planform. In order to calculate the exposed delta planform area, it was necessary to approximate the waverider leading edge sweep at the nose as being a constant 35° . From this, and given the required area ratio and sweep of each modification, it was possible to calculate the required base and height of each delta. Table B.1 gives the dimensions of each modification. Figures B.2-B.7 show modification one, Figures B.8 and B.9 show modification two and Figures B.10-B.12 show modification three.

TABLE B.1 APEX DELTA DIMENSIONS

Modification	Base(inches)	Height(inches)	Sweep (Λ)
1	.739	.792	65°
2	1.476	1.583	65°
3	2.080	1.485	55°

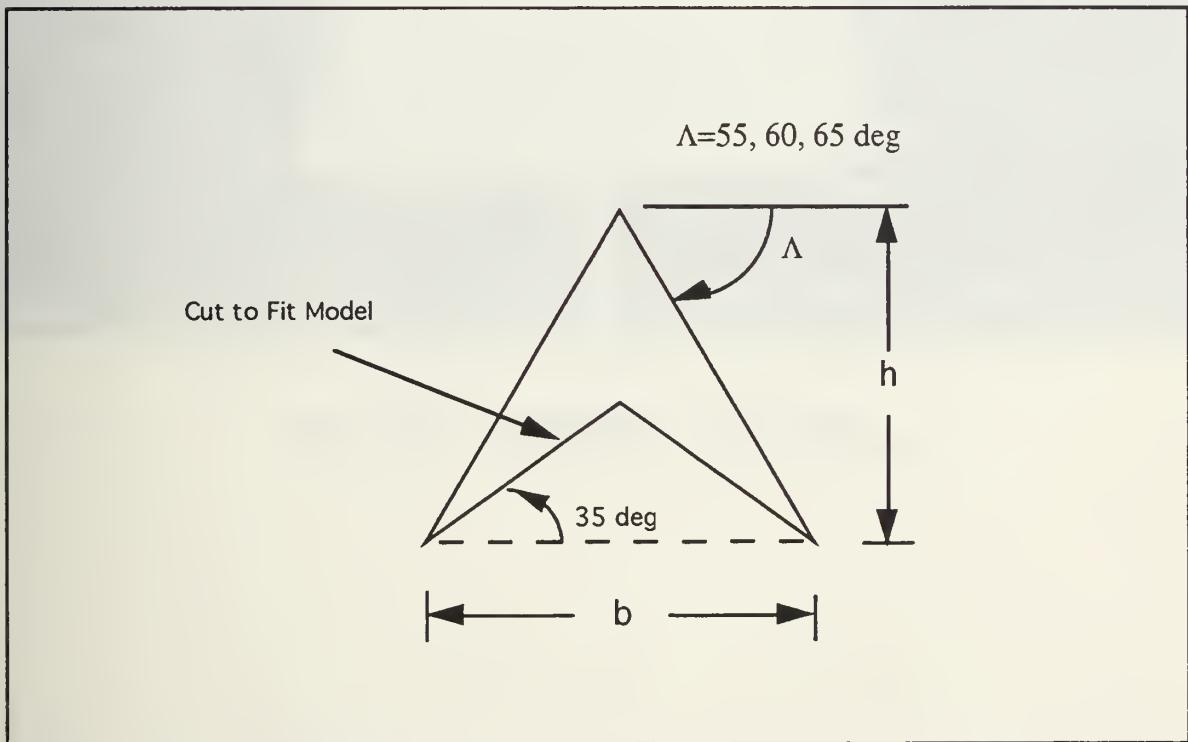


Figure B.1 Apex Delta

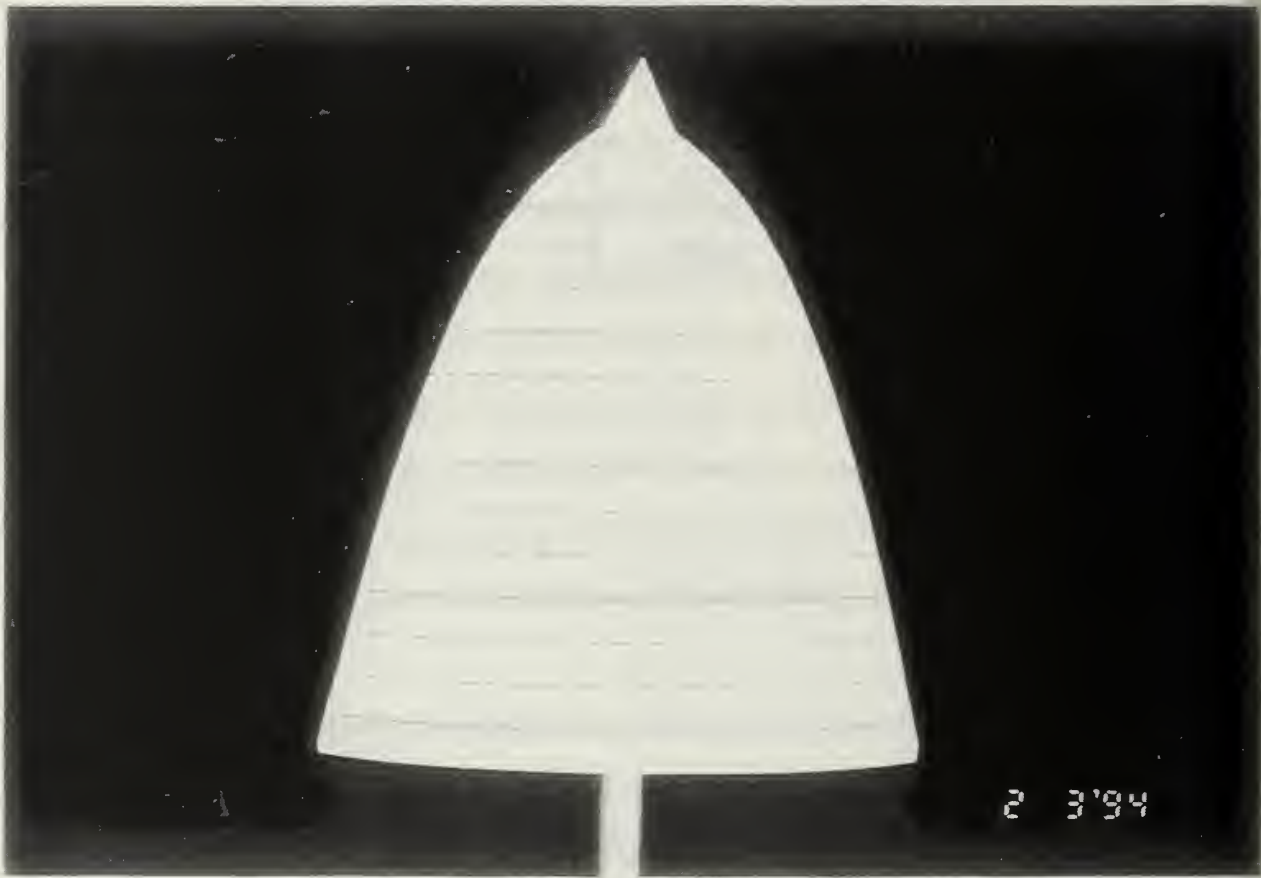


Figure B.2 Modification 1 (Top View)

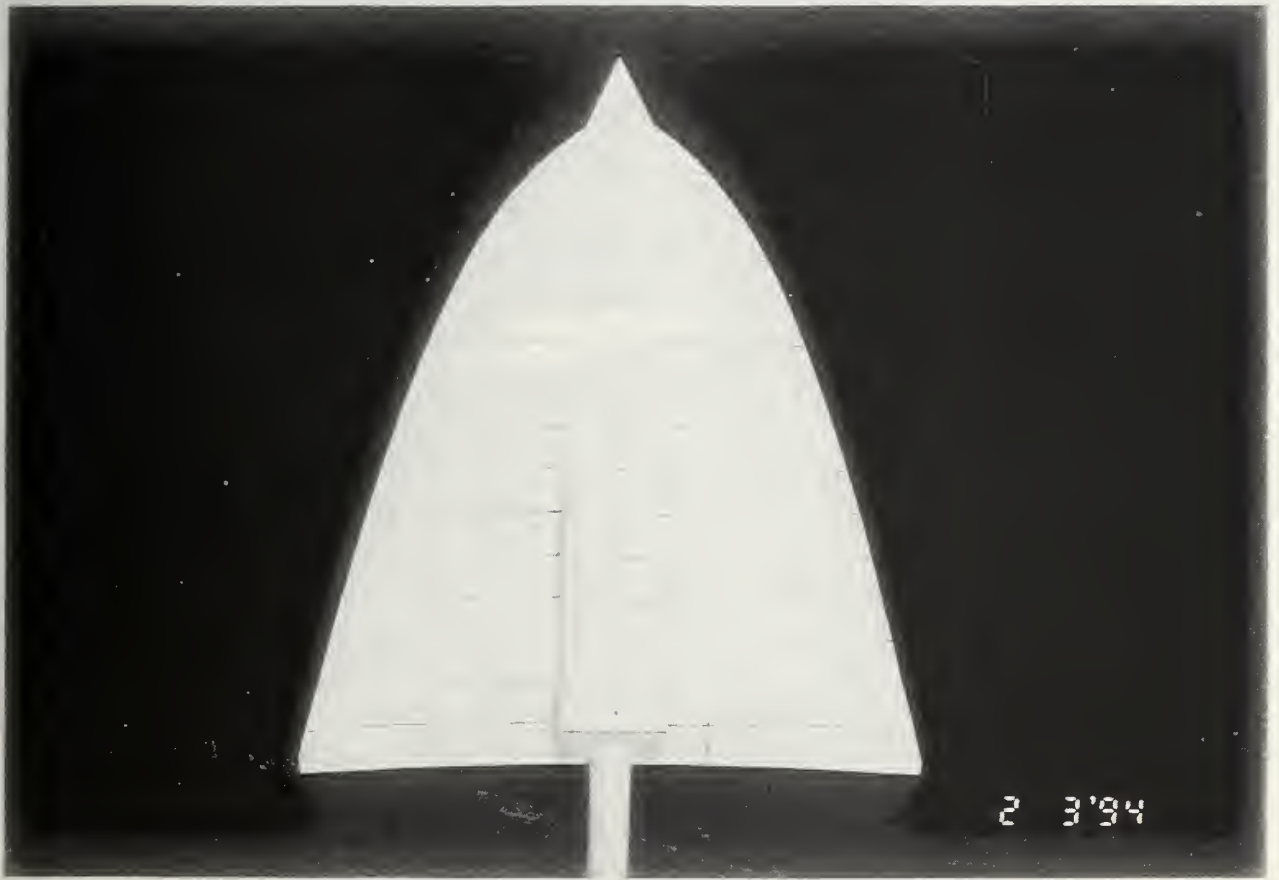


Figure B.3 Modification 1 (Bottom View)



Figure B.4 Modification 1 (Side View)



Figure B.5 Modification 1 (Isometric View)

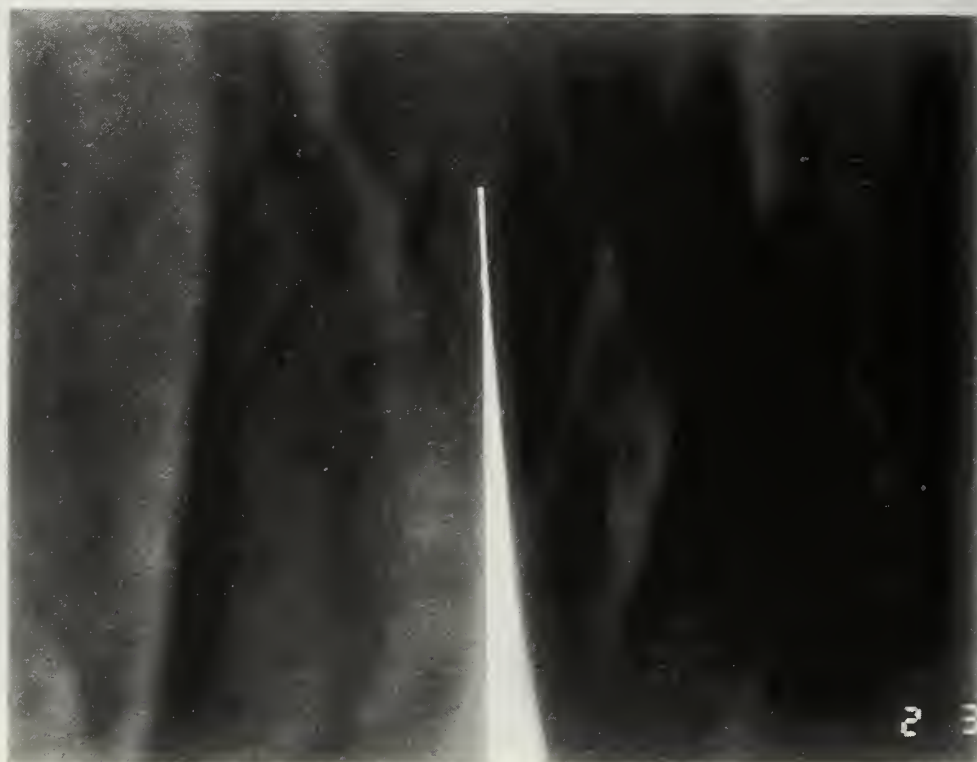


Figure B.6 Modification 1 (Side View Close-up)

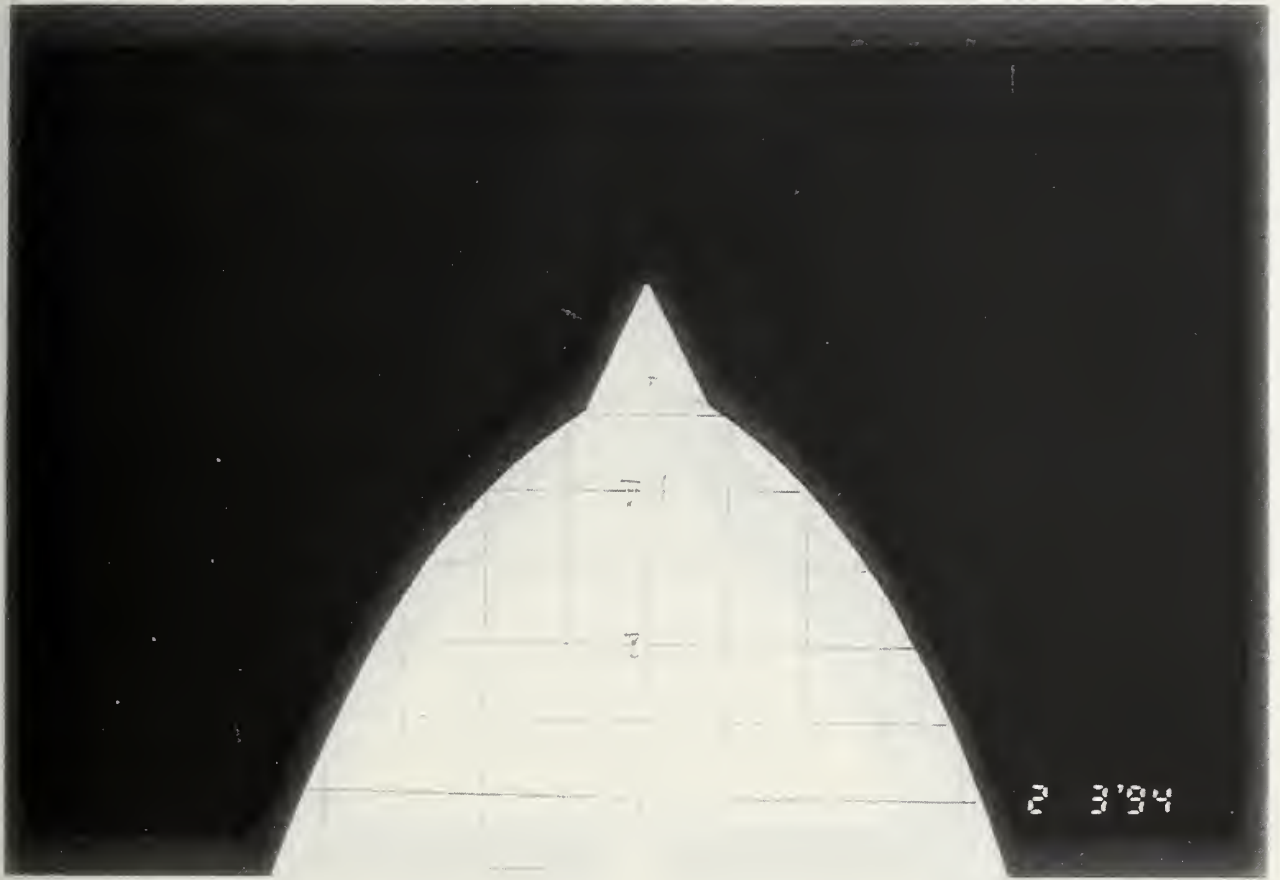


Figure B.7 Modification 1 (Bottom View Close-up)

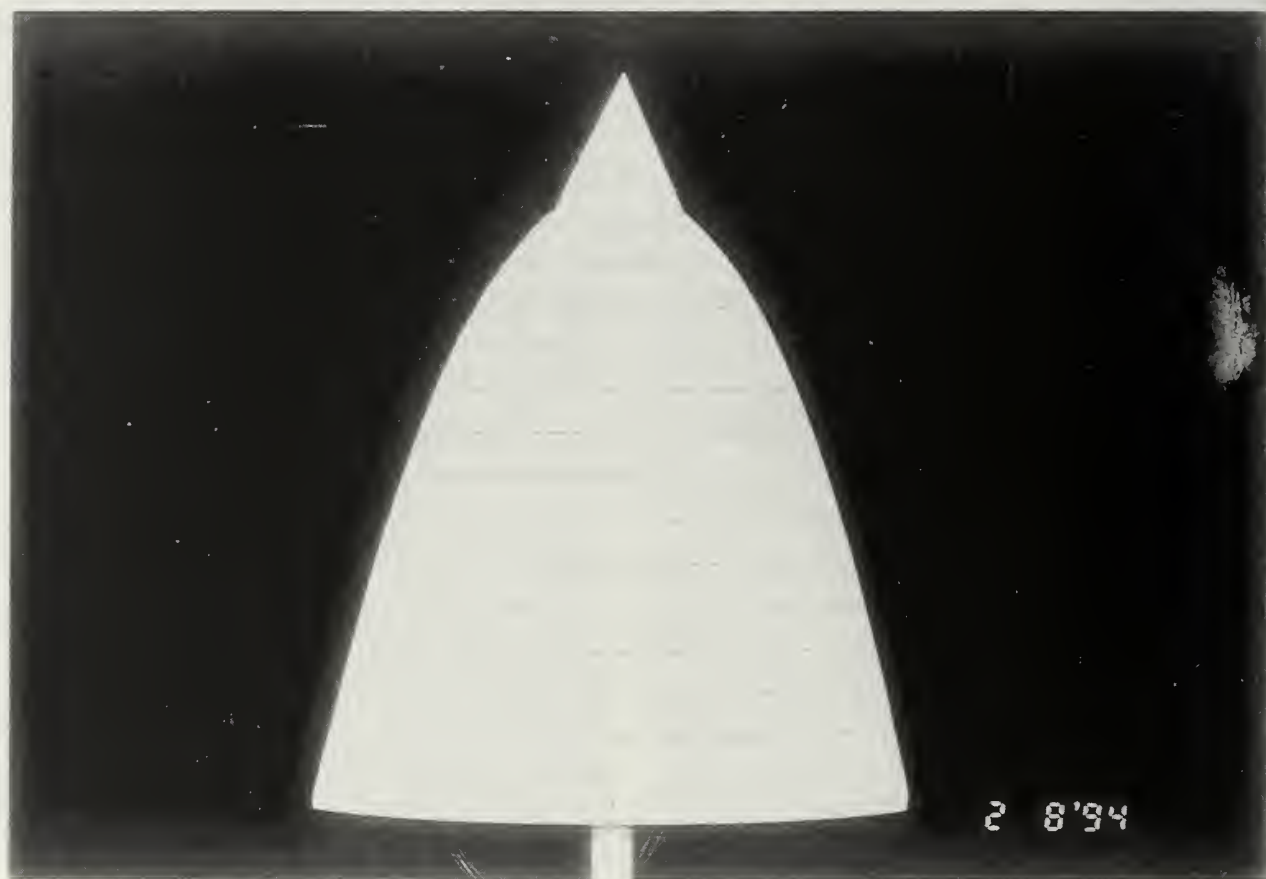


Figure B.8 Modification 2 (Top View)



Figure B.9 Modification 2 (Top View Close-up)

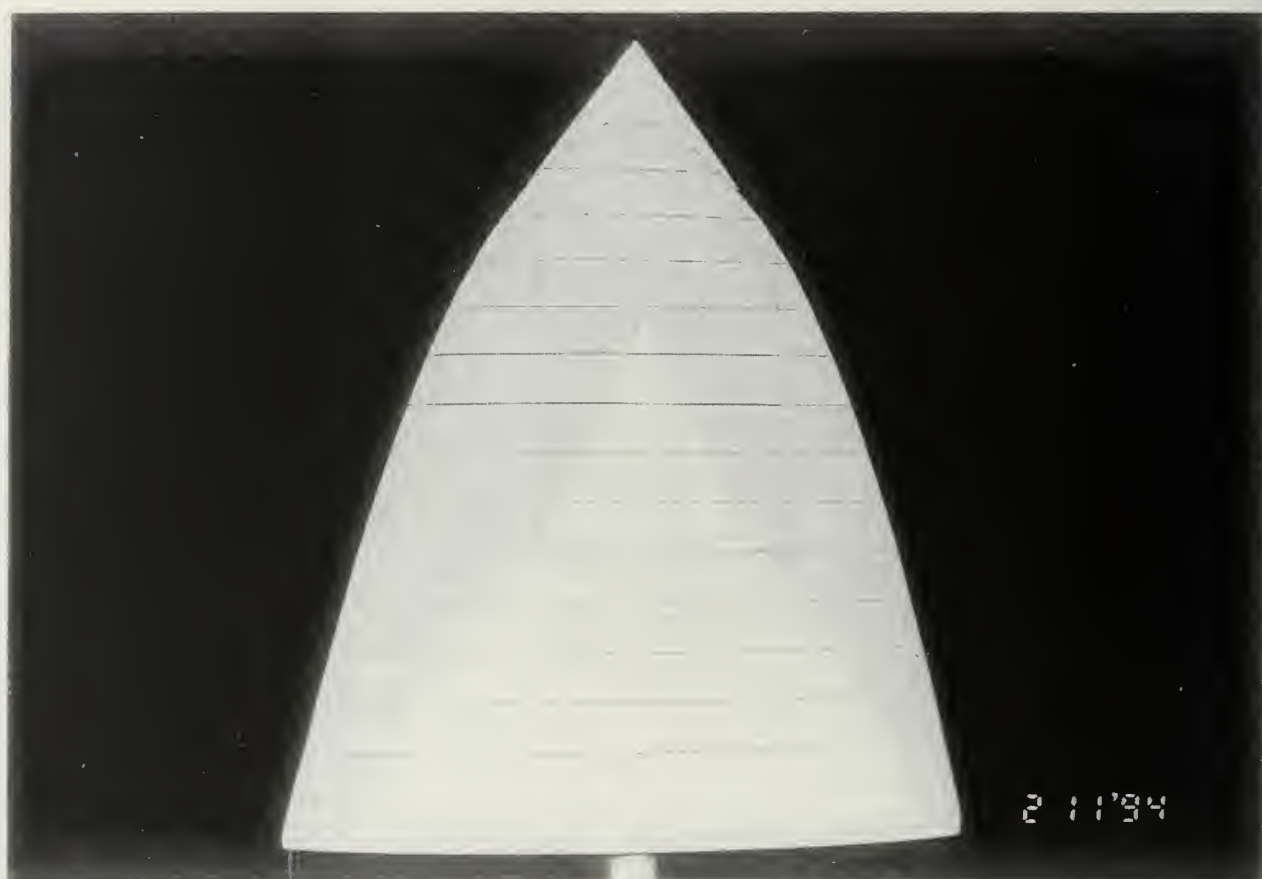


Figure B.10 Modification 3 (Top View)



Figure B.11 Modification 3 (Top View Close-up)

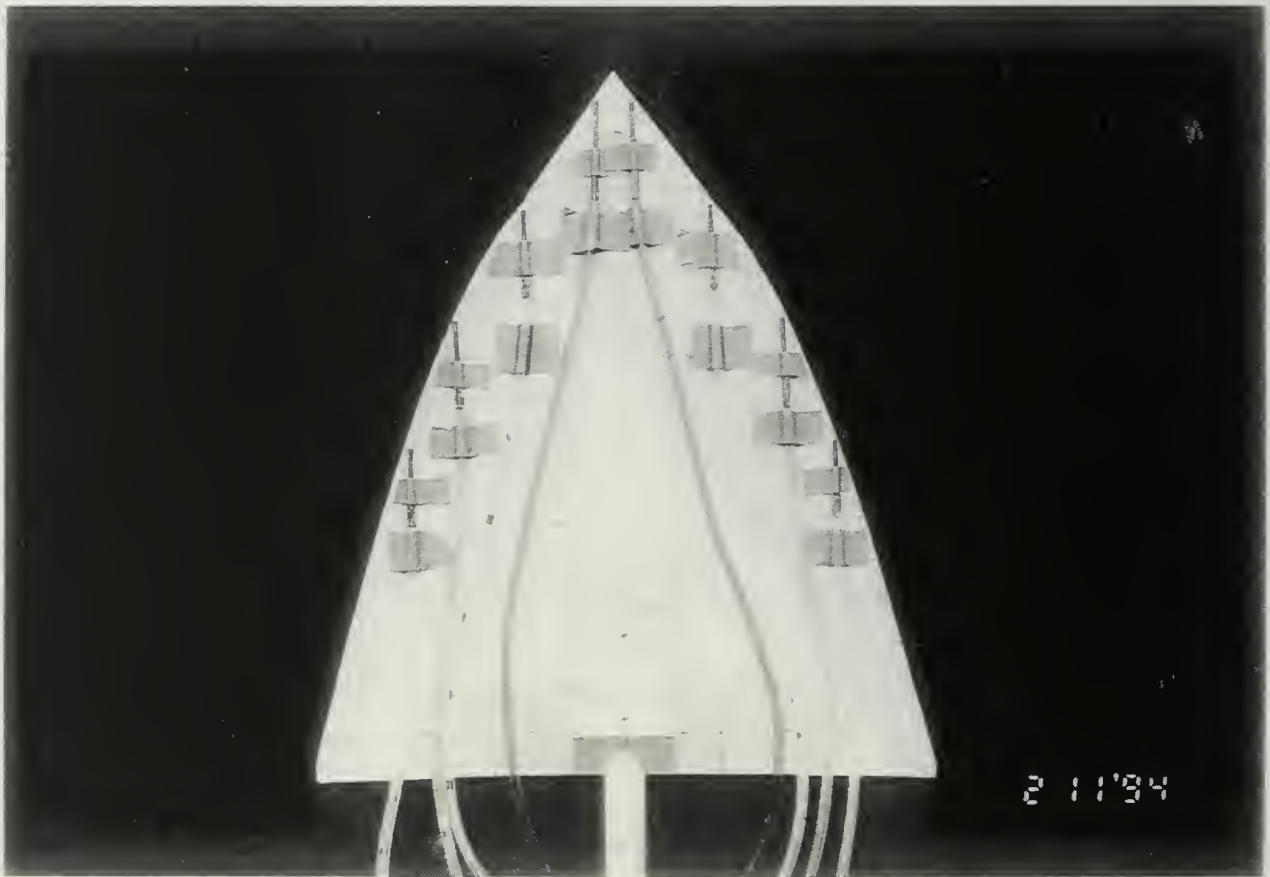


Figure B.12 Modification 3 (Bottom View) With Dye Ports

APPENDIX C-DATA TABLES

A. BASELINE

TABLE C.1
BASELINE, LATERAL CORE TRAJECTORY (LEEWARD)

X/C	β°	Y/C							
		$\alpha=2^\circ$	$\alpha=3^\circ$	$\alpha=4^\circ$	$\alpha=5^\circ$	$\alpha=6^\circ$	$\alpha=7^\circ$	$\alpha=8^\circ$	$\alpha=9^\circ$
.914	0	.0762	.0508	.0508	.0508	.0635	.0635	.0508	.0508
	5	.0508	.0635	.0635	.0635	.0635	.0635	.0635	.0635
	10	.0635	.0762	.0762	.0762	.0762	.0762	.0635	.0635
.762	0	.1524	.1524	.1524	.1524	.1524			
	5	.1651	.1778	.1651	.1651				
	10	.1778	.1778	.1778	.1778	.1651			
.508	0	.254	.254	.254					
	5	.280	.267	.279	.279				
	10	.292	.292	.292	.279	.279			
.254	0	.330							
	5	.356	.3302						
	10	.381	.381	.381	.381				
.127	0	.356							
	5	.381	.381						
	10	.419	.406	.419	.406				

TABLE C.2
BASELINE, LATERAL CORE TRAJECTORY (WINDWARD)

X/C	β°	Y/C							
		$\alpha=2^\circ$	$\alpha=3^\circ$	$\alpha=4^\circ$	$\alpha=5^\circ$	$\alpha=6^\circ$	$\alpha=7^\circ$	$\alpha=8^\circ$	$\alpha=9^\circ$
.914	0	.0762	.0508	.0508	.0508	.0635	.0635	.0508	.0508
	5	.076	.076	*	*	.051	.051	.051	.051
	10	.076	.051	.038	.038	.051	.051	.051	.051
.762	0	.1524	.1524	.1524	.1524	.1524			
	5	.152	.127						
	10	.152	.152	.152					
.508	0	.254	.254	.254					
	5	.254	.229						
	10	.229							
.254	0	.330							
	5								
	10								
.127	0	.356							
	5								
	10								

* Core location could not be determined

TABLE C.3
BASELINE, BURST LOCATION

α°	X/C				
	$\beta=0^\circ$	leeward	leeward	windward	windward
		$\beta=5^\circ$	$\beta=10^\circ$	$\beta=5^\circ$	$\beta=10^\circ$
2	*	*	*	.406	.508
3	.305	*	*	#	.711
4	.508	.254	*	#	.762
5	.711	.356	.127	#	.838
6	.737	.508	.356	.813	.864
7	.762	.762	.508	.863	.889
8	.863	.838	.762	.889	.902
9	.889	.914	.863	.915	.914
10	.915	.94	.889	.94	.94
11	.94		.914		

*No bursting

#Burst point could not be determined

B. MODIFICATION ONE

TABLE C.4
MOD 1, LATERAL CORE TRAJECTORY (LEEWARD)

X/C	β°	Y/C					
		$\alpha=4^\circ$	$\alpha=8^\circ$	$\alpha=12^\circ$	$\alpha=16^\circ$	$\alpha=20^\circ$	$\alpha=24^\circ$
.889	0	.0508	.0508	.0508	.0508	.0508	
	5	.0635	.0635	.0635	.0635		
	10	.0635	.0635	.0635	.0635	.0635	
.825	0	.0952	.0952	.0952	.0952		
	5	.0952	.0952	.0952	.0952		
	10	.111	.111	.111	.111		
.635	0	.175	.190				
	5	.190	.190	.190			
	10	.222	.206	.206			
.508	0	.222					
	5	.248	.248				
	10	.260	.260	.260			
.254	5		.330				
	10	.349	.349	.349			

TABLE C.5
MOD 1, LATERAL CORE TRAJECTORY (WINDWARD)

X/C	β°	Y/C					
		$\alpha=4^\circ$	$\alpha=8^\circ$	$\alpha=12^\circ$	$\alpha=16^\circ$	$\alpha=20^\circ$	$\alpha=24^\circ$
.889	5	.0318	.0476	.0476			
	10	*	.0476				
.825	5	*	.0794	.0794			
	10						
.635	5						
	10						
.508	5						
	10						
.254	5						
	10						

*Vortex undefined

TABLE C.6
MOD 1, BURST LOCATION

α°	X/C				
	$\beta=0^\circ$	leeward	leeward	windward	windward
		$\beta=5^\circ$	$\beta=10^\circ$	$\beta=5^\circ$	$\beta=10^\circ$
2	*				
4		.381	#		
6	.571				
8	.635	#	0	.603	.889
12	.714	.667	.254	.825	.921
16	.825	.810	.667	.921	1
20	.889	.905	.825		
24					

*Vortex undefined

#Burst point located aft of trailing edge

C. MODIFICATION TWO

TABLE C.7
MOD 2, LATERAL CORE TRAJECTORY (LEEWARD)

X/C	β°	Y/C					
		$\alpha=4^\circ$	$\alpha=8^\circ$	$\alpha=12^\circ$	$\alpha=16^\circ$	$\alpha=20^\circ$	$\alpha=24^\circ$
.889	0	.0699	.0699	.0699	.0699	.0699	.0699
	5	.0762	.0699	.0699	.0699	.0699	.0699
	10	.0762	.0762	.0762	.0762	.0762	
.825	0	.0826	.0826	.0826	.0826		
	5	.0889	.0889	.0889	.0889	.0889	.0889
	10	.0953	.1016	.1016	.1016	.1016	
.635	0	.1778	.1778	.1778	.1778		
	5	.1905	.1905	.1842			
	10	.1905	.1905	.1905	.1905	.1905	
.508	0						
	5						
	10	.254	.254	.254	.254	.254	
.254	5						
	10	.3683	.3493	.3302	.3302		

TABLE C.8
MOD 2, LATERAL CORE TRAJECTORY (WINDWARD)

X/C	β°	Y/C					
		$\alpha=4^\circ$	$\alpha=8^\circ$	$\alpha=12^\circ$	$\alpha=16^\circ$	$\alpha=20^\circ$	$\alpha=24^\circ$
.889	0	.0699	.0699	.0699	.0699	.0699	.0699
	5	.0635	.0635	.0635	.0635		
	10	.0635	.0635	.0635	.0635		
.825	0	.0826	.0826	.0826	.0826		
	5	.0762	.0762	.0762	.0762		
	10	.0762	.0762	.0826			
.635	0	.1778	.1778	.1778	.1778		
	5	.1588	.1461	.1588			
	10						
.508	0						
	5						
	10						
.254	5						
	10						

TABLE C.9
MOD 2, BURST LOCATION

α°	X/C				
	$\beta=0^\circ$	leeward	leeward	windward	windward
		$\beta=5^\circ$	$\beta=10^\circ$	$\beta=5^\circ$	$\beta=10^\circ$
4	.635	.413	.318	.635	.635
8	.571	.381	*	.571	.698
12	.587	.413	*	.667	.730
16	.635	.444	*	.825	.889
20	.889	.698	.508	.952	
24	.952	.825	.825		

*Burst point located aft of trailing edge

D. MODIFICATION THREE

TABLE C.10
MOD 3, LATERAL CORE TRAJECTORY (LEEWARD)

X/C	β°	Y/C						
		$\alpha=4^\circ$	$\alpha=8^\circ$	$\alpha=12^\circ$	$\alpha=16^\circ$	$\alpha=18^\circ$	$\alpha=20^\circ$	$\alpha=24^\circ$
.889	0	.0698	.0698	.0698	.0698			
	5	.0762	.0762	.0762	.0762		.0762	
	10	.0762	.0762	.0762	.0762	.0762		
.825	0	.0953	.0953	.0953	.0953		.0953	
	5	.1016	.1016	.1016	.1016			
	10	.1143	.1143	.1143	.1143			
.635	0	.1905	.1905	.1842				
	5	.1905	.1905	.1905	.1905			
	10	.1905	.1905	.1905	.1905			
.508	0	.2222	.2222	.2222				
	5	.254	.2413	.2413				
	10	.2604	.254	.254				
.254	5	.3175	.3175					
	10	*	.3302	.3302				

*Vortex Burst

TABLE C.11
MOD 3, LATERAL CORE TRAJECTORY (WINDWARD)

X/C	β°	Y/C						
		$\alpha=4^\circ$	$\alpha=8^\circ$	$\alpha=12^\circ$	$\alpha=16^\circ$	$\alpha=18^\circ$	$\alpha=20^\circ$	$\alpha=24^\circ$
.889	0	.0698	.0698	.0698	.0698			
	5	.0635	.0635	.0635				
	10	.0635	.0635	.0635				
.825	0	.0953	.0953	.0953	.0953		.0953	
	5	.0889	.0889	.0889				
	10	.0889	.0889	.0889				
.635	0	.1905	.1905	.1842				
	5							
	10							
.508	0	.2222	.2222	.2222				
	5							
	10							
.254	5							
	10							

TABLE C.12
MOD 3, BURST LOCATION

α°	X/C				
		leeward	leeward	windward	windward
		$\beta=5^\circ$	$\beta=10^\circ$	$\beta=5^\circ$	$\beta=10^\circ$
	$\beta=0^\circ$				
4	.635	*	.381	.762	.794
8	.540	*	*	.794	.825
12	.571	.317	.127	.762	.857
16	.794	.667	.413	.889	.952
18			.635		
20	.952	.857			
24		.952			

*Burst point located aft of trailing edge

LIST OF REFERENCES

1. Nonweiler, T.R.F., "Aerodynamic Problems of Manned Space Vehicles," Journal of the Royal Aeronautical Society, v. 63, pp. 521-528.
2. Seddon, J. and Spence, A., "The Use of Known Flowfields as an Approach to the Design of High Speed Aircraft", Hypersonic Boundary Layers and Flow Fields, Agard CP No. 30, May 1968, pp 10/1-10/21.
3. Ward, Lauren, "Riding the Shockwave," Skyline, North American Aviation, volume 19, number 1, March 1961, pp. 20-27.
4. Rassmussen, M.L., "Waverider Configurations Derived from Inclined Circular and Elliptic Cones", Journal of Spacecraft and Rockets, vol. 17, No. 6, Nov. 1980, pp. 537-545.
5. Eggers, A.J., and others, "Hypersonic Waverider Configurations from the 1950's to the 1990's," Proceedings of the 1st Hypersonic Waverider Symposium, October 1990.
6. Vanhoy, D.L., Low-Speed Wind Tunnel Testing of a Mach 6 Viscous Optimized Waverider, Masters Thesis, University of Maryland, College Park, Maryland, May 1988.
7. Price, D.R., Optimization and Performance Analysis of a Supersonic Conical-Flow Waverider for a Deck-Launched Intercept Mission, Masters Thesis, Naval Postgraduate School, Monterey, California, June 1993.
8. Price, D.R., "The Ames Waverider Code: Introduction and Use," presented to Professor Newberry, Naval Postgraduate School, Monterey, California, June 1993.
9. Kerns, S.B., "Numerical Investigation of Vortex Flow Control Through Small Geometry Modifications at the Strake Wing Junction of a Cropped Double-Delta Wing." AIAA paper 92-0411, January 1992.
10. Anderson, J.D., Fundamentals of Aerodynamics, 2d ed., pp 356-365, McGraw-Hill, Inc. 1991.
11. National Physical Laboratory, R&M No. 3282, The Bursting of Leading-Edge Vortices-Some Observations and Discussion of the Phenomena, by N.C. Lambourne and D.W. Bryer, April 1961.

12. Hebbar, S.K., Platzer, M.F., Park, S.N., and Cavazos, O.V., "A Dynamic Flow Visualization Study of a Two-Percent F/A-18 Fighter Aircraft Model at High Angles of Attack," High Angle of Attack Technology, Vol. I< NASA CP-3149, Part 3, pp. 1025-1037, May 1992.
13. Erickson, G.E., "Flow Studies of Slender Wing Vortices," AIAA 13th Fluid and Plasma Dynamics Conference, Snowmass, Colorado, 14-16 July 1980.
14. R.A.E Tecnical Report 69051, Low-speed Characteristics of Waverider Wings, by R.F.A. Keating, 1970.

INITIAL DISTRIBUTION LIST

	No. Copies
1. Defense Technical Information Center Cameron Station Alexandria, Virginia 22304-6145	2
2. Library, Code 52 Naval Postgraduate School Monterey, California 93943-5100	2
3. Professor C. F. Newberry, Code AA/Ne Dept. of Aeronautics and Astronautics Naval Postgraduate School Monterey, California 93943	3
4. Professor S. K. Hebar, Code AA/He Dept. of Aeronautics and Astronautics Naval Postgraduate School Monterey, California 93943	1
5. Mr. J. V. Bowles Systems Analysis Branch M/S 237-11 NASA Ames Research Center Moffett Field, California 94035-1000	1
6. Dr. Kevin G. Bowcutt Rockwell International MC SX40 2600 Westminster Blvd Seal Beach, California 90740-7644	1
7. Dr. Mark J. Lewis Dept. of Aerospace Engineering University of Maryland College Park, Maryland 20742	1
8. Dr. John D. Anderson Dept. of Aerospace Engineering University of Maryland College Park, Maryland 20742	1

8. Dr. Isaiah Blankson 1
Code RN
NASA Headquarters
Washington, DC 20546-0001
9. David Price 1
160 Westover Circle
Navato, California 94949
10. Dr. Vicki S. Johnson 1
Advanced Design Program
3600 Bay Area Boulevard
Houston, Texas 77058-1113
11. Robert C. Bisbee 2
101 Buena Vista Drive
Box 204
Arlington, Wisconsin 53911

DODLEY KNOX LIBRARY
NAVAL POSTGRADUATE SCHOOL
MONTEREY CA 93943-5001

GAYLORD S

DUDLEY KNOX LIBRARY



3 2768 00307300 8